

2  
MAR 18 1994

AD-A278 477



AEOSR-TR 94 0200

AFOSR/NL

Approved for public release;  
distribution unlimited.

**BASIC RESEARCH IN NUCLEAR TEST MONITORING:  
EXPLOSIONS IN NON-SPHERICAL CAVITIES;  
INVESTIGATION OF ENHANCED BACKSCATTERING**

Batakrishna Mandal  
Craig A. Schultz  
Wenjie Dong  
M. Nafi Toksöz  
William Rodi

DTIC  
ELECTED  
APR 21 1994  
S G D

Earth Resources Laboratory  
Department of Earth, Atmospheric, and  
Planetary Sciences  
Massachusetts Institute of Technology  
Cambridge, Massachusetts 02139

1 January 1994

Contract F49620-92-J-0413  
Annual Technical Report  
1 August 1992-31 July 1993

Accesion For	
NTIS	CRA&I
DTIC	TAB
Unannounced	
Justification _____	
By _____	
Distribution / _____	
Availability Codes	
Dist	Avail and / or Special
A-1	

APPROVED FOR PUBLIC RELEASE; DISTRIBUTION UNLIMITED

DTIC QUALITY INSPECTED 3

94-12084



103P8

94 4 20 118

# REPORT DOCUMENTATION PAGE

Form Approved  
OMB No. 0704-0188

Estimated burden for this collection of information is estimated to average 1 hour per response, including the time for reviewing instructions, searching existing data sources, gathering and maintaining the data needed, and completing and reviewing the collection of information. Send comments regarding this burden estimate or any other aspect of this collection of information, including suggestions for reducing this burden, to Washington Headquarters Services, Directorate for Information Operations and Reports, 1200 2nd Street, SW, Washington, DC 20314-0198, and to the Office of Management and Budget, Paperwork Reduction Project (0704-0188), Washington, DC 20503.

1. AGENCY USE ONLY (Leave blank)	2. REPORT DATE	3. REPORT TYPE AND DATES COVERED	
	1 Jan 1994	Annual Technical 1 Aug 92 - 31 Jul 93	
4. TITLE AND SUBTITLE		5. FUNDING NUMBERS	
Basic Research in Nuclear Test Monitoring: Explosions in Non-Spherical Cavities; Investigation of Enhanced Backscattering		2309/AS F49620-92-J-0413 61102F	
6. AUTHOR(S)		7. PERFORMING ORGANIZATION NAME(S) AND ADDRESS(ES)	
B. Mandal M.N. Toksöz C. A. Schütz W. Rodi W. Dong		Massachusetts Institute of Technology 77 Massachusetts Avenue Cambridge, MA 02139	
8. PERFORMING ORGANIZATION REPORT NUMBER		9. SPONSORING / MONITORING AGENCY NAME(S) AND ADDRESS(ES)	
AFOSR-TR. 94 0200 60003		AFOSR/NL Building 410 Bolling Air Force Base DC 20332-6448 Dr. Stanley K. Dickinson	
10. SPONSORING / MONITORING AGENCY REPORT NUMBER			
11. SUPPLEMENTARY NOTES			
12a. DISTRIBUTION / AVAILABILITY STATEMENT		12b. DISTRIBUTION CODE	
Distribution Unlimited  Approved for public release: distribution unlimited.			
13. ABSTRACT (Maximum 200 words)			
<p>We report on two studies. The first is a theoretical study of the seismic radiation from explosions detonated in finite cylindrical tunnels embedded in a homogeneous, isotropic, elastic medium. We developed a frequency domain boundary element/discrete wavenumber algorithm to model the seismic wavefields from such sources, and applied the algorithm to study two specific cases of explosion sources—nuclear and non-nuclear. Our calculations show different source radiation patterns between the two types of explosions, especially when the explosion is located off-center in the tunnel in which case the non-nuclear explosion radiation displays strong directivity effects. Both types of explosions radiate significant shear wave energy outside the cavity. The second study is on enhanced seismic backscattering from rough interfaces. We experimentally and numerically investigate the scattering of an acoustic P wave incident on a highly irregular, random acoustic-elastic interface to determine whether enhanced backscattering occurs. The experiments involve ultrasonic waves reflected from a glass surface etched to produce a highly irregular 3-D surface. We find that 2-D numerical results predict the 3-D experimental results well at small incident angles. Both numerical and experimental results strongly support the presence of enhanced backscattering.</p>			
14. SUBJECT TERMS		15. AVAILABILITY	
explosion seismology, non-spherical cavities, seismic scattering, enhanced backscattering		103	
16. PRICE CODE			
17. SECURITY CLASSIFICATION OF REPORT	18. SECURITY CLASSIFICATION OF THIS PAGE	19. SECURITY CLASSIFICATION OF ABSTRACT	20. LIMITATION OF ABSTRACT
Unclassified	Unclassified	Unclassified	

## TABLE OF CONTENTS

List of Contributing Scientists .....	iv
List of Previous and Related Contracts .....	iv
Bibliography of Publications Totally or Partially Supported by the Contract .....	iv
Preface .....	v
Wavefields From an Explosion Along the Axis of a Finite Tunnel .....	1
Summary .....	1
Introduction .....	2
Method .....	4
Results .....	9
Conclusions .....	13
References .....	14
Figures .....	18
Experimental Study of Scattering From a Highly Irregular, Acoustic-Elastic Interface .....	31
Summary .....	31
Introduction .....	32
Theory .....	35
Experimental Procedure .....	43
Surface Scattering Measurements .....	50
Conclusions .....	60
References .....	63
Appendix A: Numerical Formulation—Acoustic-Elastic Case .....	65
Appendix B: Ultrasonic Design .....	67
Figures .....	71

## **List of Contributing Scientists**

Batakrishna Mandal, Research Scientist, Massachusetts Institute of Technology

Craig A. Schultz, Graduate Research Assistant, Massachusetts Institute of Technology

Wenjie Dong, Graduate Research Assistant, Massachusetts Institute of Technology

M. Nafi Toksöz, Professor of Geophysics, Massachusetts Institute of Technology

William Rodi, Research Scientist, Massachusetts Institute of Technology

## **List of Previous and Related Contracts**

DARPA/AFGL Contract F19628-89-K-0020 "Regional Seismograms: Attenuation and Scattering", July 1989 to June 1991.

DARPA/AFPL Contract F19628-90-K-0057 "Research in Regional Seismology: The Effect of Anisotropy", August 1990 to July 1992.

DARPA/AFPL Contract F29601-91-K-DB15 "Research on Monitoring at Regional Distances", September 1991 to July 1993.

## **Bibliography of Publications Totally or Partially Sponsored by the Contract**

Toksöz, M.N., B. Mandal, W. Dong, and C.A. Schultz, 1993, Seismic scattering from non-spherical cavities and rough interfaces, *Papers Presented at 15th Ann. PL/DARPA Seismic Res. Symp.*, ?.

Peng, C. and M.N. Toksöz, 1993, Optimal absorbing boundary conditions for finite difference modelings of acoustic and elastic wave propagation, *J. Acoust. Soc. Am.*, in press.

## PREFACE

The objective of this research project is to understand phenomena of seismic wave generation and propagation that affect regional and teleseismic seismograms used for nuclear test monitoring. This annual technical report includes two studies. The first is a theoretical study of the seismic radiation from explosions detonated in non-spherical cavities, i.e., cylindrical tunnels of finite length embedded in a homogeneous, isotropic, elastic medium. A frequency domain boundary element/discrete wavenumber algorithm is applied to compute seismic wavefields from nuclear and non-nuclear explosions located at various positions along a tunnel axis. The computed radiation patterns display strong shear wave generation and show significant differences between the two types of explosions. In the second study, we experimentally and numerically investigate the scattering of an acoustic P wave incident on a highly irregular, random acoustic-elastic interface to determine whether enhanced backscattering occurs. The experiments involve ultrasonic waves reflected from a glass surfaced etched to produce a highly irregular 3-D surface. We find that 2-D numerical simulations predict the 3-D experimental results well at small incident angles. Both numerical and experimental results strongly support the presence of enhanced backscattering. The report on this latter study is a preprint of a paper submitted to the *Journal of the Acoustical Society of America*.

# WAVEFIELDS FROM AN EXPLOSION ALONG THE AXIS OF A FINITE TUNNEL

## Summary

This study examines the source radiation from explosions detonated in a cylindrical cavity of finite length (tunnel) embedded in an infinite homogeneous elastic isotropic background medium. The radiated wavefields are modeled using a frequency domain boundary element/discrete wavenumber algorithm. The algorithm employs the indirect formulation of boundary integral equations for fluid and elastic media. For axially symmetric problems, the explosion source is modeled as fictitious surface sources distributed on the cavity boundary. Upon discretizing the cavity boundary into elements of uniform source distribution, and then imposing boundary conditions at each element, a system of equations is obtained with the fictitious source distribution on each element as the unknowns. Elements of the resulting coefficient matrix are integrals of displacement and stress Green's functions over boundary elements. Once the equivalent boundary sources are determined, wavefields inside and outside the cavity are easily calculated. We apply the algorithm to study two specific cases of explosion sources: nuclear and non-nuclear. A nuclear explosion is specified by assigning a very high compressional velocity of 10 km/sec inside the cavity, representing loading of the cavity wall by a shock wave. An ordinary pressure wave traveling in air (330 m/sec) is used for a non-nuclear explosion. The results show different source radiation patterns between

the two types of explosions, especially when the explosion is located off-center in which case the non-nuclear explosion radiation displays strong directivity effects. In contrast, radiation from a nuclear explosion does not depend on the source position inside the tunnel. Both types of explosions radiate significant shear wave energy outside the cavity.

## Introduction

Seismic radiation from a nuclear explosion is generally more complicated than that of a simple isotropic point source. This has been shown by various observations (e.g., Day *et al.*, 1983; Wallace *et al.*, 1983, 1985; Priestley *et al.*, 1990). The observations from nuclear explosions may be explained by one or more of the following physical mechanisms: (1) the nuclear explosion itself; (2) tectonic release; (3) spall; (4) anisotropic and heterogeneous media near the source; and (5) asymmetry of the source. So far no single one of these mechanisms has proven sufficient to explain all of the observed data (Massé, 1981; Gupta and Blandford, 1983; Johnson, 1988).

The purpose of this study is to investigate the seismic radiation from an explosive source placed in a non-spherical cavity. The effects of spherical cavities on seismic explosions was studied in the early sixties (e.g., Latter *et al.*, 1961). Glenn *et al.* (1985) and Rial and Moran (1986) studied the coupling mechanism and the radiation pattern from an explosion in an ellipsoidal cavity in an unbounded medium. Helmberger *et al.* (1991) showed that correct modeling of near-field seismograms observed after nuclear explosions requires distinct source

characteristics as well as the local crustal structure. They modeled the source characteristics by using asymmetric sources inside ellipsoidal cavities. Lately, Zhao and Harkrider (1992) showed in their theoretical investigation that asymmetry of the source region has a more significant effect on shorter period radiation than longer period radiation. In this study, we have investigated the generation of compressional and shear waves from explosions placed along the axis of cylindrical tunnels of various diameters.

Modeling far-field radiation from sources placed in a cavity poses difficulties for the finite difference method (FDM) and the finite element method (FEM), because of large scale differences between the cavity surface and formation extent. The ability to calculate the far-field wavefields is severely restricted by the computer memory space needed by these methods. The accuracy of these methods is also hampered by grid dispersion and inaccurate handling of the fluid/formation interface. For a finite cavity, the commonly used discrete wavenumber method based on the vertical wavenumber representation is no longer applicable. To overcome these difficulties, an indirect boundary element method (BEM) combined with a discrete wavenumber method based on the Sommerfeld integral representation is used.

The BEM was first established through the direct formulation by Jawson (1963) and Symm (1963) for potential theory, Rizzo (1967) for elastostatics, and Cruse (1968) for elastodynamics. Applications of the indirect BEM in elastodynamics only appeared recently for seismic wave scattering by surface topographies (e.g., Wong, 1982; Kawase, 1988; Sánchez-Sesma and Campillo, 1991). Along a similar line, work based on boundary integral equation

and discrete vertical wavenumber formulations (Campillo and Bouchon, 1985; Bouchon *et al.*, 1989) have emerged. Bouchon and Schmitt (1989) applied this method in studying full waveform acoustic logging in an infinite irregular borehole. However, the formulation of this method was limited to an infinite borehole in an infinite homogeneous medium. More recently, Bouchon (1993) and Dong (1993) developed a BEM algorithm to model downhole seismic sources in layered isotropic and transversely isotropic media. Dong (1993) also used BEM to model sources in semi-infinite boreholes.

In this study, we extend the BEM method for sources in semi-infinite boreholes to model wave radiation from an explosion source in a finite cavity embedded in a homogeneous medium.

## Method

### Indirect Integral Formulation

If a volume point source is placed inside a cavity, the total displacement potential in the cavity fluid is the sum of a direct potential due to the source and a reflected potential due to the boundary. In the case of steady state radiation (or in the frequency domain) the reflected field can be expressed as an integral of a fictitious source distribution over the cavity surface, with a Green's function being the integrand. Therefore, the displacement potential in the fluid is

$$\phi_1(\mathbf{x}) = \phi_i + \int_B dS' g_1(\mathbf{x}, \mathbf{x}') \psi(\mathbf{x}') \quad \text{for } \mathbf{x} \in V_b + B , \quad (1)$$

where the volume of cavity fluid and the cavity surface are denoted by  $V_b$  and  $B$ , respectively. Subscript 1 stands for the fluid region and  $\phi_i$  is the incident potential. The fictitious source distribution over the cavity surface is denoted by  $\psi(\mathbf{x}')$ . The integral kernel,  $g_1$ , is the scalar Green's function in an infinite homogeneous medium which is of the well-known form

$$g_1(\mathbf{x}, \mathbf{x}') = \frac{e^{ik_f |\mathbf{x} - \mathbf{x}'|}}{4\pi |\mathbf{x} - \mathbf{x}'|}, \quad (2)$$

where  $k_f = \omega/c$  is the wavenumber for the fluid.

The above representation is not only physically intuitive but also mathematically rigorous. In fact, this representation can be obtained from the mathematical formulation of Huygen's principle with assistance of the uniqueness and equivalence principles. That is, the influence of the elastic medium on the wavefield inside the cavity is equivalent to impressing a sheet of fictitious sources on the boundary between the fluid and the elastic medium. Fictitious source distribution density is the unknown function to be determined.

For the source-free elastic medium outside the cavity, the displacement field can be expressed as

$$\mathbf{U}_2(\mathbf{x}) = \int_B dS' \overline{\mathbf{G}}(\mathbf{x}, \mathbf{x}') \cdot \Psi(\mathbf{x}') \quad \text{for } \mathbf{x} \in V_e + B, \quad (3)$$

where  $\Psi(\mathbf{x}')$  is a vector fictitious source distribution on the boundary.  $\overline{\mathbf{G}}(\mathbf{x}, \mathbf{x}')$  is the dyadic Green's function for displacement and has the following form

$$\overline{\mathbf{G}}(\mathbf{x}, \mathbf{x}') = \frac{1}{\rho\omega^2} \left\{ k_\beta^2 \overline{\mathbf{I}} g_\beta(\mathbf{x}, \mathbf{x}') + \nabla \nabla [g_\beta(\mathbf{x}, \mathbf{x}') - g_\alpha(\mathbf{x}, \mathbf{x}')] \right\}. \quad (4)$$

Here,  $g_\alpha$  and  $g_\beta$  are scalar Green's functions of the same form as in (2) except that  $k_f$  is

changed to  $k_\alpha$  for the dilatational wave and to  $k_\beta$  for the shear wave. Equation (3) says that the displacement in the region outside the cavity, ( $V_e$ ), results from vector fictitious sources distributed along the boundary. For axially symmetrical problems in cylindrical coordinates, the vector fictitious source can be decomposed into source distributions in radial and vertical directions. Therefore, we have two unknown distribution functions to determine in order to calculate the displacement field in the elastic medium. Uniqueness of the calculated displacement is guaranteed by the equivalence principle and more fundamentally by the uniqueness theorem.

### Implementation of the Indirect BEM

The essence of the indirect BEM implementation is to discretize the boundary between cavity fluid and surrounding formation into a set of small-sized surfaces called elements. Each element is a ring-shaped surface with height  $dz$  and cavity radius  $r_0$ . Density of the fictitious source is assumed to be constant on each element. From our previous boundary integral formulation, it is seen that a fictitious volume source for the fluid and a fictitious source vector for the elastic medium are needed in order to uniquely describe the cavity source radiation. The fictitious source vector in an axially symmetrical system consists only of the vertical and radial components. Therefore, we have on each element  $i$  three unknowns to determine the following: a fictitious fluid volume source,  $V_i^f$ ; a vertical source for elastic medium,  $F_i^v$ ; and a radial source for elastic medium,  $F_i^r$ . Our goal is to obtain

these sources on each element so that displacement fields in the elastic medium or the fluid can be calculated.

The number of elements is restricted by the computing power of current computers and the accuracy specified. In practice, three elements per shortest wavelength are used, and the number of elements depends on the time window and the fastest wave speed. Thus, the element height  $dz$  satisfies

$$dz \leq \frac{\min(c, \beta, \alpha)}{3f}, \quad (5)$$

and the number of elements,  $N_e$ , is given by

$$N_e = \frac{t_{max} \times \max(c, \beta, \alpha)}{dz} = \frac{3f \times t_{max} \times \max(c, \beta, \alpha)}{\min(c, \beta, \alpha)}. \quad (6)$$

In the above, the frequency and maximum time to be calculated for are denoted, respectively, by  $f$  and  $t_{max}$ . At each element, the usual fluid/elastic boundary conditions have to be satisfied: i.e., continuity of normal displacements and continuity of normal stress and vanishing tangential stress of the solid,

$$\begin{aligned} U_r|_{r=r_0^+} - U_r|_{r=r_0^-} &= 0 \\ \sigma_{rr}|_{r=r_0^+} - \sigma_{rr}|_{r=r_0^-} &= 0 \\ \sigma_{rz}|_{r=r_0^+} &= 0. \end{aligned} \quad (7)$$

These boundary conditions are satisfied at the center of each element. Displacements and stresses (or pressure) at the center of each element result from contributions from fictitious sources of all the elements. To calculate the displacement at the  $j$ -th element due to the

source at the  $i$ -th element, we use the indirect formulations (1) and (3). At the  $j$ -th element, the boundary conditions become

$$\begin{aligned} \sum_{i=1}^{N_e} A_{ji}^f V_i^f + \sum_{i=1}^{N_e} A_{ji}^v F_i^v + \sum_{i=1}^{N_e} A_{ji}^r F_i^r &= D_j^u \\ \sum_{i=1}^{N_e} B_{ji}^f V_i^f + \sum_{i=1}^{N_e} B_{ji}^v F_i^v + \sum_{i=1}^{N_e} B_{ji}^r F_i^r &= D_j^{\sigma rr} \\ \sum_{i=1}^{N_e} C_{ji}^v F_i^v + \sum_{i=1}^{N_e} C_{ji}^r F_i^r &= D_j^{\sigma rx}. \end{aligned} \quad (8)$$

In the above,  $A_{ji}^f$ ,  $A_{ji}^v$  and  $A_{ji}^r$  represent displacements at the  $j$ -th element due to the cylindrical volume, and the vertical and radial ring sources of unit strength at the  $i$ -th element, respectively. They are integrals of the Green's functions with respect to the surfaces of cavity ('bottom + wall). The  $B$ 's and  $C$ 's are the radial and tangential stresses at the  $j$ -th element due to sources at the  $i$ -th element. They are the integrals of the stress Green's function. The  $D$ 's are exciting fields indicated by their superscripts at the  $j$ -th element. With  $j$  ranging from 1 to  $N_e$ , we obtain  $3 \times N_e$  equations that can be easily solved for the  $3 \times N_e$  unknowns. With these fictitious source densities determined, fields inside and outside of the cavity can be easily obtained using equations (1) and (3).

Integration of the Green's functions is done in two steps. First, using the Sommerfeld integral representation for function  $e^{ikR}/R$ , we transform the Green's functions into integrals with respect to horizontal wavenumber. The use of Sommerfeld integral representation allows us to incorporate vertical layering in a later study. The  $r_0 d\varphi$  part of surface integration greatly simplifies the integrand of the wavenumber integral due to axial symmetry. Then the

$dz$  part (for wall elements) and the  $dr_0$  part (for bottom elements) of the surface integral can be analytically evaluated. The integration of the Green's function is reduced to a horizontal wavenumber integral. Second, this wavenumber integral is evaluated using the discrete wavenumber method (Bouchon, 1981) by summation over the horizontal wavenumber.

The coefficient matrix of the equation system (8) is a fully populated complex matrix and is non-symmetrical. This is often regarded as the disadvantage of BEM as compared to FEM or FDM. In the latter two methods, tridiagonal matrices are obtained and a special faster algorithm exists for this kind of matrix. Nevertheless, this matrix can still be easily manipulated as the number of elements is not exceedingly high and the system of equations is only solved once for each frequency.

## Results

The situation of a seismic source in a finite cavity/borehole arises in nuclear explosions in tunnels, or in a borehole seismic experiment near the bottom of a borehole. Most likely, in the first case the tunnel is filled by air (or empty), and in the second the borehole is filled by water. In either case, the finiteness of the borehole/cavity will play a role in the far field radiation pattern of the seismic waves. The BEM technique outlined above can be used to study the wave radiation from this special source geometry. Some steps involved in the BEM modeling are illustrated. The influence of a finite borehole on  $P$  and  $S$  wave radiation is demonstrated.

For a finite tunnel, the wall of the tunnel as well as both its ends have to be discretized into elements (See Figure 1). On each of these elements, we need to determine the fictitious sources on the solid side and on the fluid side of the interface. The requirement of the three boundary conditions leads to a system of equations, and these sources can thus be determined. In a homogeneous medium, this BEM technique is very fast due to the following considerations:

- Let  $N_{we}$  be the number of wall elements. Wall-to-wall element interactions need not be calculated for each of the  $N_{we}$  radiating elements and each of the  $N_{we}$  receiving elements, which would involve  $N_{we} \times N_{we}$  evaluation of a wavenumber integral. Instead, calculating the interaction of one receiving element with all  $N_{we}$  radiating elements, which incurs only  $N_{we}$  evaluation of integrals, is sufficient. This is because of the permutation and symmetry properties of the displacement and stress integrals when radiating and receiving elements are shifted and interchanged.
- If we call one end of the tunnel the bottom, and the other the top, the interactions between each top element and each bottom element and their self-interactions can be computed as efficiently as those of the wall elements.
- No symmetry property can be used for computing wall-to-top element interaction. But, once this is done, the wall-to-bottom interaction can be copied from the wall-to-top calculations.

These considerations yield a tremendous saving of computation time.

To demonstrate the effect of the finite cavity on wave radiation from an explosion source, two situations that are applicable to nuclear and non-nuclear explosions in an isotropic homogeneous space are considered. For a nuclear explosion, we consider that the compressional velocity inside the cavity is the shock wave velocity. The shock wave velocity is taken as 10 km/sec (Lamb *et al.*, 1992). For a non-nuclear (i.e., chemical) explosion, the compressional velocity inside the cavity is 330 m/sec (sound speed in air). We choose an isotropic medium with a *P* velocity of 4.0 km/s, a *S* velocity of 2.2 km/s, and a density of 2.2 g/cm<sup>3</sup> as a homogeneous background model. Four tunnels are considered: 40 meters long with a 5 meter radius, 40 m long with a 10 m radius, 80 m long with a 5 m radius, and 80 m long with a 10 m radius. The receivers are circularly and evenly distributed around the source at a distance of 5 kilometers from the center of the tunnel (see Figure 1). For comparison with the radiation patterns of sources in finite cavity, Figure 2 provides the *P* and *S* wave radiation patterns for an explosion source in an air-filled infinite cylindrical cavity.

Figures 3 and 4 show the radial and tangential components for the explosion source placed at 1 and 18 meters, respectively, from one end of the tunnel with a 5 meter radius and 40 meter length. In this case, the compressional velocity inside the tunnel is chosen as air. The center frequency is 1 Hz. These figures display the seismograms and the radiation pattern of the waves simultaneously. The radial seismograms show the radial particle motion and hence the *P* wave radiation. The tangential seismograms show the transverse motion, i.e.,

the shear wave radiation. Figure 5 shows the seismograms from a nuclear explosion (shock wave velocity inside cavity) located 18 meters from one end of the tunnel. The maximum displacement of the *P* and *S* wave at the receivers for two center frequencies (1 and 2 Hz) is plotted in Figures 6 through 13 for nuclear and non-nuclear explosions at various positions along the tunnel axis.

Figures 3 through 13 show that, when an explosion source is at the center of a finite cylindrical tunnel, its *S* wave radiation pattern is basically the same as that of an explosion source in an infinite borehole (Heelan, 1953; Lee and Balch, 1982; Meredith, 1990). The *P* wave radiation pattern, on the other hand, is close to that of a force along the cavity axis. Slightly away from the center of the cylindrical cavity, the *S* radiation pattern of a non-nuclear explosion (air velocity) changes drastically. Near the end of the tunnel, *S* and *P* wave radiation patterns from a non-nuclear explosion are essentially those of a single force along the tunnel axis, and the radiated waves have their maximum amplitude when the source is close to the tunnel end. In contrast, the nuclear explosion (shock wave velocity inside the cavity) produces similar radiation patterns for different source positions along the axis of the cylinder. Shear waves are generated at each position, with the shear wave amplitude varying slightly with the position of the source especially at the end of the cavity. The dipole source pattern of shear wave radiation is very consistent for all the examples.

Both ends of the tunnel are responsible for these peculiar radiation patterns. Energy from an explosion is mostly trapped as tube waves. The impact of the direct wave and

the tube wave on both ends of the cavity is much stronger than on the cavity wall. When the explosion source is at the center, both ends experience the same pressure at the same time, and in the far field they act like a single force couple. This results in an *S* wave radiation pattern similar to that of an infinite borehole. The *P* wave pattern results from the fact that receivers close to one end of the cavity detect more *P* wave energy from this end than from the other. As the source moves away from the center, one end of the tunnel dominates, resulting in the kinds of radiation patterns observed especially for a non-nuclear explosion. For nuclear explosions, the high-speed propagation velocity inside the cavity could not produce the asymmetric results seen in the case of non-nuclear sources. In this case, the entire tunnel surface radiates energy at the same time as a volume source.

## Conclusions

A general numerical algorithm based on the boundary element method has been used to model seismic waves radiated from explosion sources inside finite, cylindrical tunnels. This method has the capability to calculate both near-field and far-field radiation and the scale difference is properly dealt with. We computed source radiation patterns for two different explosion source types placed along the axis of a finite tunnel. The radiation patterns from non-nuclear sources depend strongly on the position of the source along the axis. Sources near the tunnel wall produce the highest amplitudes and behave like a simple point force. Radiation patterns from nuclear sources do not vary significantly with source position owing

to the very high compressional velocity inside the tunnel. All the sources and source positions considered produced significant shear waves, showing that a finite cylindrical cavity provides a mechanism for shear wave generation from explosions.

## References

Bouchon, M., 1981, A simple method to calculate Green's functions for elastic layered media, *Bull. Seism. Soc. Am.*, **71**, 959–971.

Bouchon, M., 1993, A numerical simulation of the acoustic and elastic wavefields radiated by a source in a fluid-filled borehole embedded in a layered medium, *Geophysics*, **58**, 475–481.

Bouchon, M., Campillo, M., and Gaffet, S., 1989, A boundary integral equation-discrete wavenumber representation method to study wave propagation in multilayered media having irregular interfaces, *Geophysics*, **54**, 1134–1140.

Bouchon, M., and Schmitt, D.P., 1989, Full-wave acoustic logging in an irregular borehole, *Geophysics*, **54**, 758–765.

Campillo, M., and Bouchon, M., 1985, Synthetic SH-seismograms in a laterally varying medium by the discrete wavenumber method, *Geophys. J. Roy. astr. Soc.*, **83**, 307–317.

Cruse, T.A., 1968, A direct formulation and numerical solution of the general transient elastodynamic problem. I: *J. Math. Anal. Appl.*, **22**, 341–355.

Day, S.M., N. Rimer, and J.T. Cherry, 1983, Surface waves from underground explosions

with spall: analysis of elastic and nonlinear source models, *Bull. Seism. Soc. Am.*, **84**, 247–264.

Dong, W., 1993, Elastic wave radiation from borehole seismic sources in anisotropic media, Ph.D. Thesis, Massachusetts Institute of Technology.

Glenn, L.A., A.J.C. Ladd, B. Moran and K.A. Wilson, 1985, Elastic radiation from explosively-loaded ellipsoidal cavities in an unbounded medium, *Geophys. J. R. astr. Soc.*, **81**, 231–241.

Gupta, I.N. and R.R. Blandford, 1983, A mechanism for generation of short-period transverse motion from explosions, *Bull. Seism. Soc. Am.*, **73**, 571–591.

Heelan, P.A., 1953, Radiation from a cylindrical source of finite length, *Geophysics*, **18**, 685–696.

Helmberger, D., L. Burdick and R. Stead, 1991, Modeling near-field data at NTS and Amchitka, *AGU Geophysical Monograph Series*, **65**, 35–45.

Jawson, M.A., 1963, Integral equation methods in potential theory. I: *Proc. Roy. Soc. London, A*, **275**, 23–32.

Johnson, L.R., 1988, Source characteristics of two underground nuclear explosions, *Geophys. J.*, **95** 15–30.

Kawase, H., 1988, Time domain response of a semicircular canyon for incident SV, P, and Rayleigh waves calculated by the discrete wavenumber boundary element method, *Bull. Seism. Soc. Am.*, **79**, 1361–1382.

Lamb, F.K., B.W. Callen, and J.D. Sullivan, 1992, An approximate analytical model of shock waves from underground nuclear explosions, *J. Geophys. Res.*, **97**, 515–535.

Latter, A.L., R.E. LeLevier, E.A. Martinelli and W.G. McMillan, 1961, A method of concealing underground nuclear explosions, *J. Geophys. Res.*, **66**, 943–946.

Lee, M.W., and A.H. Balch, 1982, Theoretical seismic wave radiation from a fluid-filled borehole, *Geophysics*, **47**, 1308–1314.

Massé, B.P., 1981, Review of seismic source models for underground nuclear explosions, *Bull. Seism. Soc. Am.*, **71**, 1249–1268.

Meredith, J.A., 1990, Numerical and analytical modeling of downhole seismic sources: the near and far field, Ph.D. Thesis, Massachusetts Institute of Technology.

Priestley, K.F., W.R. Walter, V. Martynov and M.V. Rozhkov, 1990, Regional seismic recordings of the Soviet nuclear explosion of the joint verification experiment, *Geophys. Res. Lett.*, **17**, 179–182.

Rial, J.A. and B. Moran, 1986, Radiation patterns for explosively-loaded axisymmetric cavities in an elastic medium: analytic approximations and numerical results, *Geophys. J. R. astr. Soc.*, **86**, 855–862.

Rizzo, F.J., 1967, An integral equation approach to boundary value problems of classical elastostatics, *Q. Appl. Math.*, **25**, 83–95.

Sánchez-Sesma, F.J., and M. Campillo, 1991, Diffraction of P, SV, and Rayleigh waves by topographic features: a boundary integral formulation, *Bull. Seism. Soc. Am.*, **81**, 2234–

2251.

Symm, G.T., 1963, Integral equation methods in potential theory. II: *Proc. Roy. Soc. London, A*, 275, 33-46.

Wallace, T.C., D.V. Helmberger, and G.R. Engen, 1983, Evidence of tectonic release from underground nuclear explosions in long-period P waves, *Bull. Seism. Soc. Am.*, 73, 593-613.

Wallace, T.C., D.V. Helmberger, and G.R. Engen, 1985, Evidence of tectonic release from underground nuclear explosions in long-period S waves, *Bull. Seism. Soc. Am.*, 75, 157-174.

Wong, H.L., 1982, Effect of surface topography on the diffraction of P, SV and Rayleigh waves, *Bull. Seism. Soc. Am.*, 72, 1167-1183.

Zhao, L. and D.G. Harkrider, 1992, Wave fields from an off-center explosion in an embedded solid sphere, *Bull. Seism. Soc. Am.*, 82, 1927-1955.

# FINITE TUNNEL

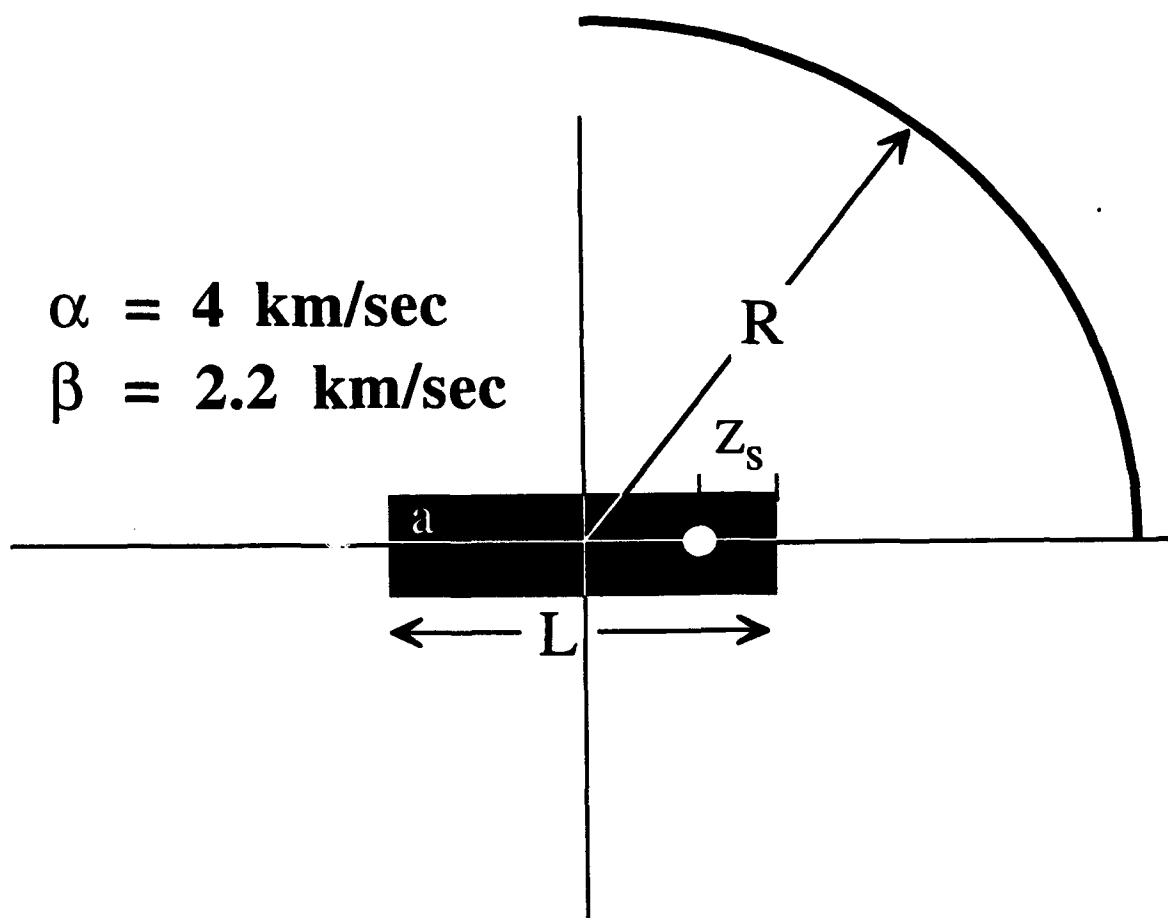


Figure 1: Schematic diagram of the element of the tunnel and the source and receivers configurations.

## *Infinite Cylindrical Cavity*

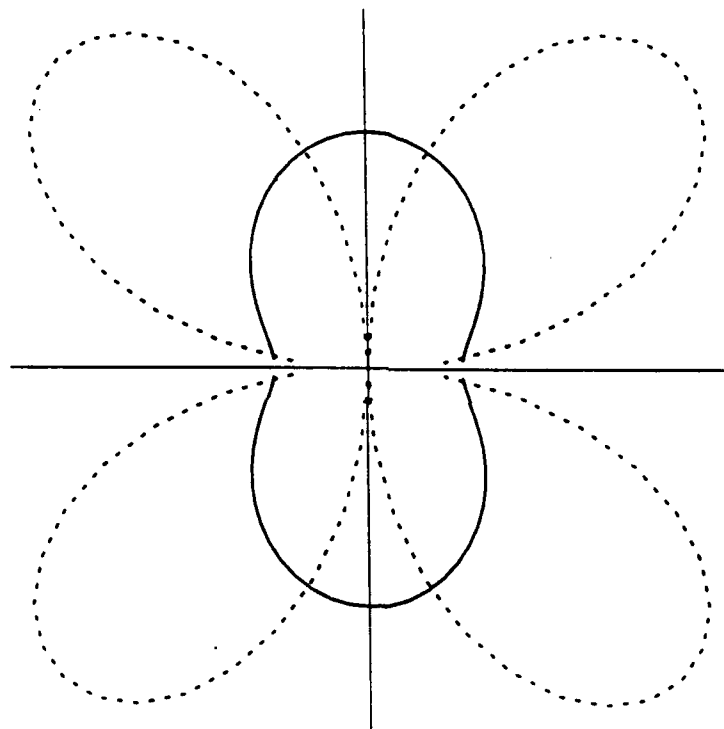
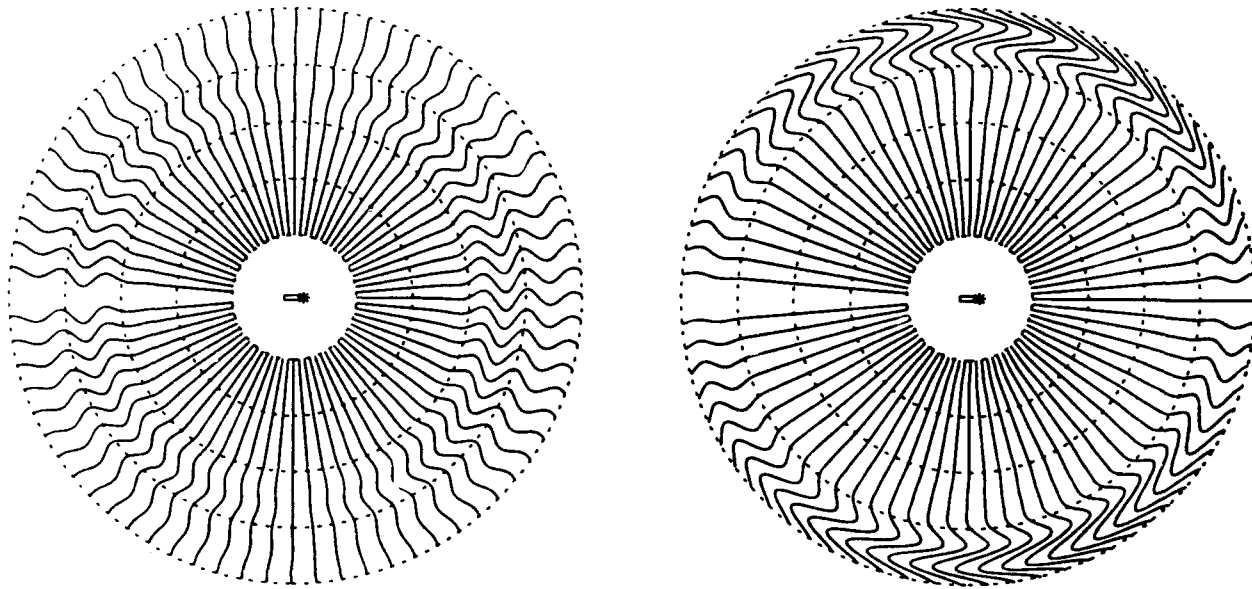


Figure 2: Analytical  $P$  (solid line) and  $SV$  (dashed line) wave radiation pattern for an explosion source at the center in an infinite air-filled cylindrical cavity.



*Radial*

*Tangential*

Radius = 5. meter

Length = 40. meter

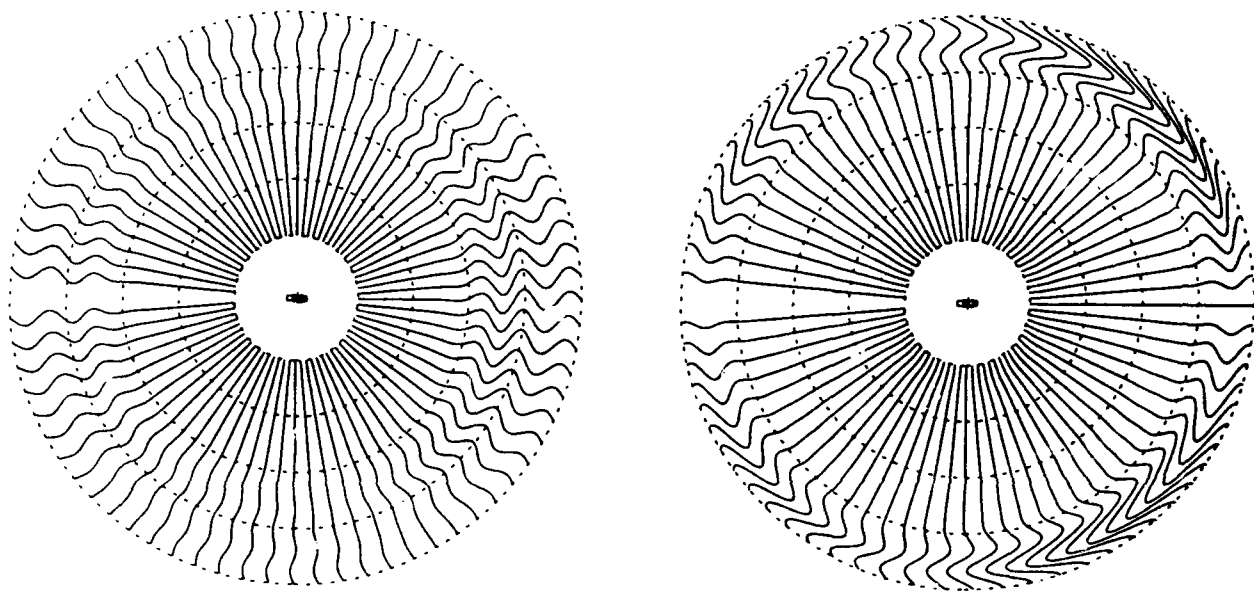
Zs = 1. meter

Rr = 5000. meter

f\_c = 1. Hz

A\_max = 0.15207713E-09

Figure 3: Radial and tangential seismograms at a distance of 5 km from a finite tunnel with a length of 40 meters and a 5 meter radius. The center frequency is 1 Hz. The source is placed 1 meter from one end of the tunnel. The compressional velocity inside the tunnel is 330 m/sec (air).



*Radial*

Radius = 5. meter

Length = 40. meter

Zs = 18. meter

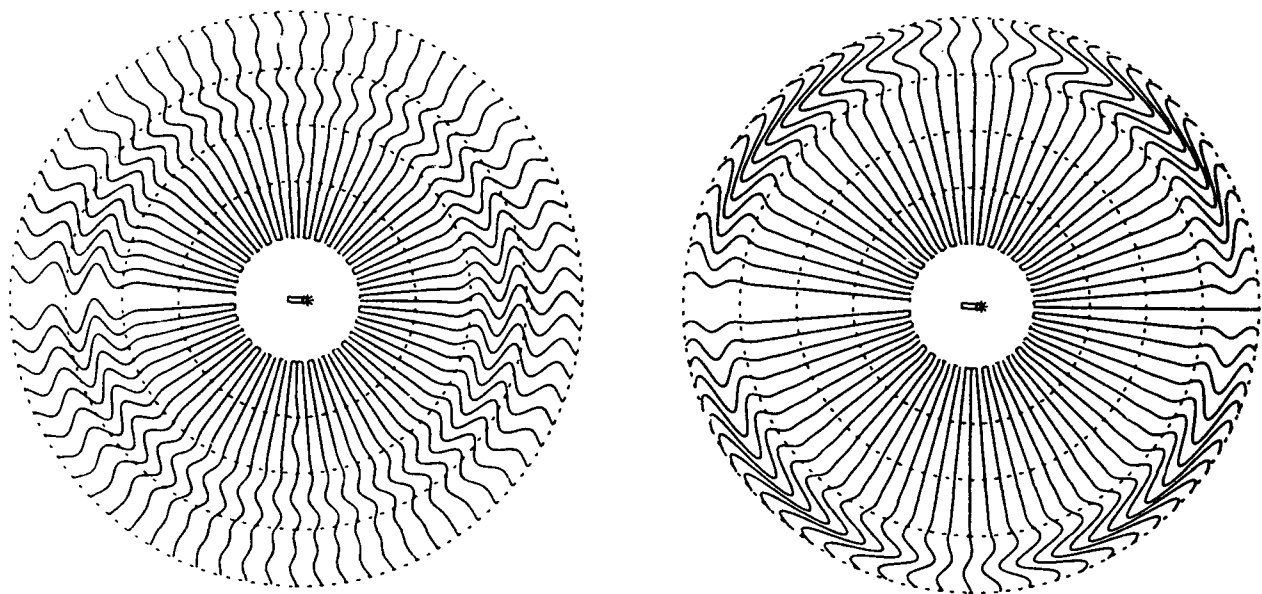
Rr = 5000. meter

f\_c = 1. Hz

A\_max = 0.26047033E-10

*Tangential*

Figure 4: Same as described in Figure 3 but the source is 18 meters from one end of the tunnel.



*Radial*

*Tangential*

Radius = 5. meter  
 Length = 40. meter  
 Zs = 1. meter  
 Rr = 5000. meter  
 f\_c = 1. Hz  
 A\_max = 0.14442876E-11

Figure 5: Same as described in Figure 3 but the compressional velocity inside the tunnel is 10 km/sec as shock wave (nuclear explosion).

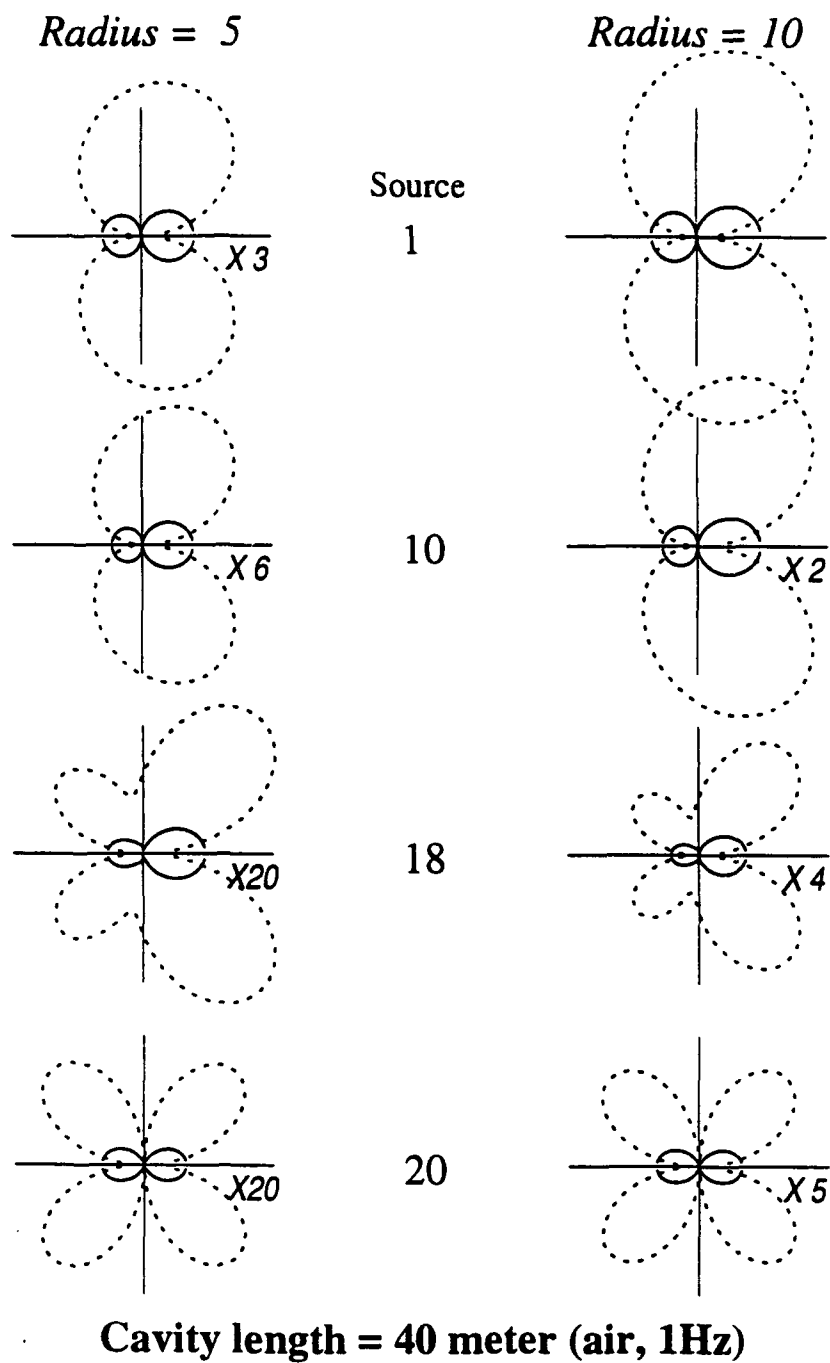
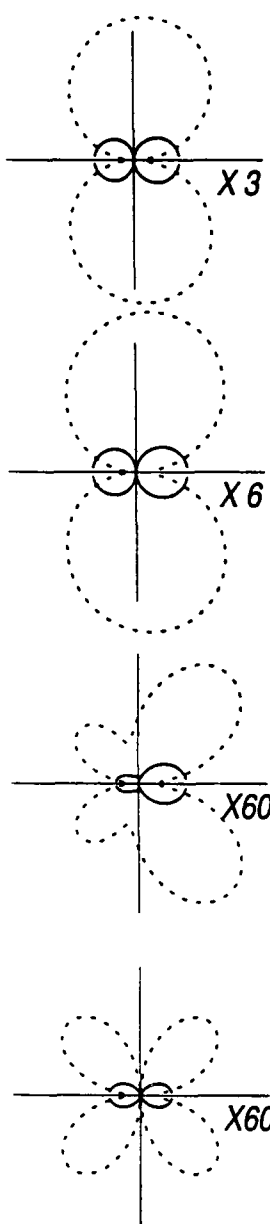


Figure 6: Radiation pattern of P and S waves from a finite tunnel of length 40 meters for different source positions along the tunnel with *compressional velocity 330 m/sec (non-nuclear source)*. The center frequency of the waveforms is 1 Hz. The left column shows the results for the tunnel with a 5 meter radius and the right column is for a 10 meter radius. The source position from one end of the tunnel is also shown in the middle column. The amplitudes are plotted on the same scale, but the multiplication factor (e.g.,  $x3$  for radius 5 and source position 1 meter from the end of the tunnel) is also shown where required.

*Radius = 5*



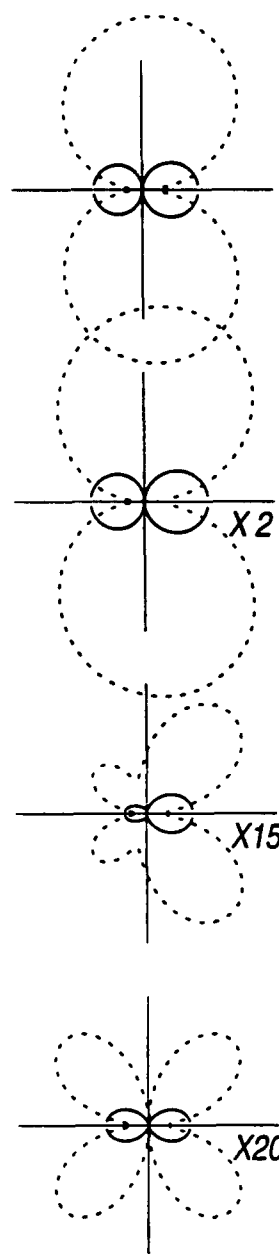
*Radius = 10*

Source  
1

10

38

40



**Cavity length = 80 meter (air, 1Hz)**

Figure 7: Same as described in Figure 6 from an 80 meter long finite tunnel.

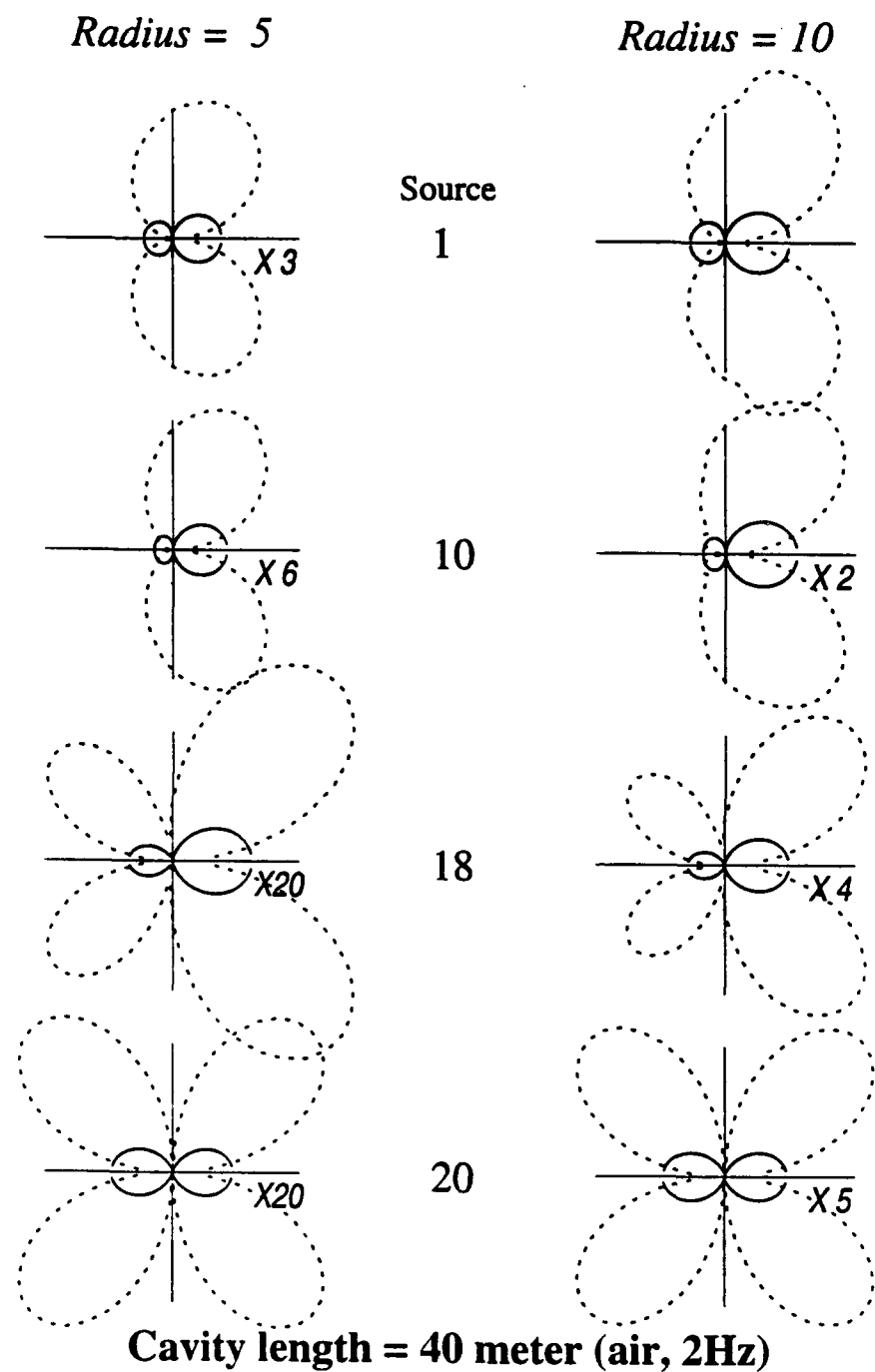
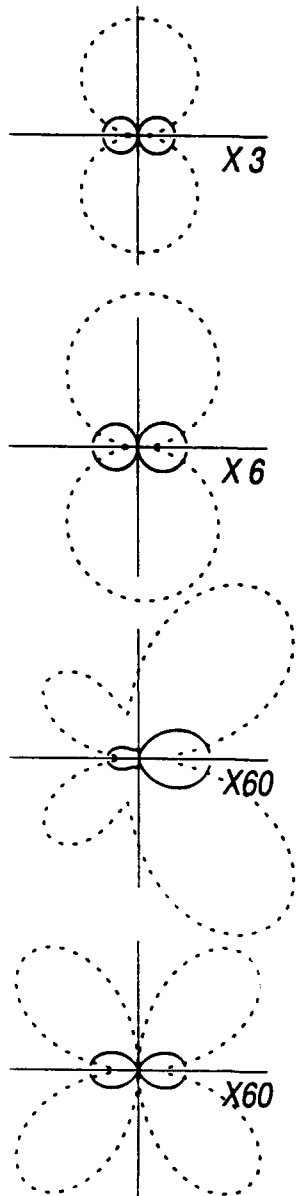


Figure 8: Same as described in Figure 6. The center frequency is 2 Hz.

*Radius = 5*



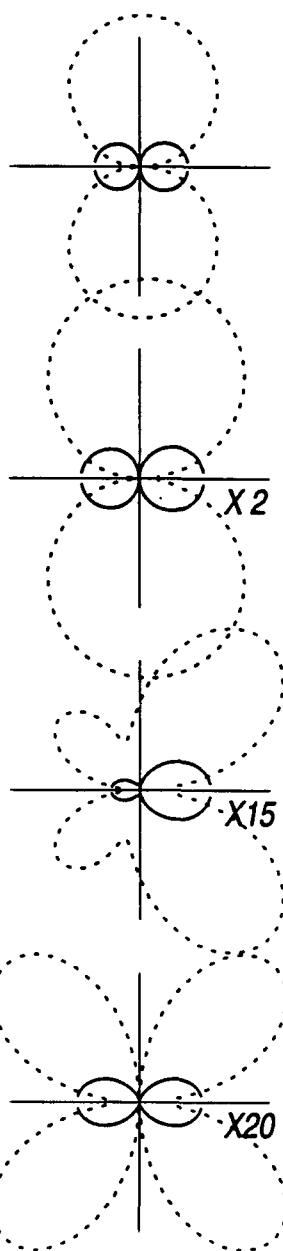
*Radius = 10*

Source  
1

10

38

40



**Cavity length = 80 meter (air, 2Hz)**

Figure 9: Same as described in Figure 7. The center frequency is 2 Hz.

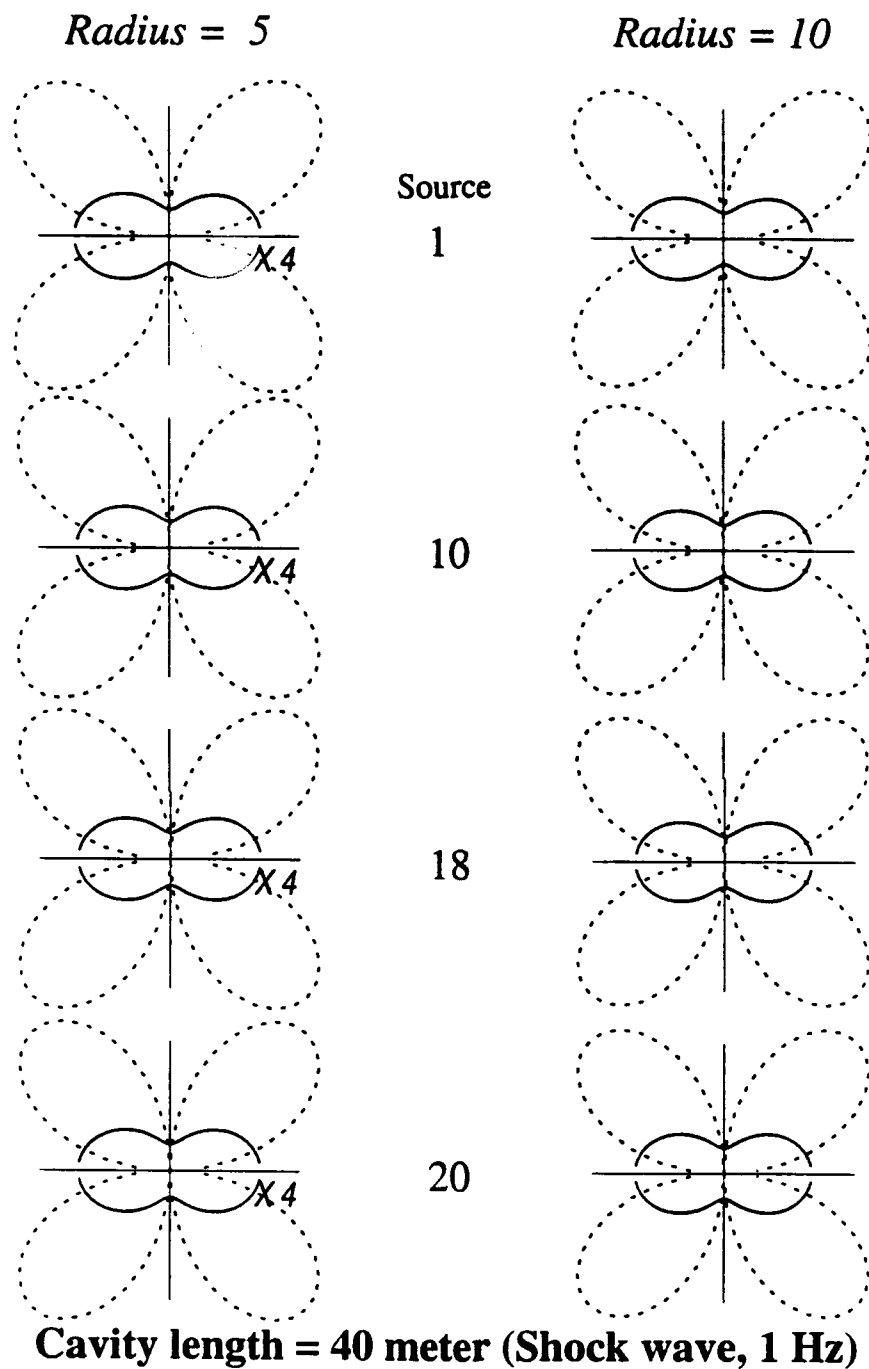


Figure 10: Same as described in Figure 6. The compressional velocity inside the tunnel is 10 km/sec as shock wave (*nuclear explosion*).

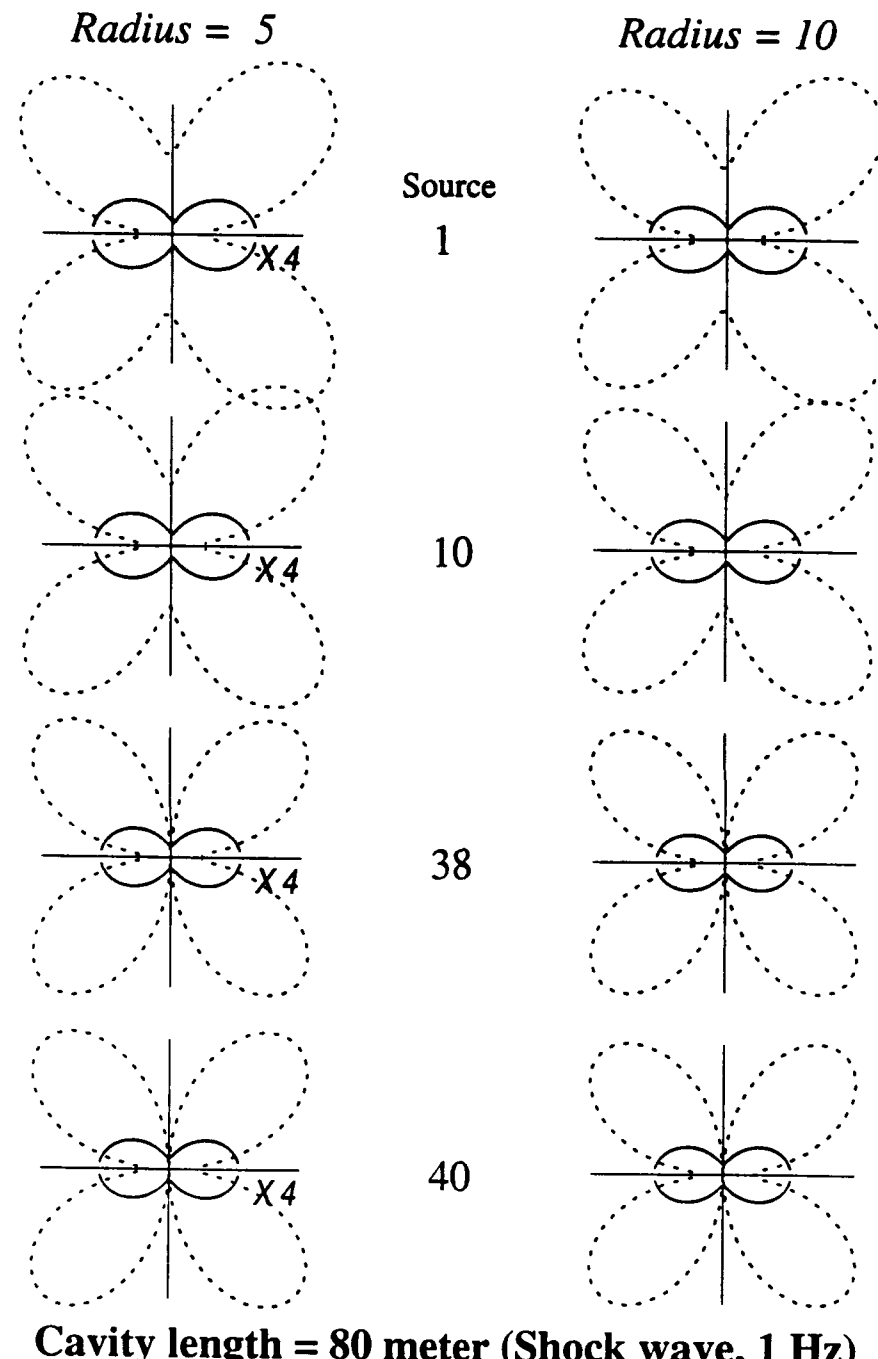


Figure 11: Same as described in Figure 10 from an 80 meter long finite tunnel.

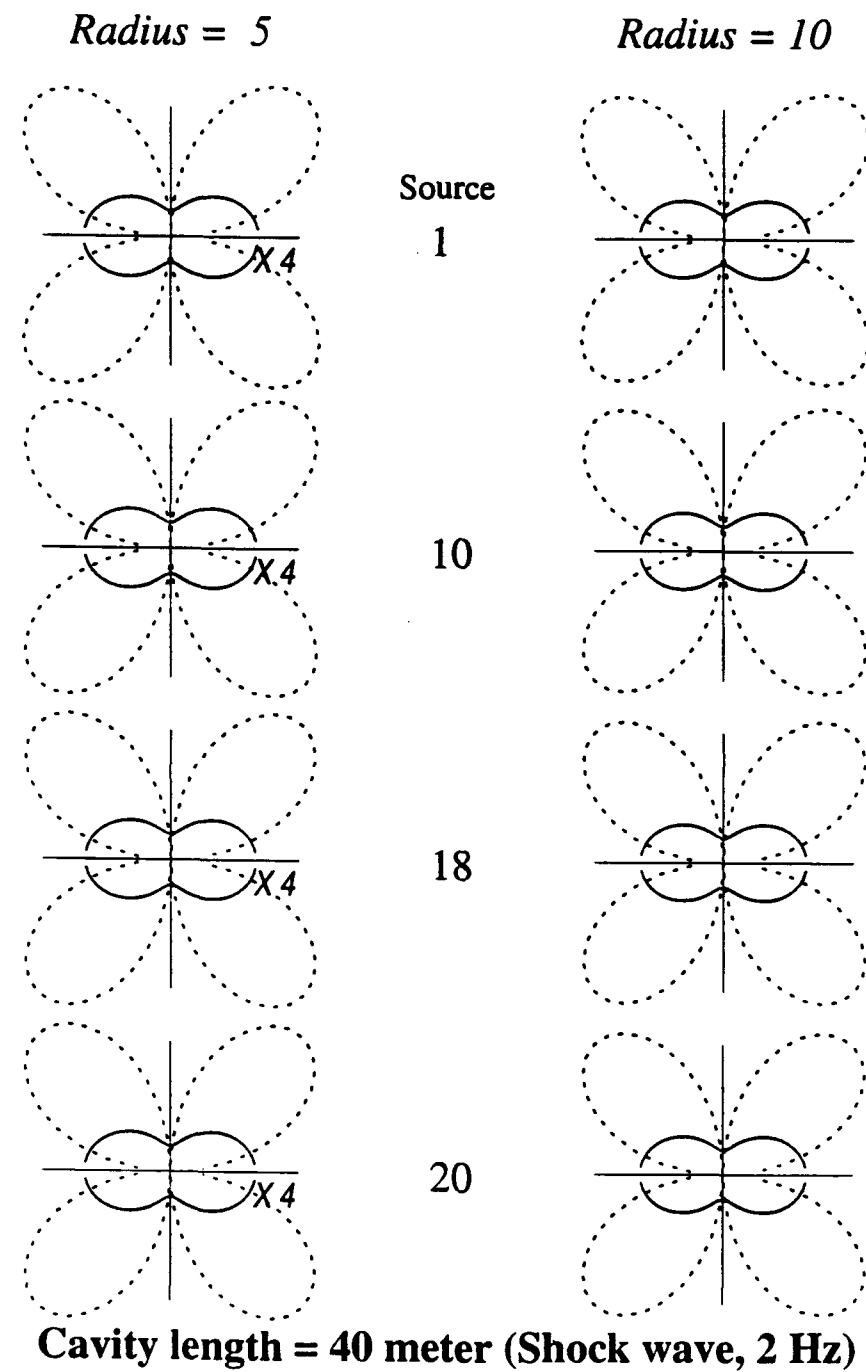
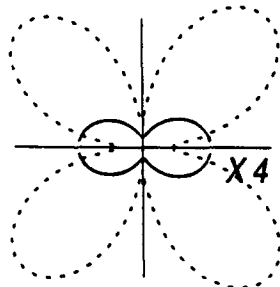
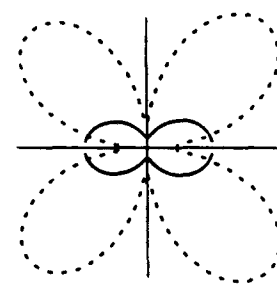


Figure 12: Same as described in Figure 10. The center frequency is 2 Hz.

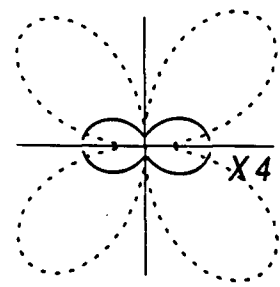
*Radius = 5*



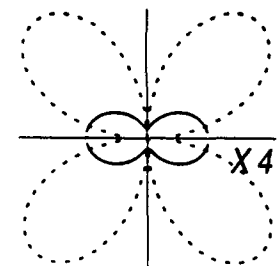
*Radius = 10*



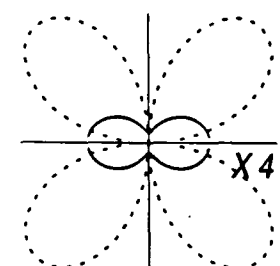
Source  
1



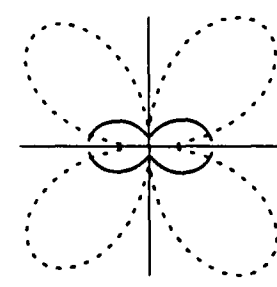
10



38



40



**Cavity length = 80 meter (Shock wave, 4 Hz)**

Figure 13: Same as described in Figure 11. The center frequency is 2 Hz.

# EXPERIMENTAL STUDY OF SCATTERING FROM A HIGHLY IRREGULAR, ACOUSTIC-ELASTIC INTERFACE

## Summary

In this study, we experimentally and numerically investigate the scattering of an acoustic P wave incident on a highly irregular, random acoustic-elastic interface to determine whether enhanced backscattering, already identified numerically for SH and P-SV waves, occurs. Numerically, the problem is solved by coupling the Somigliana identity for an elastic medium with Green's second integral theorem for pressure in a fluid. Exact integral expressions for the scattered pressure in the acoustic medium are then obtained. Experimentally, a glass etching process using photoresist templates with Gaussian statistics allowed for the generation of a characterized random interface. This 3-D interface has approximately a Gaussian correlation function and a Gaussian height distribution. A method was also developed by which identical interface geometries with differing material contrasts can be physically created. This approach involved using the glass surface as an epoxy mold. Experiments were carried out on the glass surface in M.I.T.'s Earth Resources Laboratory's ultrasonic laboratory. Two-dimensional numerical results predict the 3-D experimental results well at small incident angles. Both numerical and experimental results strongly support the presence of "enhanced backscattering." However, more experiments are required to fully constrain the properties of the retroreflective peak. Finally, fundamental differences between 2-D and 3-D

scattering mechanisms appear to form at larger incident angles.

## Introduction

In laboratory experimentation a lack of control over the statistical parameters of a given random model can easily make experimental results ambiguous. In the case of irregular interfaces, the height probability distribution and the correlation lengths of the interface may not be well constrained, the interface may not be stationary in space, and the interface may contain a wide variety of length scales. Each of these experimental uncertainties makes comparisons with numerical models difficult, if not impossible. It is the goal of this project to physically fabricate a random interface which is stationary in space with both a simple height probability distribution and a simple transverse correlation function so that these experimental results can be easily compared with the corresponding numerical results.

Experimentally, the accurate generation of a Gaussian surface is very important since Gaussian interfaces are mathematically convenient and widely used in scattering studies. Many theoretical formulations in the literature apply the simple properties of a Gaussian correlation function to random surfaces. Examples can be found in Prange and Toksöz (1990), Knopoff and Hudson (1964, 1967), Haddon (1978), and Kuperman and Schmidt (1989). Exponential correlation functions have also been used extensively (e.g, Wu and Aki, 1985; Frankel and Clayton, 1986) and in many instances give a good description of field observations.

In this study, we choose to fabricate and model an interface with a Gaussian correlation function. The statistical parameters of the interface are chosen so that the incident wavelength has the same length scale as the correlation length of the irregularities. In addition, the average slope of the interface is large and the approximate techniques such as the Kirchoff, Born, and the geometrical ray approach, break down into multiple scattering mechanisms such as “enhanced backscattering” and “shadowing,” and play strong roles in wave scattering.

What is enhanced backscattering from an acoustic-elastic halfspace? By definition, enhanced backscattering or ‘retroreflectance’ is the enhancement of energy scattered back in the direction of the source. O’Donnell and Mendez (1987) were the first to propose the hypothesis that time-reversed paths were responsible for enhanced backscattering. This hypothesis was further strengthened by Maradudin *et al.* (1991) who showed that retroreflectance for energy double scattered from the interface. More support came from Schultz and Toksöz (1993b), who showed that full elastic seismic scattering is consistent with this hypothesis since enhancement is observed on P-to-P and S-to-S scattering and not on P-to-S and S-to-P scattering. The extension of time-reversed paths is easily extended to the acoustic-elastic case. Take for instance the peak-valley sequence shown in Figure 1. If an incident P-wave, shown by the solid line, diffracts from point 1, it will propagate as a P-wave to point 2 and then diffract at some angle into the upper medium again as a  $P'$ -wave. For most waves travelling away from the interface, enhancement will not occur. However, if the diffracted

wave travels directly back towards the source, an incident P-wave can be found travelling exactly in the reverse path—propagating from point 2 to point 1 and again travelling back towards the source as shown by the dashed line. In this case, the time-reversed path interferes constructively with the forward path and contributes additional energy towards the source, resulting in enhanced backscattering. Using a simple phase argument, some properties of enhanced backscattering can be derived. The peak width can be written as  $\Delta\theta_s = \frac{\lambda}{2l}$ , where  $\Delta\theta_s$  is the angular width of the peak,  $\lambda$  is the incident wavelength, and  $l$  is the mean free path of the interface or, in other words, the average distance a wave propagates between points 1 and 2 along the interface.

Using this phase approach other path geometries may also contribute to enhanced backscattering. For example, if a wave encounters the interface and multiply scatters three times as a P-wave to send energy back in the direction of the source, then a time-reversed path may be found that also sends energy back towards the source. In the same manner, many multiply scattered paths sending energy back towards the source can be found in the acoustic-elastic case. However, as a result of energy loss with each diffraction from the interface due to both transmission through the interface and additional spreading, it seems reasonable that the double-scattered path contributes the majority of retroreflective energy.

In this paper, we first briefly summarize the numerical formulation used to model scattering from a randomly irregular acoustic-elastic interface. This Somigliana identity approach is based on the work of Schultz and Toksöz (1993a,b). Next, the construction of the ran-

dom glass surface is discussed and the ultrasonic apparatus for measuring the scattering properties of the interface is then described. The third section compares the experimental scattering results obtained in our in-house ultrasonic water tank with the numerical models. The scattering properties are discussed in detail along with a discussion of probable scattering mechanisms. Finally, we discuss the differences between the 2-D synthetic results and the 3-D experimental data. We then propose possible differences between 2-D and 3-D scattering mechanisms.

## Theory

The numerical approach described in this section and the notation used, follows that of Schultz and Toksöz (1993a,b). Since the approach here is very similar to the SH and P-SV cases, we give only a brief outline of the theoretical approach. We first express the total scattered displacement at any point within two volumes of elastic material exactly with the Somigliana representation theorem (e.g.. Aki and Richards, 1980). Simplifying this theorem to a 2-D case gives a set of four integral equations

$$\begin{aligned}
 H[1]u_n^{(l)}(\underline{x}) = & \int_V f_p^{(l)}(\underline{\eta})G_{np}^{(l)}(\underline{x}; \underline{\eta})dV(\underline{\eta}) \\
 & -(-1)^i \int_S dS(\underline{x}') \{ [c_{ijpq}^{(l)} \hat{n}_j(\underline{x}') \partial G_{np}^{(l)}(\underline{x}; \underline{x}') / \partial x'_q] u_i^{(l)}(\underline{x}') \\
 & - G_{np}^{(l)}(\underline{x}; \underline{x}') T_p^{(l)}(\underline{u}^{(l)}(\underline{x}'), \hat{n}) \},
 \end{aligned} \tag{9}$$

where gradients are zero in the  $x_2$ -direction. Following the notation of Schultz and Toksöz (1993b),  $T_p^{(l)}(\underline{x})$  is the traction vector along the interface in the fluid ( $l = f$ ) and the solid ( $l = s$ ), and we have assumed all surfaces are far enough away that only the surface,  $S(\underline{x})$ , separating the two volumes, contributes to the final displacement.  $G_{np}(\underline{x}; \underline{x}')$  is a Green's function giving the  $n$ -component of displacement at  $\underline{x}$  resulting from a point force in the  $p$ -direction at  $\underline{x}'$ ,  $c_{ijpq}$  is the elasticity tensor, and  $H[i]$  is a function that takes a value of 0 or 1 depending on whether the point  $\underline{x}$  lies outside or inside the volume of interest,  $i$ , respectively. We assume that the media are homogeneous and isotropic, so the constitutive relation can be written with the aid of the elasticity tensor as

$$\tau_{ij}(\underline{x}) = \lambda \Theta(\underline{x}) \delta_{ij} + \mu [u_{i,j}(\underline{x}) + u_{j,i}(\underline{x})], \quad (10)$$

where  $\Theta(\underline{x}) = u_{k,k}(\underline{x})$  is the dilatational parameter and  $\lambda$  and  $\mu$  are Lamé parameters for the medium.

In this work the upper medium is acoustic, supporting propagation of only dilatational waves while the lower medium is taken as elastic. The boundary separating these two media is shown in Figure 2. The boundary conditions for the resulting acoustic-elastic boundary, can be written in the general form

$$\begin{aligned} \mathbf{n} \cdot \underline{u}^{(f)}(\underline{x})_{x_3=\zeta(x_1)} &= \mathbf{n} \cdot \underline{u}^{(s)}(\underline{x})_{x_3=\zeta(x_1)}, \\ \mathbf{T}^{(f)}(\underline{x})_{x_3=\zeta(x_1)} &= \mathbf{T}^{(s)}(\underline{x})_{x_3=\zeta(x_1)}, \\ \mathbf{n} \times \mathbf{T}^{(s)}(\underline{x})_{x_3=\zeta(x_1)} &= 0, \end{aligned} \quad (11)$$

where the surface profile function is taken to be  $x_3 = \zeta(x_1)$  and the unit normal vector along the interface can be expressed as

$$\hat{n} = (-\zeta'(x_1), 1)[1 + (\zeta'(x_1))^2]^{-\frac{1}{2}}. \quad (12)$$

The first boundary condition represents the continuity of normal displacement and the latter two conditions together represent the continuity of normal stress. Referring to the requirement for continuity of normal displacement one can expand the first term of the volume integral (9) as

$$n_i c_{ijpq}^{(f)} u_i^{(f)}(\underline{x}) = \lambda^{(f)} n_i u_i^{(f)}(\underline{x}) \delta_{pq}, \quad (13)$$

which follows from the lack of rigidity in the acoustic medium,  $\mu^{(f)} = 0$ . The last two boundary conditions in (11) infer the continuity of fluid pressure at the interface. Upon combining these two boundary conditions with the constitutive relation, (10), the traction in the solid can be expressed at the interface as

$$T_p^{(s)}(\underline{x}) = S^{(f)}(\underline{x}) n_p = \lambda^{(f)} \theta^{(f)} n_p, \quad (14)$$

where  $S^{(f)}(\underline{x})$  is the fluid pressure in the fluid. Finally, referring to eq. (13) and comparing it with a similar expansion in the elastic medium it is clear that the equality  $u_i^{(s)}(\underline{x}) = U_i(\underline{x}) = u_i^{(f)}(\underline{x})$  implies that the normal displacement is continuous, or  $n_k u_k^{(s)}(\underline{x}) = n_k u_k^{(f)}(\underline{x}) = n_k U_k(\underline{x})$ .

Taking our volume of interest to be the upper acoustic medium, placing the incident wave in the acoustic medium, and substituting the final form of the boundary conditions (11), the

integral equation in the lower elastic medium can be written as

$$0 = \int_{\infty}^{\infty} dx'_1 [U_i(\underline{x}') c_{ijpq}^{(s)} n_j \frac{\partial G_{np}^{(s)}(\underline{x}; \underline{x}')}{\partial x'_q} - G_{np}^{(s)}(\underline{x}; \underline{x}') S^{(f)}(\underline{x}') n_p], \quad (15)$$

where the unknowns are the fluid pressure,  $S^{(f)}(\underline{x})$ , and the displacement,  $U(\underline{x})$ , along the interface.  $S^{(f)}(\underline{x})$  should not be confused with the surface function referred to previously.

In the acoustic medium, the surface integral can be greatly simplified. Since shear waves can not propagate in the acoustic medium, one of the two integral equations (9) in the upper medium is redundant and can be combined into one equation. We note that the fluid pressure in the acoustic medium,  $S^{(f)}(\underline{x})$ , satisfies the basic wave equation

$$\nabla^2 S^{(f)}(\underline{x}) + (k_t^f)^2 S^{(f)}(\underline{x}) = 0, \quad (16)$$

assuming no sources are present in the medium. The Helmholtz potential for the displacement,  $\phi^{(f)}(\underline{x})$ , also satisfies a similar wave equation. Transforming to the frequency domain and differentiating we find that  $\phi^{(f)}(\underline{x})$  is directly related to the P wave pressure,

$$\phi^{(f)}(\underline{x}) = -(\rho^{(f)} \omega^2)^{-1} S^{(f)}(\underline{x}), \quad (17)$$

Using this relation, the normal displacement at the interface can be expressed as

$$\frac{\partial S^{(f)}(\underline{x})}{\partial n} = -\rho^{(f)} \omega^2 (n_k u_k^{(f)}(\underline{x})) = -\lambda k_T^{(f)2} (n_k u_k^{(f)}(\underline{x})) \quad (18)$$

and using the Green's function for the pressure,  $G^{(f)}(\underline{x}; \underline{x}')$ , the integral equation in the acoustic medium can be expressed with the aid of Green's second integral theorem as

$$S^{(f)}(\underline{x}) = S^{(f)}(\underline{x})_{\text{incid}} \quad (19)$$

$$+ \int_{-\infty}^{+\infty} dx'_1 [\lambda^{(f)} S^{(f)}(\underline{x}') \frac{\partial G^{(f)}(\underline{x}; \underline{x}')}{\partial n} + \lambda^{(f)2} k_T^{(f)2} G^{(f)}(\underline{x}; \underline{x}') n_k u_k^{(f)}(\underline{x}')],$$

where we have utilized (18). Equations (15) and (19) together consist of three integral equations with three unknown functions. These integral equations now express the total scattered field in both media. Letting  $x_3 \rightarrow \zeta^+(x_1)$ , the final set of coupled integral equations can be written as,

$$\begin{aligned} S(\underline{x}) &= S^{(f)}(\underline{x})_{\text{incid}} & (20) \\ &+ \int_{-\infty}^{+\infty} dx'_1 [S(\underline{x}') T^{(f)}(\underline{x}|\underline{x}') - D_n^{(f)}(\underline{x}|\underline{x}') D_n(\underline{x}')], \end{aligned}$$

in the acoustic medium, and

$$0 = - \int_{-\infty}^{+\infty} dx'_1 [U_i(\underline{x}') T_i^{n(s)}(\underline{x}|\underline{x}') - \frac{\lambda^{(f)}}{\mu^{(s)}} D_n^{(s)}(\underline{x}|\underline{x}') S(\underline{x}')], \quad (21)$$

in the elastic medium. We have defined

$$T^{(f)}(\underline{x}|\underline{x}') = \lambda^{(f)} \frac{\partial G^{(f)}(\underline{x}; \underline{x}')}{\partial n} \Big|_{x_3=\zeta(x_1)}, \quad (22)$$

$$D_i^{(f)}(\underline{x}|\underline{x}') = -\lambda^{(f)} k_T^{(f)2} G^{(f)}(\underline{x}; \underline{x}') n_i \Big|_{x_3=\zeta(x_1)}, \quad (23)$$

$$T_i^{n(s)}(\underline{x}|\underline{x}') = T_i^{n(s)}(\underline{x}|\underline{x}') \Big|_{x_3=\zeta(x_1)},$$

$$D_n^{(s)}(\underline{x}|\underline{x}') = \mu^{(s)} G_{np}^{(s)}(\underline{x}; \underline{x}') n_p \Big|_{x_3=\zeta(x_1)}.$$

in the respective media. Now the unknown source strength functions, which we eventually solve for, can be expressed as a function of  $x_1$  alone

$$S(x_1) = \theta^{(f)}(\underline{x}) \Big|_{x_3=\zeta(x_1)}, \quad (24)$$

$$D_i(x_1) = U_i^{(f)}(\underline{x}) \Big|_{x_3=\zeta(x_1)},$$

where we have normalized the pressure term with respect to  $\lambda^{(f)}$  to ensure that the final numerical conditions are well conditioned.

The scattered field in the acoustic medium can now be expressed completely in terms of the unknown source functions, (24). The cartesian coordinate form of the Green's function in the fluid can be written as

$$G^{(f)}(\underline{x}; \underline{x}') = \frac{i}{4\pi\lambda^{(f)}} \int_{-\infty}^{+\infty} dk \frac{e^{ik(x_1 - x'_1) + ik_3^{(f)}|x_3 - x'_3|}}{k_3^{(f)}}, \quad (25)$$

where

$$k_3^{(f)} = ((k_T^{(f)})^2 - k^2)^{\frac{1}{2}}, \quad Im(k_3^{(f)}) > 0,$$

which corresponds to a pressure source,  $P(\underline{x}) = -\lambda^{(f)-1}\delta(x_1 - x'_1)\delta(x_3 - x'_3)$  applied at  $\underline{x}'$  in the fluid. Substituting (25) into the surface integral (19) the scattered field at any point  $x_3 > \zeta(x_1)_{max}$  in the fluid can be decomposed into a summation of plane waves

$$S(\underline{x})_{scat} = + \int_{-\infty}^{+\infty} \frac{dk}{2\pi k_3^{(f)}} R_f(k\omega) e^{ikx_1 + ik_3 x_3}, \quad (26)$$

where the amplitude coefficient takes the form

$$\begin{aligned} R_f(k\omega) = & \frac{i}{2} \int_{-\infty}^{+\infty} dx'_1 [iS(\underline{x}')(k\zeta'(\underline{x}') - k_3^{(f)}) \\ & - k_T^{(f)2}(\zeta'(x'_1)D_1(\underline{x}') - D_3(\underline{x}'))] e^{-ikx'_1 - ik_3^{(f)}\zeta'(x'_1)}. \end{aligned} \quad (27)$$

To reduce the computational demand of this approach, the incident wave is expressed as a narrow Gaussian beam source following Maradudin (1990). This allows for a reduction

in the length of integration along the acoustic boundary, since only a small portion of the interface is excited by the incident beam. The pressure of a Gaussian beam incident at an angle,  $\theta_0$ , in the acoustic medium can be written as

$$S^{(f)}(\underline{x})_{inc} = e^{ik_T^{(f)}(x_1 \sin \theta_0 - x_3 \cos \theta_0)[1 + W(\underline{x})]} e^{-((x_1 \cos \theta_0 + x_3 \sin \theta_0)/w)^2}, \quad (28)$$

where

$$W(\underline{x}) = \frac{1}{k_T^{(f)2} w^2} \left[ \frac{2}{w^2} (x_1 \cos \theta_0 + x_3 \sin \theta_0)^2 - 1 \right], \quad (29)$$

which is an approximation to the wave equation, (16), and is valid so long as  $\frac{\omega w}{2c} \gg 1$ , where  $w$  is the half-width of the Gaussian beam. We also express  $w = h \cos \theta_0$ , where  $h$  is the half-width of the incident beam as seen on the plane  $x_3 = 0$ .

An approximation to the Fourier reflection coefficient can now be written in terms of the amplitude coefficient, (27). Normalizing this amplitude coefficient by the amplitude of the incident plane wave having a wave vector corresponding to the angle of incidence, the reflection coefficient can be expressed as

$$R(k\omega) = \frac{|r_p(\theta_s)|}{2\sqrt{\pi} k_T^{(f)} w}, \quad (30)$$

where

$$\begin{aligned} r_p(\theta_s) = & \int_{+\infty}^{-\infty} dx'_1 [iS(x'_1) k_T^{(f)} (\sin \theta_s \zeta(x'_1) - \cos \theta_s) \\ & - k_T^{(f)2} (\zeta'(x'_1) D_1(x'_1) - D_3(x'_1))] e^{-ik_T^{(f)} (\sin \theta_s x'_1 + \cos \theta_s \zeta'(x'_1))}, \end{aligned} \quad (31)$$

which is comparable in amplitude to the Fourier reflection coefficient calculated for a single

incident plane wave, and we let  $k = k_T^{(f)} \sin \theta_s$ , and  $k = k_T^{(f)} \cos \theta_s$ . Note that this normalization is different from the Differential Reflection Coefficient of Schultz and Toksöz (1993a,b).

Appendix A describes how these integral equations can be solved numerically following the approach of Schultz and Toksöz (1993a,b). We show that the solution to this acoustic-elastic case can be expressed completely as a combination of the Green's functions for the P-SV and SH case, where the shear velocity of the SH wave is changed to the P-wave velocity of the acoustic medium, so as to reflect the acoustic Green's function. The final coupled integral equations are then transformed to a coupled set of matrix equations and solved using LU decomposition.

### Numerical Analysis

In this paper two types of interfaces are modeled numerically. Both interfaces have a Gaussian distribution about the mean, where  $\delta^2 = \langle \zeta^2(x_1) \rangle$  is the mean-square departure of the surface from flatness. The first interface studied has a correlation function

$$W(|x_1 - x'_1|) = \delta^{-2} \langle \zeta(x_1) \zeta(x'_1) \rangle, \quad (32)$$

described by a Gaussian correlation function,  $W(|x_1|) = \exp(-x_1^2/a^2)$ . The correlation length for a Gaussian interface is approximately equal to the average distance between adjacent peaks and valleys along the interface. The interface can also be described in terms of the *rms* slope of surface,  $\phi$ , which we will refer to often. This *rms* slope can be written as  $\phi = \tan^{-1}(\frac{\sqrt{2}\delta}{a})$ . The second surface studied has an exponential correlation function,

$$W(|x_1|) = \exp(-x_1/a).$$

Averaging over an ensemble of realizations of these surfaces, we display the final scattered pressure as a statistical average that follows the approach of Schultz and Toksöz (1993a,b). The statistical characteristics of the scattered pressure can then be analyzed for possible scattering mechanisms. Although the coherent and incoherent properties of the scattered field were computed for seismic analysis, only the total mean squared contribution to the Reflection Coefficient (RC) is presented in the following sections. The total mean squared contribution to the RC can be written as

$$\left\langle \frac{\partial R_p}{\partial \theta_s} \right\rangle_{tot} = \frac{4\pi}{k_T^{(f)2} w^2} \langle |r_p(\theta_s)|^2 \rangle. \quad (33)$$

This gives the average squared pressure reflected into the upper medium as a function of the scattering angle,  $\theta_s$ , given one incident beam angle,  $\theta_0$ . The square root of this RC is used for comparison with experimentally recorded amplitudes.

## Experimental Procedure

The experimental procedure involved submerging a solid elastic model, in this case a glass block, into an experimental water tank, essentially creating an acoustic-elastic interface at the boundary between the block and the surrounding water. The first portion of the experiment entailed generating a characterized random surface that, if successful, would have predetermined Gaussian statistics. The second portion involved constructing a motor driven measurement device that could accurately (to within a fraction of a degree) measure

various realizations of the fluid-glass boundary.

### Random Interface Generation

Fabricating the randomly irregular scattering surface was the most challenging part of this project. Numerous irregular surfaces were designed. Models ranged from irregular distributions of glass beads to roughened cement surfaces. In addition, random distributions of gravel held together by epoxy were tested along with naturally rough granite and sandstone surfaces. Unfortunately, these models either did not give proper control over statistical parameters or were extremely heterogeneous at the ultrasonic level, making comparisons with numerical models very difficult. After much experimentation the most promising approach became the fabrication of a random glass surface using an etching procedure.

The irregular glass surface was designed using a solid glass block and a standard etching process. First the cylindrical glass block shown in Figure 3 was cast using a graphite mold. After one week of annealing the block had a final diameter of 19.5 cm and a height of 7.5 cm. The upper surface, that was exposed to air, contracted slightly due to the high expansion coefficient of Na glass and resulted in a slightly concave surface. Therefore, the lower plane surface of the block was etched.

The general theory behind etching a specific surface is shown in Figure 4. Take, for instance, the fabrication of the valley shown in the upper left portion of the figure. In this case, the valley is divided into a number of discrete depth intervals. Photoresist templates

are designed to match the geometry of the valley at each discrete depth. The first template is glued to the smooth glass surface that, in the case of a valley, contains only a small gap. The surface is then exposed to a constant pressure of high velocity particles which chip any portion of the surface not covered by photoresist. After a set time which depends on the compressed air pressure and the sand/air mixture ratio, the exposed glass is etched to a target depth. The first layer of photoresist is then removed, and the next layer is attached exposing a larger portion of the surface to the incoming sand particles. The glass surface is exposed again to sand particles for the same amount of time. The valley is now broader and twice as deep. Adding each template in a similar manner, the desired valley is etched into the glass surface.

To achieve the desired random interface, the Gaussian surface described in the previous section was first numerically generated. Both the transverse correlation length,  $a$ , and the standard deviation of the height,  $\delta$ , of the interface were specified as 1 mm and .71 mm, respectively, giving an *rms* slope of 45°. After generation, the Gaussian surface was discretized into six individual depth levels, with each level's thickness equal to one standard deviation of the surface. The templates shown in Figure 5 were successively glued to the surface and each template was exposed to high velocity sand particles normally incident on the surface for approximately 360 s. A simple lateral sweeping motion of the sand blaster was used to cover the whole template. The blaster operated at a pressure of 125 kPa ( $\approx$  18 psi) with the glass surface 0.3 m from the nozzle of the sand blaster. In general, the

correlation length of the surface was controlled by the template design, and the standard deviation of the interface was controlled by the time that each template was exposed to the sand blast.

As the etching proceeded, we found that the standard deviation and correlation length were difficult to control precisely. We observed during the sand blasting process that particles impacting the surface tended to scatter many times within valleys, generally broadening the valley width. In addition, small narrow peaks tended to chip away far faster once completely exposed to the sand blast, removing the linearity assumed in the design of the surface. As we show below, this results in a longer correlation length than expected. In this study, the target 'rms' slope of the interface was  $45^\circ$  and the desired correlation length was 1 mm.

### **The Scattering Instrumentation**

Once the irregular glass surface was created, an automated scattering apparatus was used to measure the scattering properties of the interface. The two different flat-bottomed transducers used to create a beam source were a Panametrics 12.7 mm diameter transducer (1.5 MHz,  $\lambda = 1.0$  mm in water) and a Panametrics 25.4 mm diameter transducer (0.5 MHz,  $\lambda = 3.0$  mm in water). The detectors, which were also Panametrics flat-bottomed transducers, consisted of a 6.4 mm diameter transducer (1.5 MHz,  $\lambda = 1.0$  mm in water) and a 12.7 mm diameter transducer (0.5 MHz,  $\lambda = 3.0$  mm in water), respectively. The detectors were chosen such that they were sensitive only to waves approaching nearly perpendicular

to the surface of the transducer, limiting the energy recorded to waves which approach in line with the transducer axis. Given the source parameters, the resulting source radiation pattern was a beam of energy with the majority of the source energy travelling in the forward direction. As shown in Figure 6 the source radiation patterns show some spreading of the beam although further tests showed that this slight spreading did not significantly affect the results.

Experimental data was recorded in our in-house water tank, described in Appendix B. The experimental geometry used to measure the surface scattering is shown in Figure 7. The glass block was located at the center of the experiment and the source and detector were then stepped in a semicircle about an axis of rotation running parallel to the general trend of the irregular fluid-glass interface. In each experiment the source was placed at a constant incident angle,  $\theta_0$ , and a constant .35 m distance from the axis of rotation. The recording angle was then controlled by mounting the detector on a motor-driven, rotating arm that held the detector .30 m from the given axis of rotation. The arm was then rotated in 0.9° steps about this axis of rotation. Therefore, the recorded energy represents scattering in the plane of incidence. As a result, it is important to note that the detector occludes the source when it is near the backscattering position. This results in a loss of 3° to 6° of scattering amplitudes centered about the source position. These data points are not plotted.

The final desired measurement is the mean scattered pressure as a function of scattering angle, given a fixed angle of incidence. Since the scattering mechanisms working at the

interface are strongly a function of frequency, we are interested in measuring the scattered field at specific frequencies. Two different approaches to this problem can be taken. One is to record the scattered energy given a broad band incident wavelet and then to decompose the recorded energy as function of frequency. However, since it is unclear exactly what numerical effects may be introduced with the narrow band filtering we take the second approach which involves no filtering and gives cleaner results. We introduce directly via the transducer source a monochromatic wave of given frequency. The continuous sinusoidal wave is approximated well by a finite sinusoid ranging from 35 to 100 cycles. The final constant amplitude of the scattered pressure is then recorded.

A single realization of scattering from the irregular interface results in large fluctuations in scattered pressure as a function of the scattering angle. It is necessary, therefore, to average experimentally as we averaged numerically, so as to obtain a final mean reflection coefficient. In optical theory, averaging is accomplished by illuminating a field lens that is much larger than these fluctuations. The fluctuations, referred to as speckle in optical terminology (O'Donnell and Mendez, 1987), are integrated over a specified solid angle giving the average intensity scattered at that angle. In seismic experiments it is very difficult to use an integrating lens. This difficulty arises mainly from the limited size and frequency range of ultrasonic experimentation. As a result, we chose to follow the numerical approach and to create different independent realizations of the interface. The pressure of waves scattered from an ensemble of interface realizations was averaged to determine the final mean scattered

pressure at each scattering angle. The computer-controlled arm allowed for rapid acquisition of data with the reproducibility required for this averaging scheme. A typical measurement consisted of measuring the scattered pressure from an independent statistical realization of the interface. Each independent realization was acquired by rotating and shifting the sample in the sequence shown in Figure 8. Since rotating the surface with respect to the incident beam formed another scattering geometry, many different realizations of the interface were obtained. In general, the sample was rotated by 60° staggered steps, followed by 1.25 cm shifts of the block, which placed the axis of rotation for the source and receiver on concentric circles about the center of the glass cylinder. This movement sequence can easily give more than 150 different realizations of the interface.

Due to interest in the enhancement of energy travelling directly back towards the source, it was desirable to create a source-receiver design that retrieved energy in the occluded zone near the source. This was achieved by constructing a four-layered piezo-film detector. The general idea behind the piezo-film receiver is straightforward. A single layer of film has an impedance very similar to water, and, as a result, when the piezo-film is placed directly in front of the source, the source energy transmits almost completely through the detector, allowing most of the energy to travel towards the interface. The incident wave is then diffracted from the interface, and the scattered energy travelling directly back towards the source is recorded as it transmits a second time through the piezo-film receiver. A four-layer piezo-film receiver was constructed using conducting glue and in-parallel connections,

significantly increasing the signal to noise ratio. The construction of this receiver is discussed in detail in Appendix B. It is important to note that the piezo-film receiver is sensitive to energy arriving both from in front and from behind the receiver. As a result, extreme care was taken to choose a time window of analysis that did not contain multiple scattering from the source and the tank wall. In addition, as we will show, piezo-film of this thickness does have a substantial reflection coefficient, therefore, a resonance between source and receiver had to be avoided, too.

We stress that the data discussed in the next section represents the mean diffusely scattered signal, as a function of angle, for a fixed solid angle of data acquisition. No artificial angular factors are introduced to the data even though the apparent vertical wavelength, acting at the surface in this experiment, varies inversely with the cosine of the scattering angle. We do not place any absolute vertical scales on the data, although for comparison the data are normalized to the numerical RC calculated at normal incidence.

## Surface Scattering Measurements

In this section we present the average reflection coefficient measurements obtained using the roughest glass surface fabricated. This surface was chosen because many scattering mechanisms will play their strongest role. Figure 9a shows the target surface height distribution, independent of lateral position, and Figure 9b shows the histogram of the surface height, based on surface profilometer measurements of the actual surface. The histogram shows

that the data nicely matches a Gaussian probability distribution with a standard deviation of approximately 0.6 mm. This is close to the target value,  $\delta = 0.71$ . Figure 10a gives the target Gaussian autocorrelation function, and Figure 10b shows the actual autocorrelation function calculated from profilometer measurements. As previously predicted, the correlation length of 1.4 mm is greater than the target value of 1 mm. Also plotted are Gaussian and exponential autocorrelation functions with the same correlation length as the data. The autocorrelation function is very close to a Gaussian correlation function at the more important, smaller lags. At larger lag distances, the surface lies directly in between a Gaussian and an exponential correlation function.

Figure 11a gives a 3-D grayscale plot of the irregular surface based on the surface profilometer measurements. Figure 11b plots the surface height for a profile taken across the surface, while Figure 11c shows a numerically generated Gaussian and exponential surface given the same standard deviation and correlation length. It is clear that the Gaussian surface matches the experimental interface well, both in the observed slopes and the lateral scale of the irregularities. Since the frequency domain representation of the surface goes as the square root of its correlation function, the exponential surface should contain larger amounts of energy at both low and high frequencies. This is seen clearly since the exponential surface contains lower amplitude short wavelength irregularities that were not observed on the experimental surface. Although the Gaussian gives a good fit to the experimental data, out of interest, we shall still plot the results for an exponential surface.

Based on the measurements above, the final glass interface slopes steeply at approximately  $30^\circ$  *rms*, and the impedance contrast at the fluid-glass interface is large as the glass interface has properties very similar to an igneous material (see Figure 3). As a result, multiple-scattering and shadowing effects can play a significant role at both small and large incident angles, and approximate linear theories, such as the Kirchhoff and Born approaches, break down. Therefore, the mean scattered pressure measured experimentally is compared with the reflection coefficients calculated with the Boundary Integral technique, formulated earlier. This technique includes all multiple scattering and wave conversions at the interface.

**Case:**  $\lambda = 0.71a$

Figure 12 shows one realization of the interface given an incident pulse with a center frequency of 1.5 MHz and a half-power width of 0.25MHz. This realization corresponds to a beam impinging on the surface with an incident angle of  $20^\circ$ . The source pulse is shown. This pulse is also shown reflected from a plane interface, in which case energy arrives only in the specular direction. Referring to the polar seismogram, it is clear that the large scale surface roughness scatters energy over most forward and back scattering angles. The energy is spread over a large time interval and amplitudes vary rapidly as a function of scattering angle. In general, it is difficult, given this single model, to determine quantitatively which scattering mechanisms are working at the surface.

Our first continuous wave analysis is carried out at 1.5 MHz, the center frequency of

the seismogram above, so that  $\lambda = .71a = 1.00$  mm. Figure 19 shows one experimental realization of the fluid-glass surface at each of four incident beam angles:  $0^\circ$ ,  $20^\circ$ ,  $30^\circ$ , and  $60^\circ$ . Clearly the amplitudes in each realization vary strongly as a function of scattering angle,  $\theta_s$ . As discussed earlier, these fluctuations can be removed by averaging over a finite number of realizations and obtaining a mean reflection coefficient. The total mean reflection coefficients for both a Gaussian and an exponential surface are given in Figures 14-17 and Figures 20-23. At the bottom of these figures, the experimental mean reflection coefficients are given along with the SD of the finite average, showing the deviation of these reflection coefficients from the final mean reflection coefficient corresponding to a full ensemble of realizations. Negative scattering angles ( $\theta_s < 0$ ) correspond to backscattering in all plots. We also stress that given the incident wavelength, the surface is extremely irregular and the specular reflection is largely disrupted.

Figure 14 shows the total mean scattered pressure as a function of scattering angle given a normally incident acoustic beam. Upon comparing the numerical and experimental data it is clear that the 2-D numerical results for a Gaussian interface match the 3-D scattered data extremely well. The fluctuations in the data are mostly within one standard deviation of the finite average. There are a number of interesting aspects in the curves. The experimental data shows a strong peak amplitude propagating back towards the source at  $\theta_s = 0^\circ$ ; this is predicted well by the numerical reflection coefficient. The width of this peak is approximately  $35^\circ$ . Notice that there is considerable scattering at all angles, dropping off linearly

with increasing scattering angle. The exponential surface also predicts the general form of scattering well, but the higher frequency component appears to destroy the enhancement of energy scattered back towards the source.

A similar form of scattering is exhibited in Figures 15 and 16, which show the mean scattered pressure for an incident angle of  $20^\circ$  and  $30^\circ$ , respectively. Both the numerical results for the Gaussian interface and the experimental data match very well. There are also two remarkable aspects to these curves. First, on both reflection coefficients two peaks can be identified by eye. One is a broad peak occurring in the forward scattered direction. The other is much narrower and occurs in the retroreflective direction  $\theta_s = -\theta_0$ . This "retroreflective" peak loses amplitude as the incident angle is increased, sinking further into the surrounding reflection coefficient curve. This retroreflectance is clearly supported by the ultrasonic data. Second, both curves become strongly asymmetric. However, upon comparing the curves, the 2-D numerical model shows more backscattering and less forward scattering than the 3-D ultrasonic data. This trend becomes more prominent as the incident angle is increased. The exponential curve also follows the experimental reflection coefficient closely, showing again a less distinct retroreflective peak.

Figure 17 gives the mean scattered pressure for a beam incident at  $60^\circ$ . In this case there are no distinct signs of enhanced backscattering in either the numerical or the experimental data. However, energy is scattered uniformly over most backscattering angles. This energy does not drop off until the retroreflective angle is exceeded in the backscattering region.

Most dramatic is the continuation of the trend observed at the smaller incident angles above. Specifically, the numerical data clearly shows more backscattering and less forward scattering than the experimental data.

**Case:  $\lambda = 2.14a$**

Figure 18 shows one realization of the interface given an incident pulse with a center frequency of 0.5 MHz and a half-power width of 250 kHz. This realization corresponds to a beam impinging on the surface at a 20° incident angle. The pulse reflected from a plane interface is shown, with the energy again arriving only in the specular direction. Referring to the scattered seismogram, it is clear that, even at this lower frequency, energy is scattered over most forward and backscattered angles. Given this one deterministic case, it is difficult to determine quantitatively the scattering mechanisms operating at this frequency, or to define how they might differ from those in the higher frequency case.

This second continuous wave analysis was carried out at 0.5 MHz, the center frequency of the seismogram above, so that  $\lambda = 2.14a = 3.0$  mm. Figure 13 shows one experimental realization of the fluid-glass surface at each of the four incident beam angles. Once again the amplitudes for each realization vary strongly as a function of scattering angle, although not as strongly as the  $\lambda = .71a$  case. Figure 20 shows the comparison between the averaged numerical and experimental reflection coefficients given a normally incident beam. The 2-D numerical results for a Gaussian interface predict the experimental observations well. All of

the experimental data sits within the standard deviation of the finite-average. Comparing these curves to the curves for  $\lambda = 0.71a$ , a number of distinct differences are apparent. Most noticeable is the widening of the retroreflective peak width from about  $35^\circ$  to greater than  $60^\circ$ . This widening is apparent in both the experimental and the numerical data. The reflection coefficient for an exponential interface again shows much lower retroreflectance than for the Gaussian interface.

Figures 21 and 22 both show that the numerical results over a Gaussian interface predict the asymmetric trends in the experimental data very well for incident angles of  $20^\circ$  and  $30^\circ$ , respectively. However, distinct differences do occur between the two curves. First, as the incident angle increases, the 2-D numerical results again show more backscattering and less forward scattering than the 3-D ultrasonic data. A broad retroreflective peak is both predicted and observed at  $20^\circ$  and  $30^\circ$  incidence, supporting the existence of retroreflectance. Unfortunately, the height of these peaks are of the same order as the standard deviation of the experimental average, not allowing for a direct verification of retroreflectance. Numerically, the exponential interface does give rise to a retroreflective peak; this peak is smaller than the peak predicted by the Gaussian surface.

Figure 23 shows the mean reflection coefficient for an incident angle of  $60^\circ$ . In this case enhanced backscattering is not predicted numerically or observed experimentally. At this lower frequency, the 2-D numerical model predicts more backscattering and less forward scattering than the 3-D ultrasonic data. In addition, the numerical model predicts a much

smaller specular peak than is observed experimentally. Although the amplitudes are different, the numerical curves do predict well the uniform scattering of energy into the fluid above as shown in the data.

Retroreflectance is clearly supported by the ultrasonic data above. However, the retroreflective peak height is still on the same order as the standard deviation of the finite-average in each case. This makes it difficult to verify the existence of "enhanced backscattering." For this reason, data was recorded near the retroreflective direction using the partially transparent piezo-film receiver. The experimental procedure is described in Appendix B, the steps obtaining the final reflection coefficient are summarized in Figure 24, and the final average RC observed with the piezo-film receiver is superposed on Figure 21. The data has been scaled to the amplitudes received with the flat-bottomed transducers. The scattered pressure was measured between the backscattering angles of  $40^\circ$  and  $5^\circ$  ( $-40^\circ < \theta_s < -5^\circ$ ), and 65 surface realizations were averaged. In this case, the size of the retroreflective peak is larger than the corresponding SD of the average. The 2-D numerical model predicts the 3-D experimental data very well, to within the standard deviation of the finite average. A distinct peak is observed in the retroreflective direction with a slightly narrower form than the numerically generated peak. This result strongly supports the enhancement of backscattered energy due to multiple scattering from the glass interface.

## General Discussion

Generally, the numerically derived mean reflection coefficients calculated over an acoustic-elastic interface show retroreflective trends similar to those observed for the SH and P-SV cases. First, the width that the retroreflective peak appears to be is consistent with the multiple scattered constructive phase argument summarized in the introduction. In this case, when the wavelength is increased by a factor of three, both the numerically derived curve and the experimental data show a factor of three increase in peak width, from  $35^\circ$  at  $\lambda = .71a$  to greater than  $60^\circ$  at  $\lambda = 2.14a$ . Second, as the incident angle is increased, the retroreflective peak amplitude tends to decrease relative to the remaining portion of the DRC. The retroreflective peak in both the experimentally and numerically derived curves seems to disappear around an incident angle equal to the  $30^\circ$  *rms* slope of the interface. Although not studied directly here it seems likely, based on the work of Schultz (1993a), that the retroreflective peak height will tend to decrease as the impedance contrast is lowered and more energy is allowed to penetrate the interface. Along the same lines, the retroreflective peak amplitude is likely to diminish as the *rms* slope of the interface is decreased, since not as many time-reversed paths can be obtained with lower slopes.

Interestingly, as the incident angle was increased, the numerical results above consistently predicted “more backscattering and less forward scattering” than observed in the 3-D experimental results. We stress that the amplitudes for the 2-D and 3-D are normalized to each other at normal incidence, so that the absolute amplitude of backscattering is not given. The

above statement, "more backscattering and less forward scattering," means that backscattering decreases and forward scattered amplitudes increase more slowly in the 2-D case than in the 3-D case as the incident angle is increased. Two explanations may clarify this deviation. First, the glass interface used in the experiment may not follow Gaussian statistics exactly. Therefore, the observed differences may be a direct result of differences in the statistics of the model. However, the interface statistics were well-constrained using surface profilometer measurements. A second possible explanation, is that there may be distinct differences in the scattering due to an inherent difference between 2-D and 3-D scattering mechanisms. In the case of 2-D scattering, a peak along the interface is actually an infinite ridge extending in the  $x_2$ -direction. A wave incident on the side of this ridge has only three probable routes of getting to the receiver located on the opposite side of the ridge. The wave can either multiply scatter within the valley, transmit through the ridge, or diffract over the very peak of the ridge. Each of these paths exists, but a wave loses a large amount of energy along any of these paths. In the 3-D case, the surface has one more degree of freedom so that a peak along the interface can vary in all directions. Therefore, at normal incidence, out of plane scattering allows energy to arrive randomly from all directions and may increase the amount of observed backscattering. As the incident angle is increased, energy travels also out of the incident plane. However, unlike the 2-D interface, the 3-D nature of the interface may allow energy to pass around obstructing peaks, reducing the amount of backscattered energy in the measure that the incident angle is increased. For instance, energy may diffract from the

flank of a nearby peak and propagate in the forward direction back into the receiver plane. In this case, out-of-plane scattering would work to reduce the amount of backscattering, and additional energy may be allowed to propagate as forward scattered energy, explaining the difference between the 2-D and 3-D trends.

## Conclusions

In this study, we were able to generate within reasonable accuracy a 3-D characterized random interface with Gaussian statistics. An interface with approximately a Gaussian surface height distribution and Gaussian correlation function was generated using a glass etching procedure and photoresist templates. The resulting surface distribution was confirmed using surface profilometer measurements. Scattered pressures were then acquired over this surface and compared directly to numerical results calculated over a 2-D interface with the same statistical parameters.

Specifically, we have shown that 2-D numerical models of an acoustic-elastic interface with Gaussian statistics predict the 3-D scattering that is observed experimentally very well, when the incident wave is near normal incidence. Numerical results predict the large amount of observed incoherent backscattering and forward scattering. Numerical results also predict the elimination of the specular reflection at many incident angles. Most striking is the prediction of a "retroreflective" amplitude peak. The numerical results predict that the peak amplitude decreases as the incident angle increases and the peak's width is directly

proportional to the ratio of the incident wavelength and the correlation length of the interface. Experimentally, enhanced backscattering is strongly supported by observations at normal incidence and at 20°-incidence. The peak's amplitude appears to decrease dramatically when the incident angle becomes greater than the *rms* slope of the interface. Numerical modeling of an exponential surface with the same correlation length and standard deviation as the glass interface gives results very similar to the results of the Gaussian surface although the results show more general backscattering. Retroreflectance from the exponential interface was difficult to identify in almost all cases studied.

The 2-D numerical curves deviate from the experimental curves at incident angles greater than 30°. Specifically, as the incident angle is increased, the 2-D models predict more backscattering and less forward scattering than observed in the experimental data. This trend becomes much stronger as the incident angle approaches grazing angles. As the surface in this experiment is well characterized, this appears to result from a distinct difference between 2-D and 3-D scattering mechanisms. In this case the peaks and valleys of 3-D surfaces appear to backscatter less energy into the plane of incidence than the ridges along 2-D interfaces when the incident angle is increased. In addition, they allow more energy to scatter forward into the plane of incidence. Even though the amplitudes did not match at larger incident angles, the trends of the reflections coefficients did match. Both numerical and experimental results showed energy scattered uniformly over most scattering angles as a 60° incident angle was approached. This results in negative phase velocities, large phase

velocities, and a large amount of interference in seismic data recorded in the fluid above the interface.

Although tests were not carried out on epoxy surfaces in this study, an epoxy surface was generated for the purpose of profilometer measurements. Essentially, the irregular glass surface was used as a mold. After adding a separating solution, an epoxy model was generated and separated from the glass mold. We have concluded that the glass surface can be used to make models out of different substances, each with different material properties. Future work will therefore include studies to determine how the material properties affect scattering from surfaces with identical height distributions. Although in this paper we chose to fabricate a Gaussian surface, the etching process used here can also be used to create an interface with exponential statistics.

## References

Abramowitz, M. & Stegun, I.A., 1964. *Handbook of Mathematical Functions*, Dover Publications, New York, NY (sections 9.1.3, 9.1.10–11, 9.1.27, 9.1.30, 9.4.1–6).

Dacol, D.K. and Berman, D.H., 1988, Sound scattering from a randomly rough fluid-solid interface, *J. Opt. Soc. Am.*, *84*, 292–302.

Frankel, A., & Clayton, R., 1986, Finite difference simulations of seismic scattering: implications for the propagation of short-period seismic waves in the crust and models of crustal heterogeneity, *Jour. Geophys. Res.*, *91*, 6465–6489.

Haddon, R.A.W., 1978, Scattering of seismic body waves by small random inhomogeneities in the earth, *NORSAR Sci. Rep.*, *3-77/78*, Norw. Seismic Array, Oslo.

Knopoff, L., & Hudson, J.A., 1964, Scattering of elastic waves by small inhomogeneities, *J. Acoust. Soc. Am.*, *36*, 338–343.

Knopoff, L., & Hudson, J.A., 1964, Frequency dependence of amplitudes of scattered elastic waves, *J. Acoust. Soc. Am.*, *42*, 18–20.

Kuperman, W.A., & Schmidt, H., 1989, Self-consistent perturbation approach to rough scattering in stratified media. *J. Acoust. Soc. Am.*, *86*, 1511–1522.

Maradudin, A.A., Michel, T., McGurn, A.R., & Méndez, E.R., 1990. Enhanced backscattering of light from a random grating, *Annals of Physics*, *203*, 255–307.

O'Donnell, K.A. & Mendez, E.R., 1987, Experimental study of scattering from characterized random surfaces, *J. Opt. Soc. Am.*, 4, 1194-1205.

Prange, M., & Toksöz, M.N., 1990, Perturbation approximation of 3-D seismic scattering, *Geophys. J. Int.*, 101, 713-738.

Sanchez-Sesma, F.J. & Campillo, M., 1991, Diffraction of P, SV, and Rayleigh waves by topographical features: A boundary integral formulation, *Bull. Seism. Soc. Am.*, 81, 2234-2253.

Schultz, C.A. & Toksöz, M.N., 1993a, Enhanced backscattering of seismic waves from a highly irregular interface: SH case, *Geophys. J. Int.*, 114, 91-102.

Schultz, C.A. & Toksöz, M.N., 1993b, Enhanced backscattering of seismic waves from a highly irregular interface: P-SV case, *Geophys. J. Int.*, in press.

Singh, S.J. & Sikka, J.S., 1988, On 2-D dynamical dislocations, *J. Phys. Earth*, 36, 27-41.

Wu, R., & Aki, K., 1985, Scattering characteristics of elastic waves by an elastic heterogeneity, *Geophysics*, 50, 582-595.

## Appendix A: Numerical Formulation—Acoustic-Elastic Case

We numerically solve the integral equations (20) and (21) by first integrating them over a finite interval,  $L$ , then converting them to a set of  $3N$  linear equations. Separating each of the integrals into a sum of  $N$  integrals, each integrated over an increment  $\Delta x$ , centered at the interface points we can express (21), which represents the scattered displacement in the lower medium, as a sum over integrals centered at the points

$$x_n = -L/2 + (n - \frac{1}{2})\Delta x, \quad n = 1, 2, 3, \dots, N. \quad (\text{A.1})$$

Evaluating the total displacement at the center of each element,  $x_m$ , the integral approximations can be written as

$$T_{i0}^{n(s)}(x_m|x_n) = \int_{x_n - \frac{\Delta x}{2}}^{x_n + \frac{\Delta x}{2}} dx'_1 T_i^{n(s)}(x_m|x'_1), \quad (\text{A.2})$$

$$D_{p0}^{n(l)}(x_m|x_n) = \int_{x_n - \frac{\Delta x}{2}}^{x_n + \frac{\Delta x}{2}} dx'_1 D_p^{n(l)}(x_m|x'_1),$$

which we solve for  $k\Delta x$  very small.

In the acoustic medium the integrals which we must approximate analytically can, assuming that the source amplitude functions 24 are slowly varying along the interface, be written as

$$T_0^{(f)}(x_m|x_n) = \int_{x_n - \frac{\Delta x}{2}}^{x_n + \frac{\Delta x}{2}} dx'_1 T^{(f)}(x_m|x'_1), \quad (\text{A.3})$$

$$D_{i0}^{(f)}(x_m|x_n) = \int_{x_n - \frac{\Delta x}{2}}^{x_n + \frac{\Delta x}{2}} dx'_1 D_i^{(f)}(x_m|x'_1),$$

and it can be easily shown by letting  $x_3 = \zeta(x_1) + \epsilon$  and integrating all terms corresponding to first order in  $k_T^{(f)} \Delta x$  in the limit as  $\epsilon \rightarrow 0^+$  that the boundary integral formulation in the fluid can be represented as a simple combination of both the elastic approximation and the SH approximation (Schultz and Toksöz, 1993a). In the acoustic medium the Green's function terms are written as

$$\begin{aligned} D_i^{(f)}(\underline{x}|\underline{x}') &= \lambda^{(f)} k_T^{(f)2} G^{(f)}(\underline{x}; \underline{x}') n_i & (A.4) \\ T^{(f)}(\underline{x}|\underline{x}') &= T^{(SH)}(\underline{x}|\underline{x}') [\mu \rightarrow \lambda] \end{aligned}$$

where the traction term is identical to the SH traction term with  $\lambda^{(f)}$  in the fluid is substituted for  $\mu$  in the SH case. In the elastic medium these terms can be written as

$$\begin{aligned} D_n^{(s)}(\underline{x}|\underline{x}') &= \mu^{(s)} G_{np}^{(s)}(\underline{x}; \underline{x}') n_p & (A.5) \\ T_i^{n(s)}(\underline{x}|\underline{x}') &= T_i^{n(s)}(\underline{x}|\underline{x}') \end{aligned}$$

where the traction term is just that of the P-SV case. The displacement term is a function of the elastic Green's function developed in the P-SV formulations. In the case of integrating over singularities, expressing the integrands as a combination of Taylor and asymptotic series expansions, keeping terms up to order  $k_T^{(f)} \Delta x$ , and integrating over  $\Delta x$  gives a solution which reduces to a simple combination of the SH and P-SV solutions. This includes the first term in A.5 which multiplies an additional normal function. A direct substitution from Schultz and Toksöz (1993a) and Schultz and Toksöz (1993b) gives the final linear system of equations which is then solved.

## Appendix B: Ultrasonic Design

All experiments were done in our in-house ultrasonic water tank laboratory. Ultrasonic water tank modelling is a powerful tool as real field situations can be scaled down by four to five orders of magnitude and studied in a well controlled laboratory environment. The first section of this appendix describes the ultrasonic configuration. The second section describes in detail the construction of a four layer piezo-film receiver.

### Ultrasonic Water Tank Design

A diagram of the experimental setup is shown in Figure B.1. A solid elastic model is submerged in a water tank measuring 1.0 m by 0.5 m by 0.5 m in height. An ultrasonic wave is generated at a given source transducer with an input voltage from a Hewlett Packard 3048A function generator. For voltage output above  $+/- 5$  V a Hewlett Packard 467A Power Amplifier was utilized to obtain a  $+/- 10$  V of output. The source function generator was used to create a finite length sine wave with a specific frequency and a finite number of cycles. The input wave, received with a corresponding piezoelectric material, is amplified from 40 to 60 db with a Panametrics 5660B preamplifier.

In the case of the finite pulse seismograms, a Krohn-Hite 3202R high-low cutoff filter was applied to the input signal. In the continuous wave study the input voltage was increased and the filter bypassed to remove any distortion it may cause. Signal to noise ratios were improved by stacking recorded signals (usually 8 stacked shots). The final signal was then digitized by

a Data Precision DATA 6000 digital oscilloscope with 12-bit amplitude resolution. Although the system can simulate a full 3-D seismic study using six automated step motors, this study was carried out with only one motor. The receiver was connected rigidly to a rotating arm and then rotated in a semicircle about a rotation axis in  $.9^\circ$  steps. The digitizer and the step motor controller are interfaced with an IBM PC-AT computer through an IEEE-488 interface bus. The final digitized data is stored in the IBM PC-AT and following the experiment, is transferred to a Digital DECstation 5000/25 machine. The total time required to record and transfer the pressure recorded for a single realization of an interface was on the order of one hour.

### **Piezo-Film Receiver**

In designing an experiment which can study the energy scattered at and near retroreflective angles (energy travelling back towards the source), one must be able to place a receiver very close to the source. There are a number of approaches which allow recording directly in this region. One approach is to make the source as small as possible so that when the receiver gets near the source it does not interfere with the incident beam. The smaller the source and receiver the more the information recorded at retroreflective angles. A second approach is to use a focusing beam which has its focus at the receiver. In this case the beam is its narrowest at the receiver allowing recording very near the source angle. A third approach is to use an acoustic beam splitter, which reflects incident energy, coming from the side of the

experiment, towards the interface and then allows energy to pass back through the splitter on its second pass to the receiver. The fourth approach is to create a receiver which is transparent to acoustic energy giving one free reign to record about the source transducer. Unfortunately, the first two approaches are not applicable to this study. The first option is not practical since the size of the source transducer is required to be larger than a certain limit to propagate a narrow acoustic beam. The second option is also difficult to implement because of the water tank dimensions. If the beam is focused on a receiver located only a short distance away the beam spreading becomes too large.

We therefore chose the fourth approach. We describe a piezo-film transducer that is essentially transparent to acoustic energy. Figure B.2(a,c) shows a detailed view of the piezo-film receiver configuration. In the case of a single piezo-film layer, the film is placed between two silver conducting layers. Since the signal received comes only from areas covered by conducting metal, it is advantageous to apply the metal coating as a liquid glue which allows for full control over the receiver's shape and its sensitivity. In this study the conducting element was given the same circular shape as the flat-bottomed transducers described earlier. Due to the low sensitivity of one layer of piezo-film, it is desirable to stack multiple layers. However, there is a balance between the thickness of the receiver and its impedance contrast. As more piezo-film layers are stacked the impedance of the stack increases quickly. For this study, a four layer stack shown in Figure B.2(c) using  $110\mu$  film was optimal. The final thickness of the piezo film is approximately  $550\mu$  thick with a transmission efficient at

normal incidence of approximately 0.78. This leaves the piezo-film with a .22 reflection coefficient. As a result, reflected energy does reverberate between the source and receiver retaining a very high amplitude. A recording window was chosen such that it did not include any of this reverberative energy.

The final sheet, measuring .25 m by .12 m, was supported around the edges using a thin frame (Figure B.3). In addition to supporting the film, the frame was used to bend the sheet so it followed the curvature of the semicircle about which the receiver is stepped. This guaranteed that the source beam was normally incident on the film during receiver rotation, therefore reducing any source beam distortion created by oblique incidence.

As this is a new transducer design, the receiver properties were studied. Figure B.4 shows the receiver sensitivity pattern as a function of incident wave angle, with an incident frequency of 500 kHz. The stacked piezo-film receiver has a very directed sensitivity pattern which is similar in nature to the flat-bottomed transducers with the same diameter. The piezo-film also appears to have a broad frequency response making it a very powerful tool. In addition, this element may be used successfully in rock physics to record on curved surfaces by gluing the film directly to the rock surface. This avoids the problem of transducer coupling encountered with a flat-bottomed transducer.

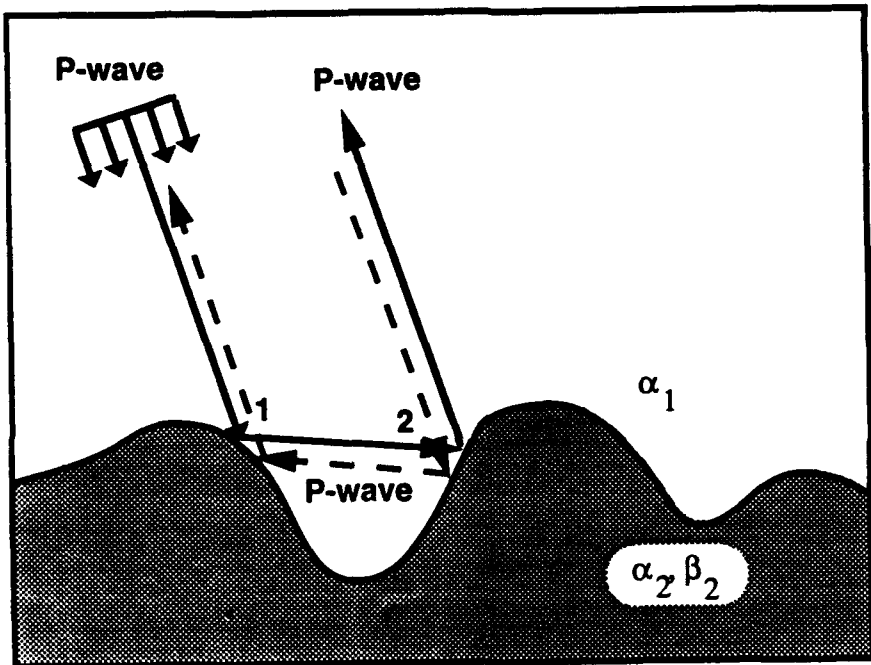


Figure 1: Peak-valley sequence along an interface showing an example of the time-reversed paths which lead to enhanced backscattering. The solid line shows a forward scattered path, while the dashed line shows the corresponding time-reversed path. These two paths constructively interfere to give an increase in amplitude diffracted back in the direction of the source.

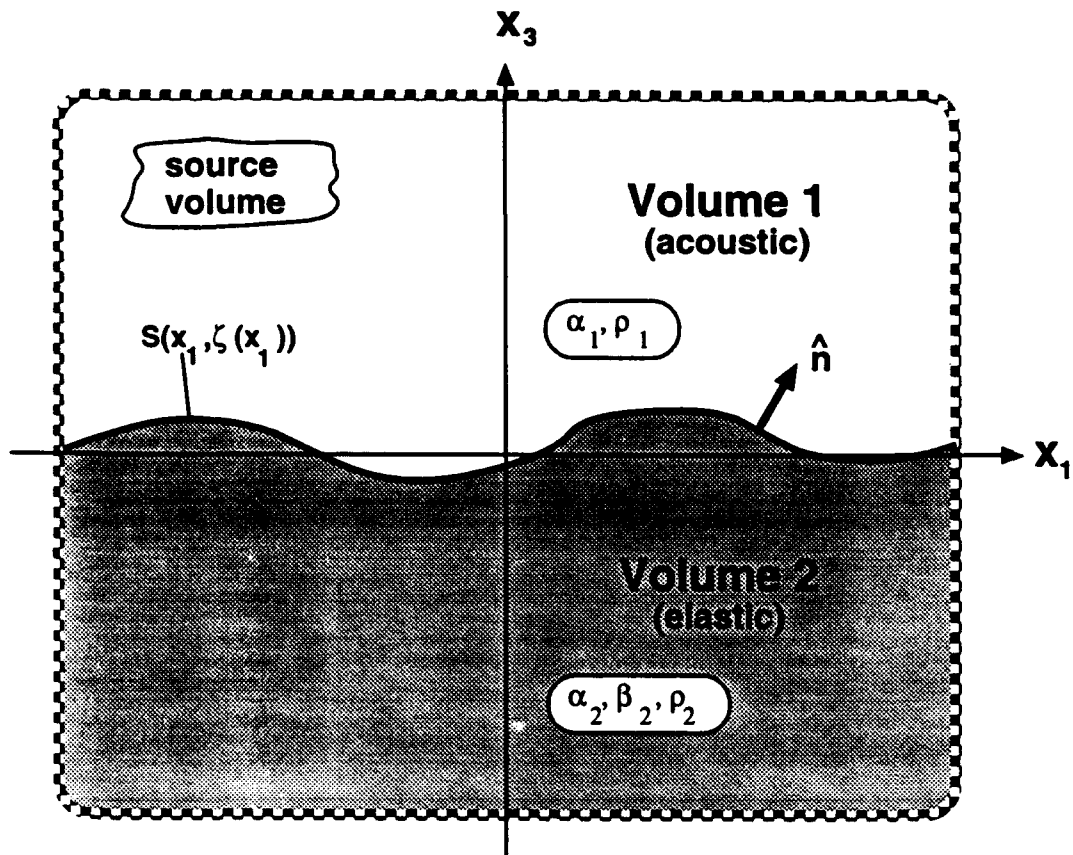


Figure 2: The geometry used to formulate the numerical model of scattering from a highly irregular interface. The upper acoustic volume is separated from the lower elastic medium by a highly irregular acoustic-elastic interface represented by the surface,  $S(x_1)$ .

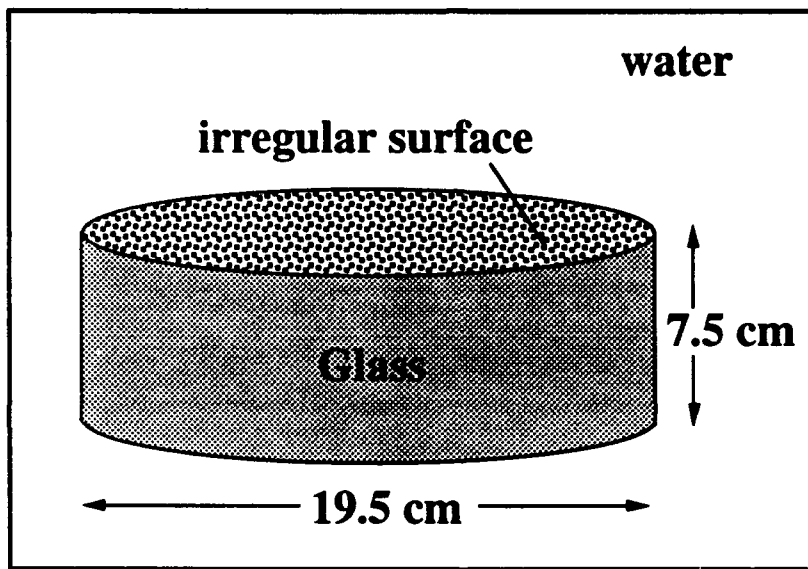


Figure 3: The cylindrical glass block model utilized in this study. The upper circular surface of this glass block was etched to give a randomly irregular geometry and then this block was submerged in water to create an irregular acoustic-elastic interface. Measurements show this block to have a P wave and S wave velocity of 5600 m/s and 3200 m/s, respectively. The density of the block is approximately 2.65.

## GENERATING THE INTERFACE

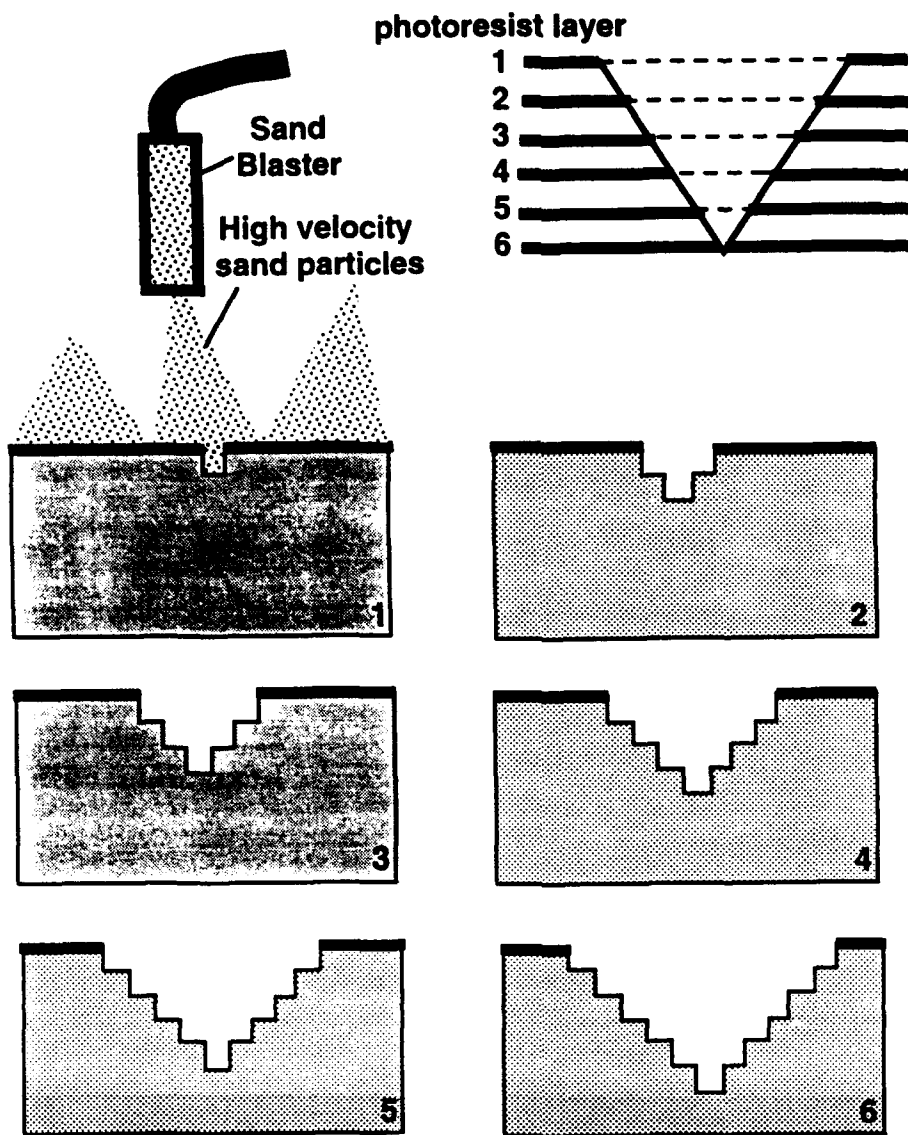


Figure 4: The general approach used to etch a specific surface geometry given a smooth glass surface. The valley shown above is etched in discrete levels using high velocity sand particles and a photoresist layer which shields the glass covered by photoresist from chipping. Therefore the the valley is slowly deepened and broadened at each level until the desired valley is achieved.

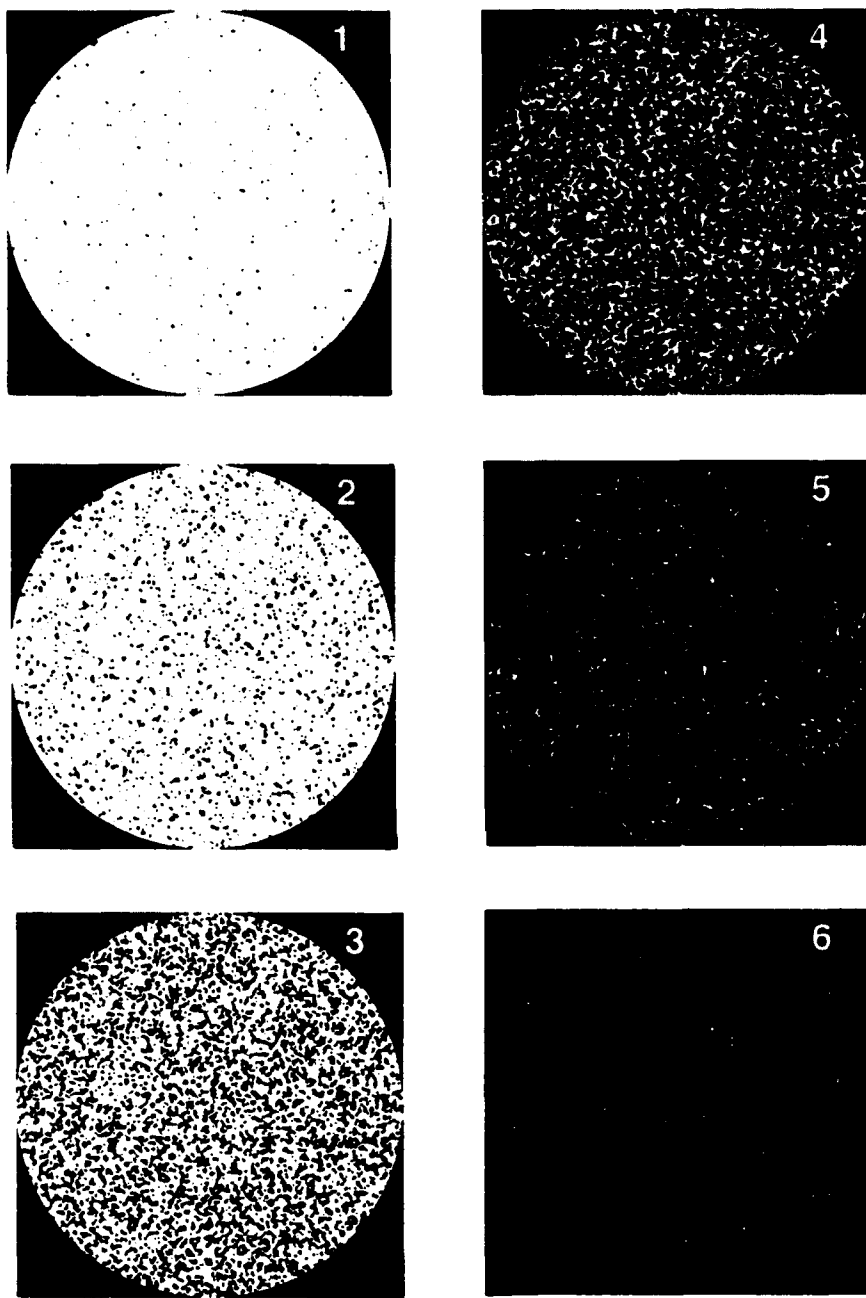
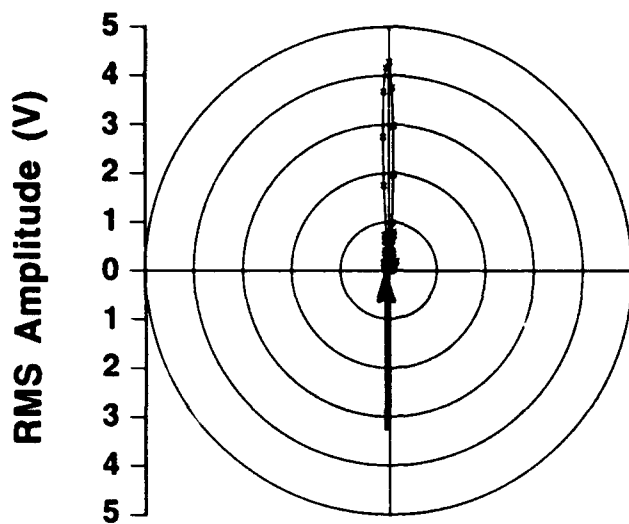


Figure 5: The six templates used to generate the random surface used in these experiments. Each circle has a 19.5 cm diameter to match the glass surface. Each template corresponds to one standard deviation of depth and each template was exposed to high velocity particles for the same amount of time. The numbering shows the order in which the templates were applied.

(a) **Source Radiation Pattern**



(b) **Source Radiation Pattern**

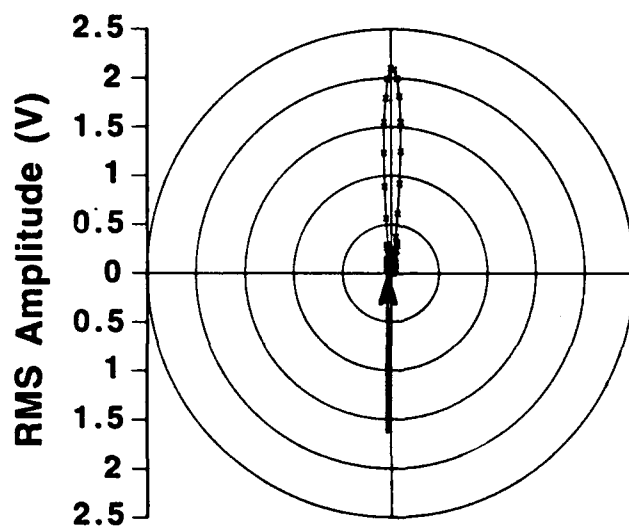
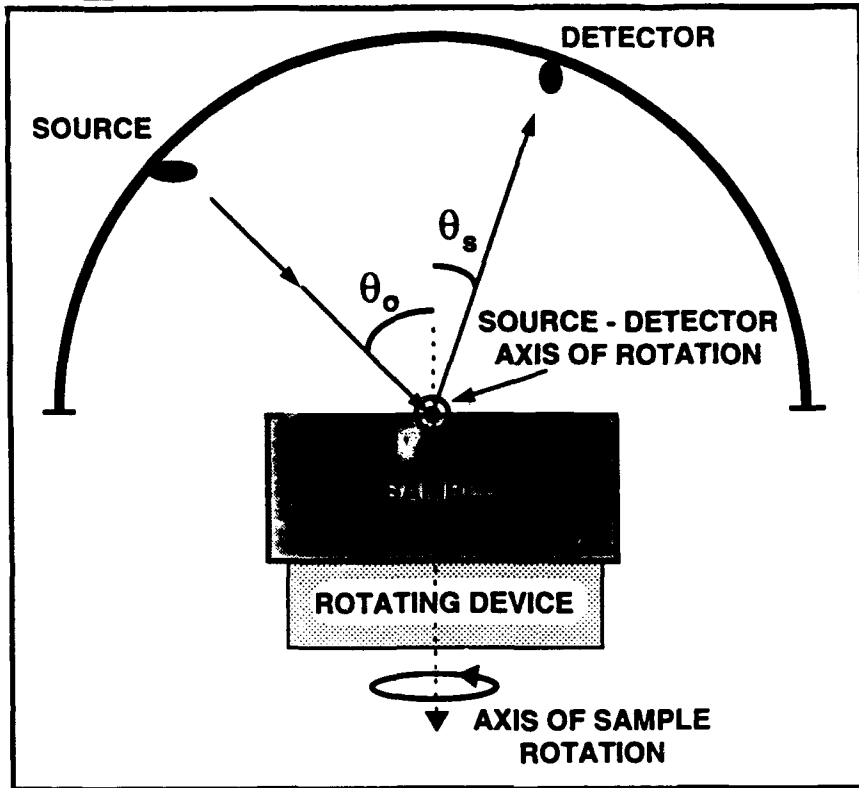


Figure 6: Source radiation pattern for the two flat-bottomed panametrics transducers used in this study. Shown are the radiation pattern (a) for a 12.7 mm (1/2 in) source operating at 1.5 MHz ( $\lambda = 1.0$  mm) in water and the radiation pattern (b) for a 25.4 mm (1 in) source operating at 0.5 MHz ( $\lambda = 3.0$  mm) in water.

SIDE VIEW



TOP VIEW

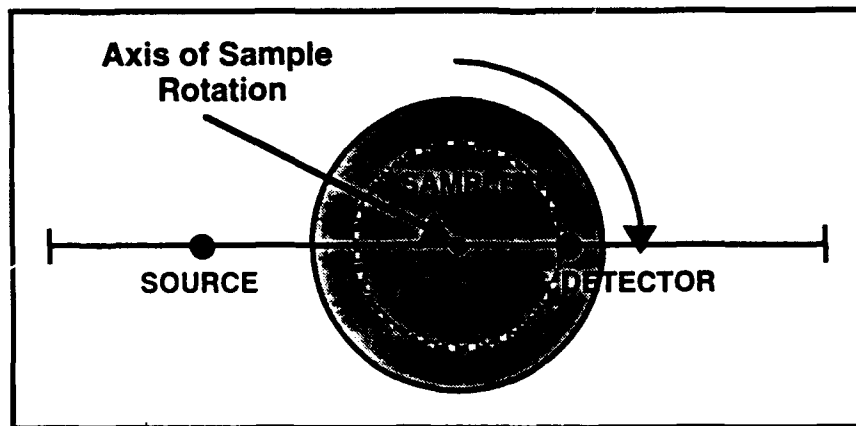


Figure 7: The geometry used to experimentally measure the scattering properties of a given random surface. The source is held stationary at one incident angle while the detector is stepped in a semi-circle about the random surface. This then gives one realization of that surface.

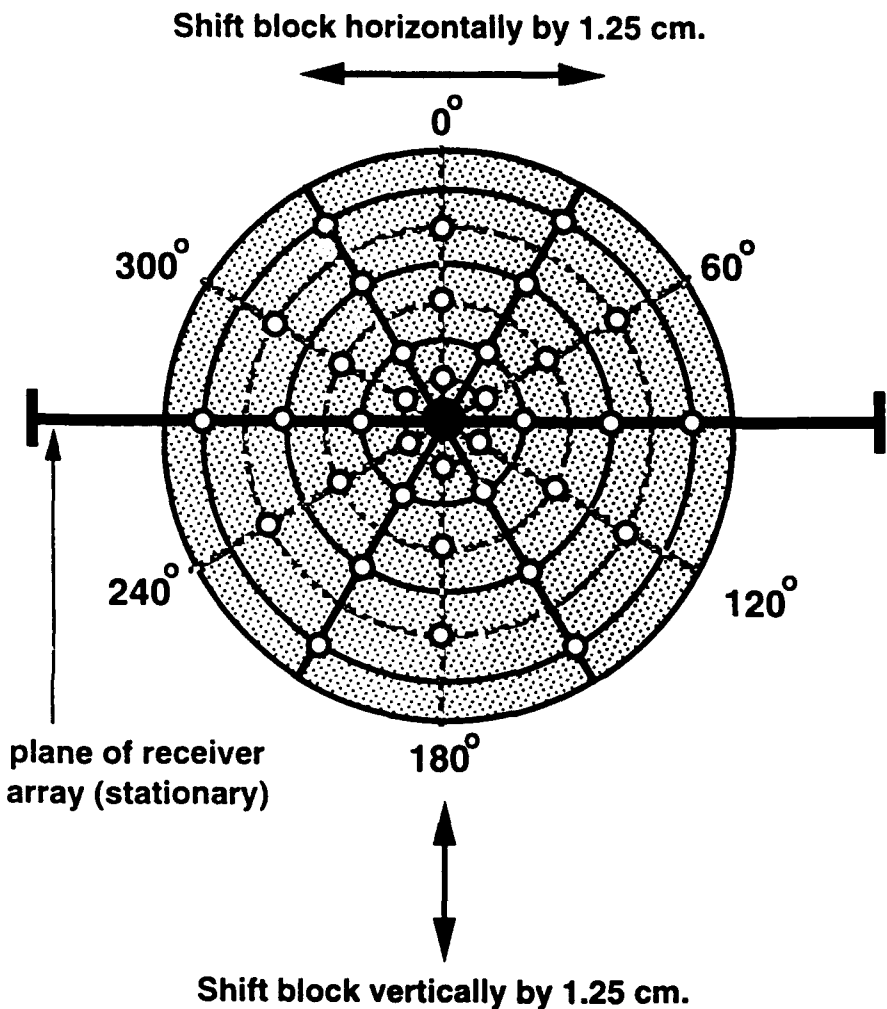


Figure 8: The rotation scheme used to generate many realizations of the interface. The sample is shifted left and right by 1.25 cm steps and the block is rotated by staggered 60° steps to give 6 independent realizations of the surface where the axes of rotation for the realization sit along concentric circles on the surface. This gives a total of 72 surface realizations. An additional 72 realizations can also be sampled by shifting the block up and down by 1.25 cm steps.

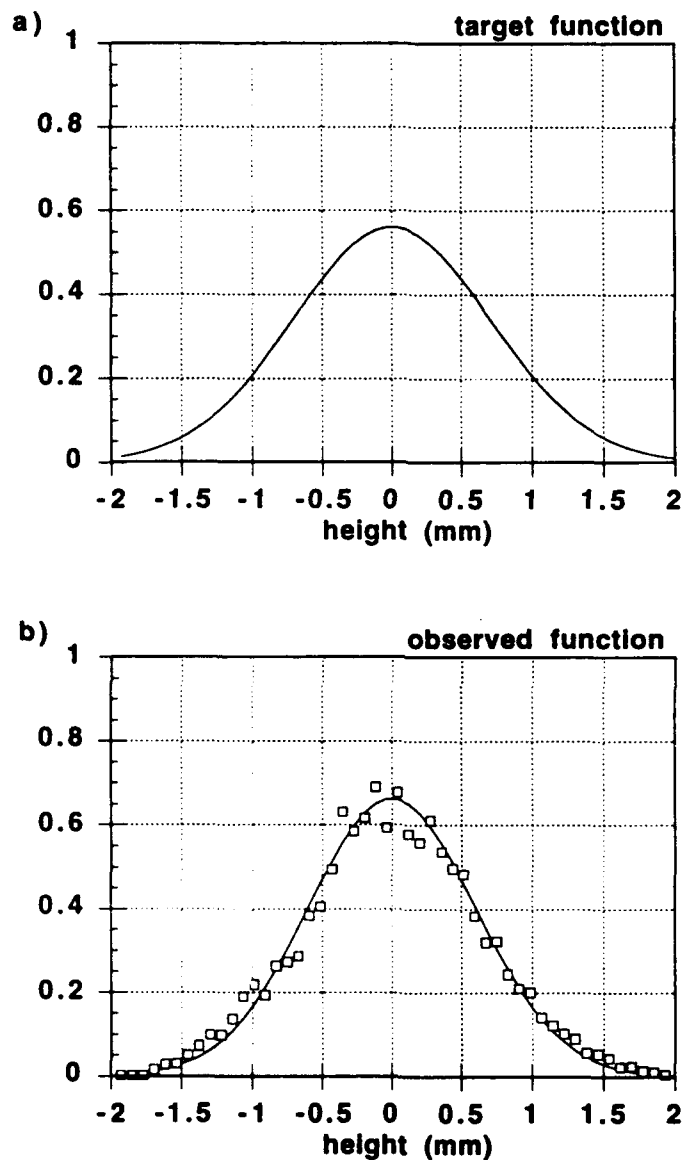


Figure 9: Histogram plotting surface height data. The target surface height distribution (a) is Gaussian with a standard deviation 1 mm. The surface height distribution (b) based on profilometer measurements (squares) of the glass surface is shown along with a best fitting Gaussian curve (solid line) which has a standard deviation of 0.6 mm. This histogram was plotted using 40000 surface profilometer measurements.

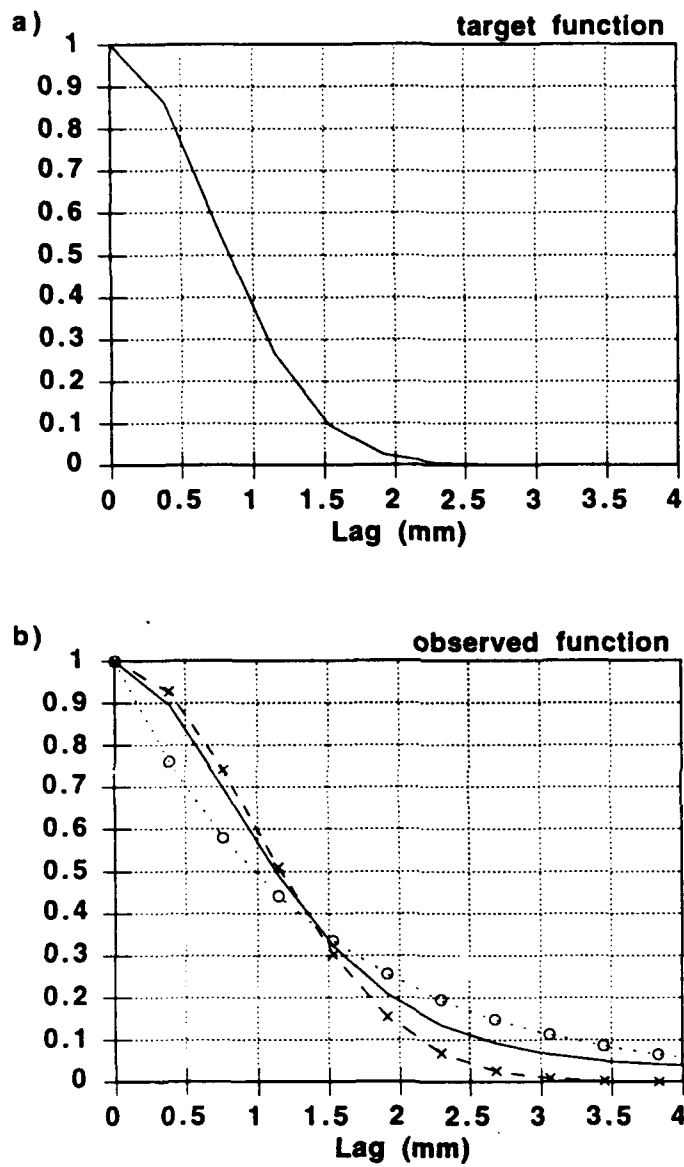


Figure 10: The interface autocorrelation function. The target autocorrelation function (a) is a Gaussian function with a correlation length  $e^{-1}$  of 1.0 mm. The actual autocorrelation function of the glass block (b) as calculated from profilometer measurements has a correlation length of 1.4 mm. The surface profilometer measurements (solid line) are compared with Gaussian (crosses) and Exponential (circles) functions with the same correlation lengths of 1.1 mm.

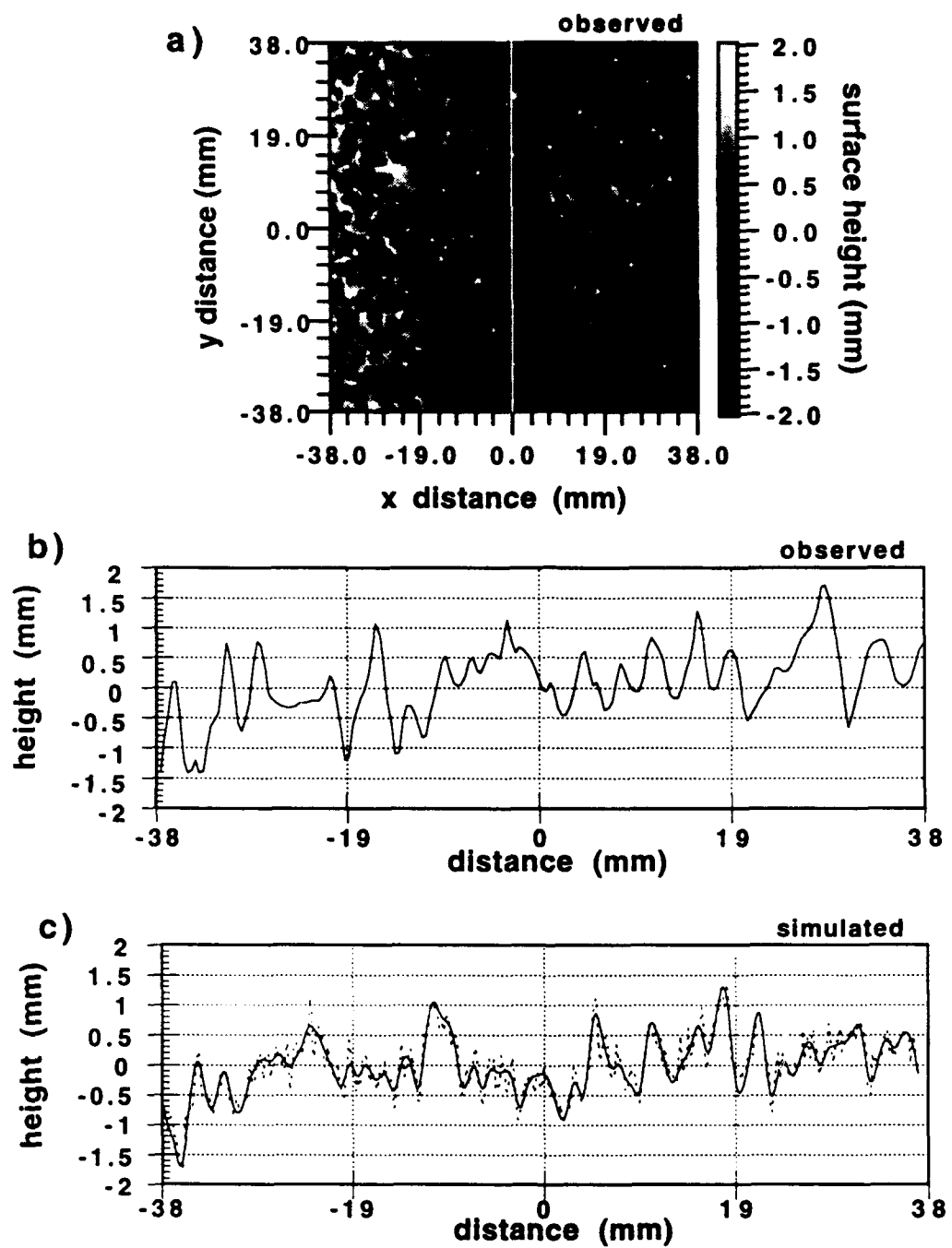


Figure 11: The surface height distribution based on profilometer measurements. (a) gives a grayscale plot of the surface. (b) gives a profile across the surface as marked in (a), and (c) shows a numerically generated surface with the statistics given in Figures 9 and 10. Both Gaussian (solid line) and exponential (dashed line) correlation functions are shown.

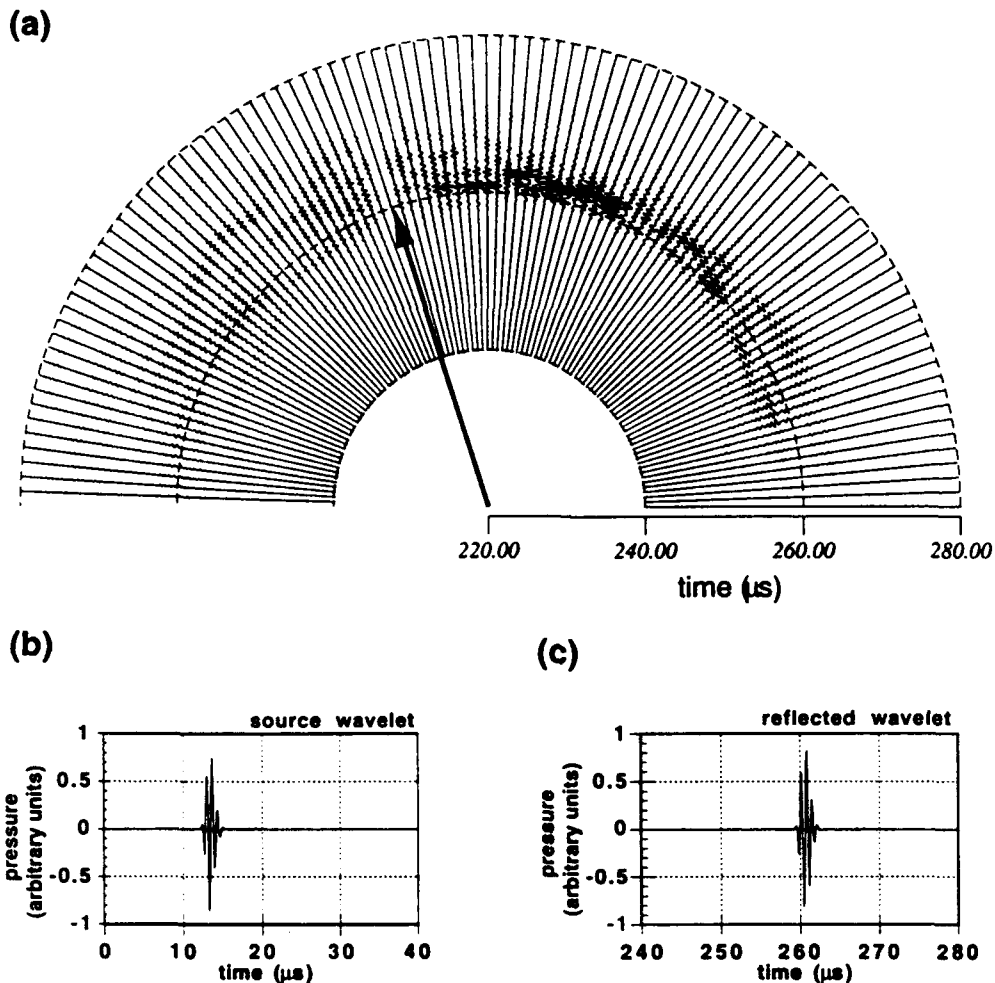


Figure 12: Experimental seismogram recorded on the glass model. (a) shows the seismic data recorded as a function of angle over the circular glass surface with  $\lambda = .71a$  given an acoustic beam incident at  $20^\circ$ . The arrow shows the retroreflective direction. The source wavelet (b) and the specular reflection (c) recorded over a plane interface are also shown. In the plane layer case the only observable energy is in the specular direction.

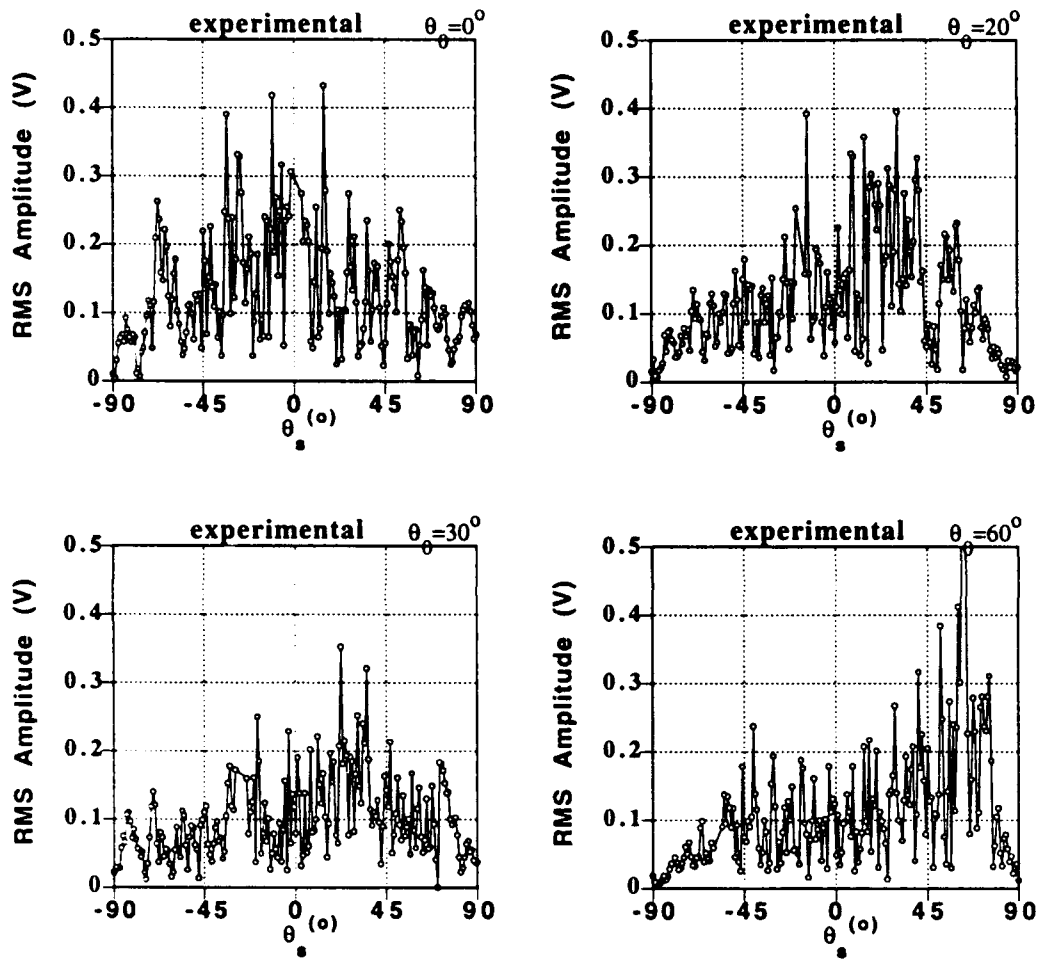


Figure 13: The amplitude recorded experimentally for one continuous wave realization of the fluid-glass interface given an acoustic beam incident at  $0^\circ$ ,  $20^\circ$ ,  $30^\circ$ ,  $60^\circ$ , respectively. The incident wavelength corresponds to  $\lambda = .71a$  and  $\theta_s$  is the angle of forward (positive) and back (negative) scattering.

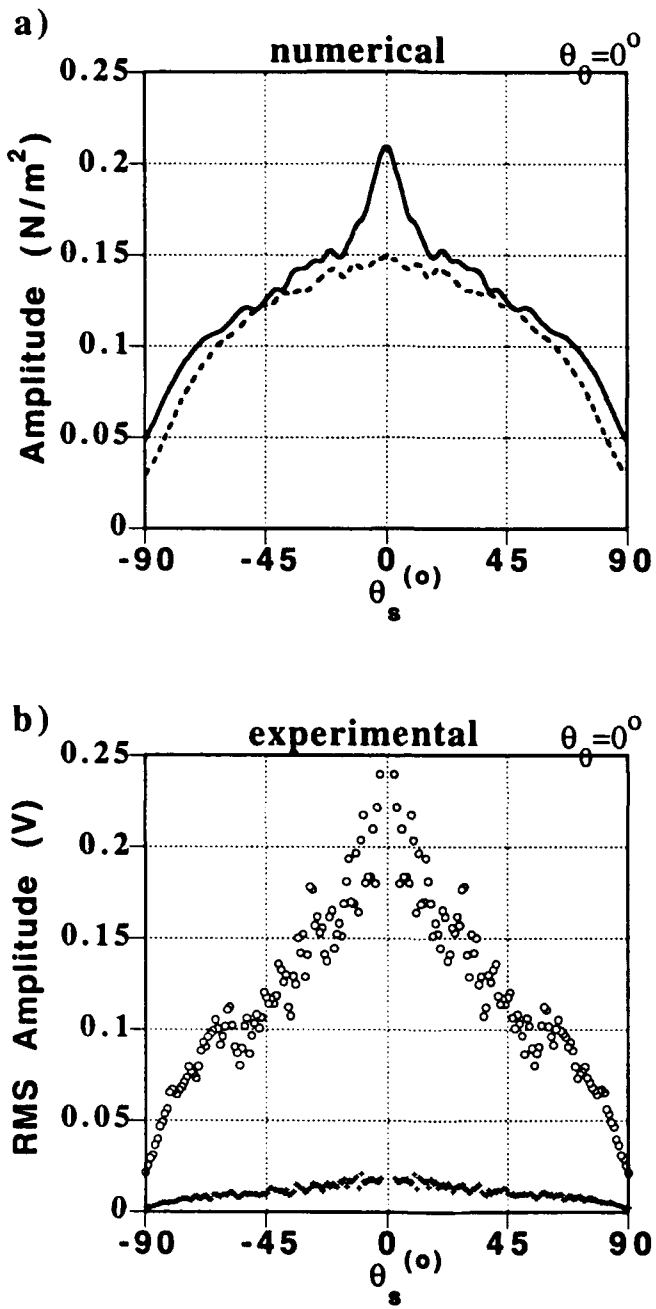


Figure 14: The 2-D mean reflection coefficient (a) calculated numerically over the Gaussian (solid line) and exponential (dashed line) surfaces given a normally incident source beam with  $\lambda = .71a$ . The 3-D reflection coefficient (b) recorded over the experimental interface (circles) and the standard deviation of the finite average (plus) are also shown. The experimental results correspond to 30 surface realizations.

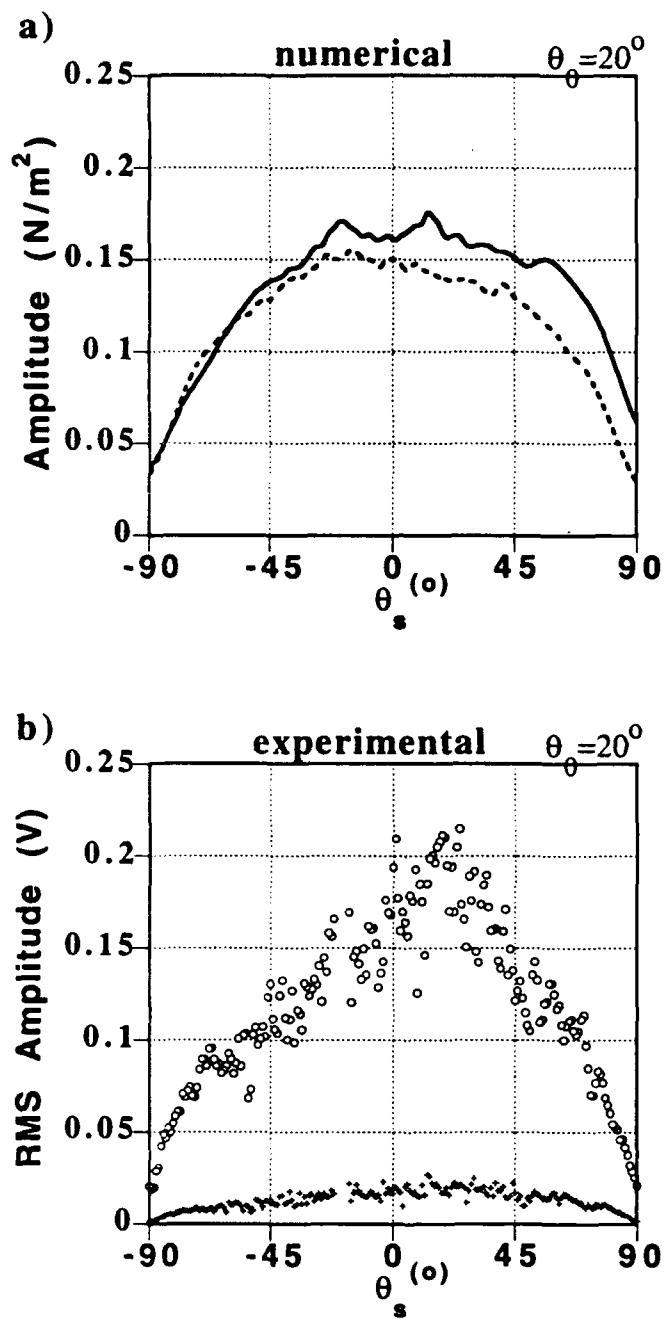


Figure 15: Similar to Figure 14 except the incident angle is now  $20^\circ$  and results correspond to 20 realizations.

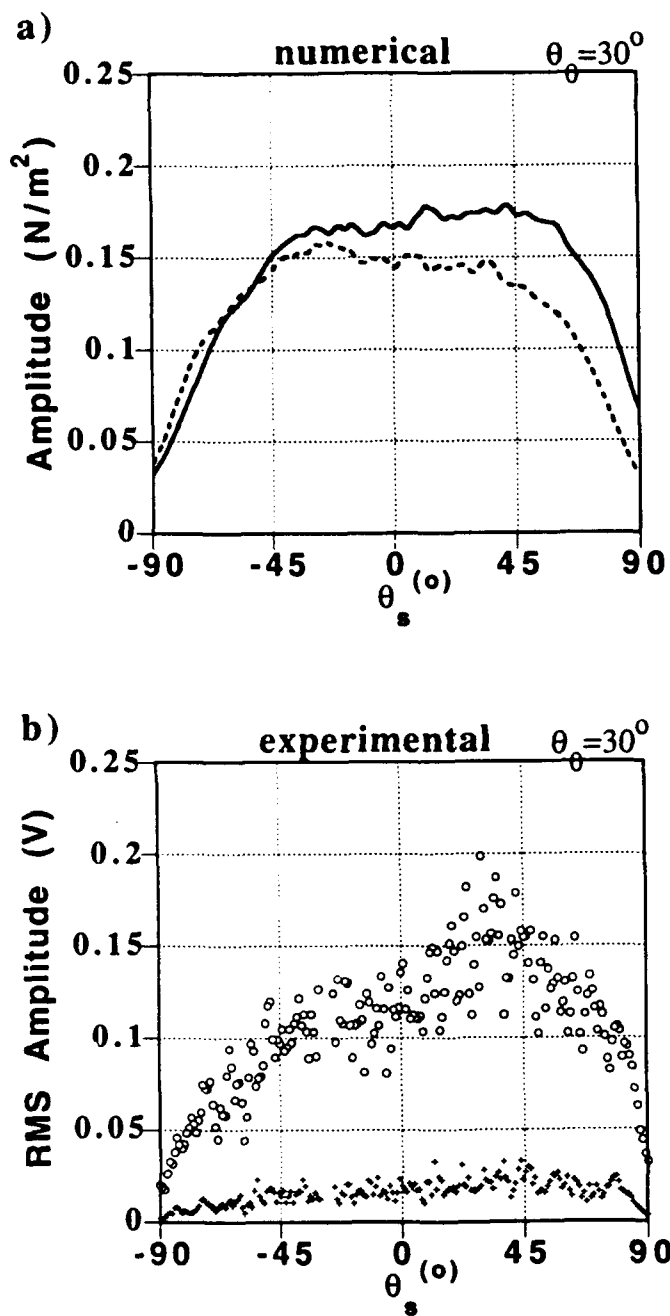


Figure 16: Similar to Figure 14 except the incident angle is now  $30^\circ$  and results correspond to 10 realizations.

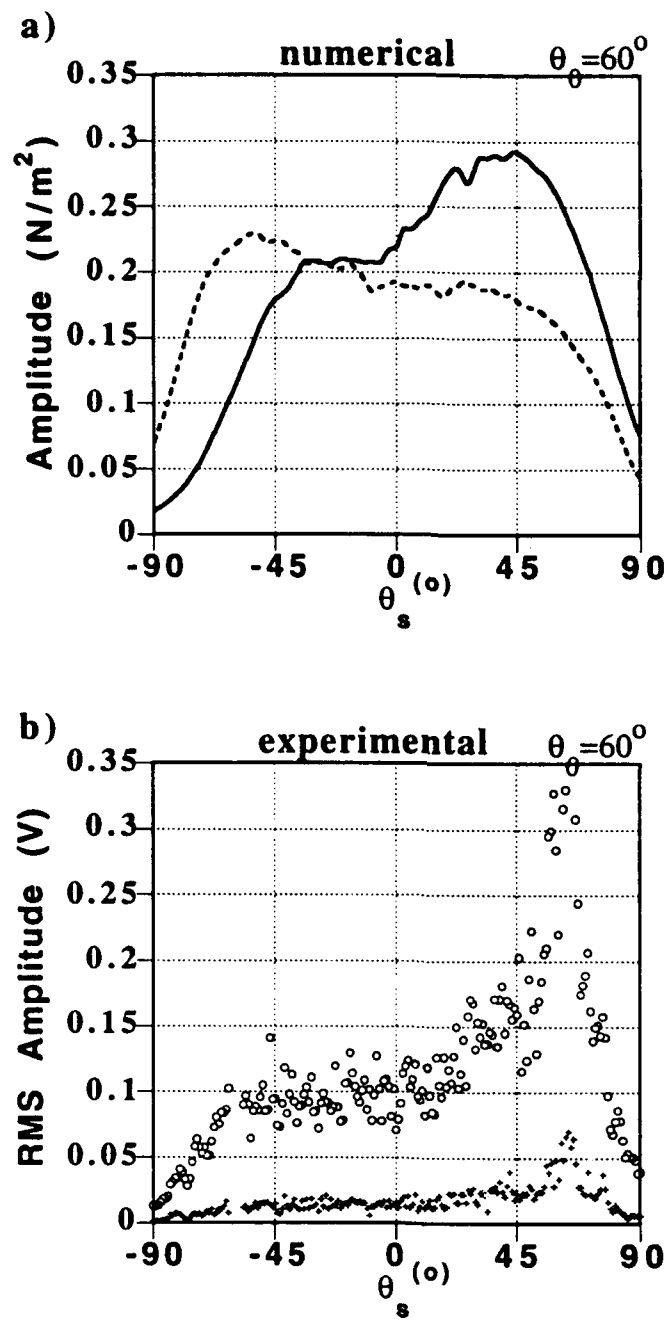
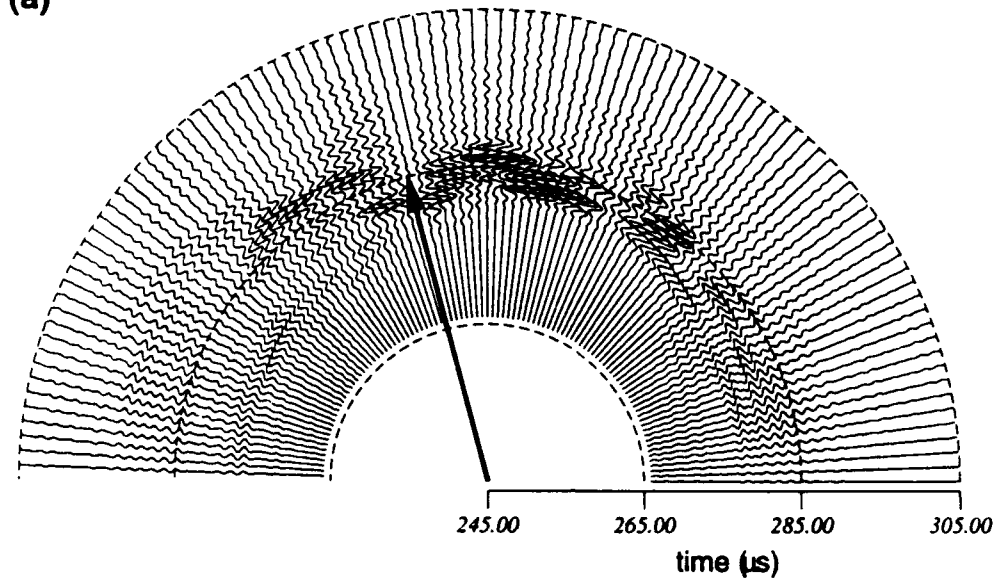
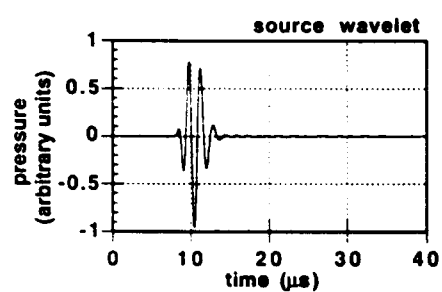


Figure 17: Similar to Figure 14 except the incident angle is now  $60^\circ$  and results correspond to 10 realizations.

(a)



(b)



(c)

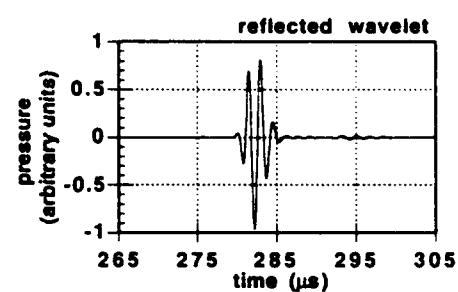


Figure 18: Similar to Figure 12, except  $\lambda = 2.14a$  and results correspond to 10 realizations.

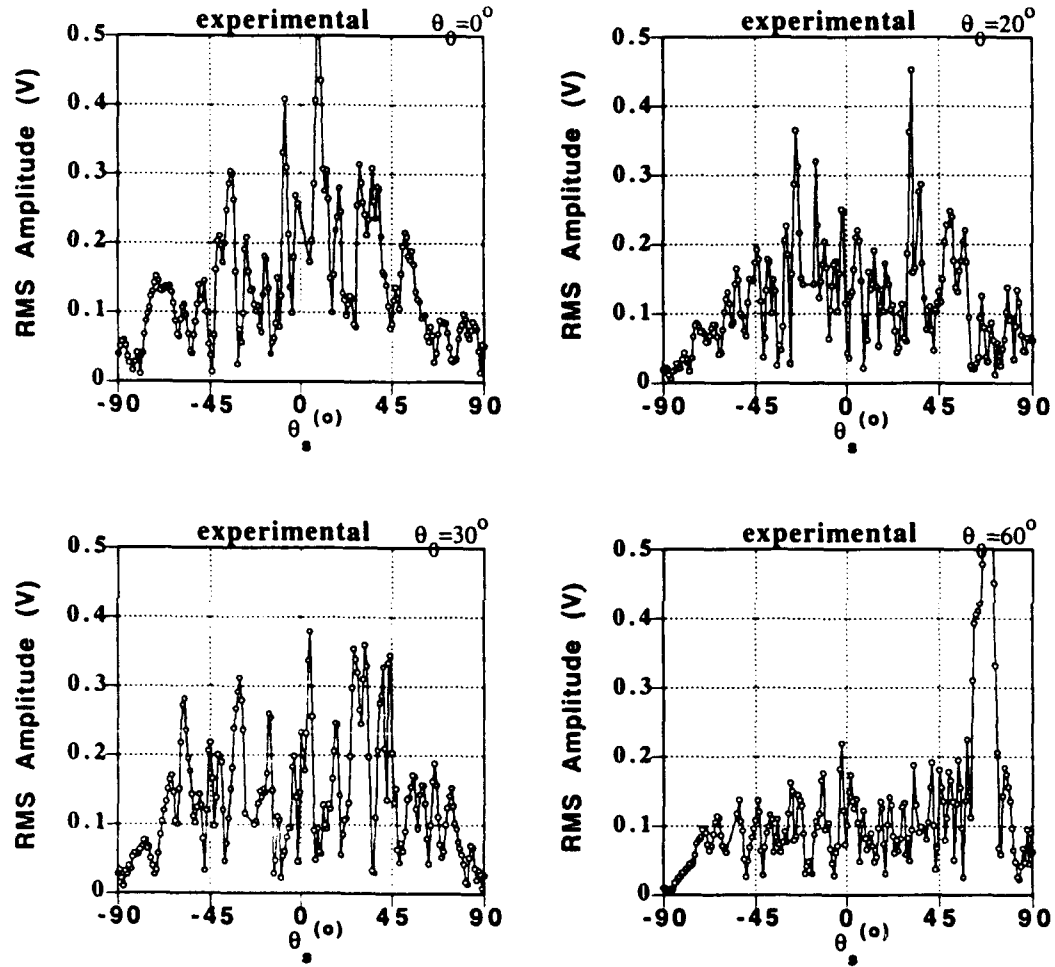


Figure 19: The amplitude recorded experimentally for one continuous wave realization of the fluid-glass interface given an acoustic beam incident at  $0^\circ$ ,  $20^\circ$ ,  $30^\circ$ ,  $60^\circ$ , respectively. The incident wavelength corresponds to  $\lambda = 2.14a$  and  $\theta_s$  is again the angle of forward (positive) and back (negative) scattering.

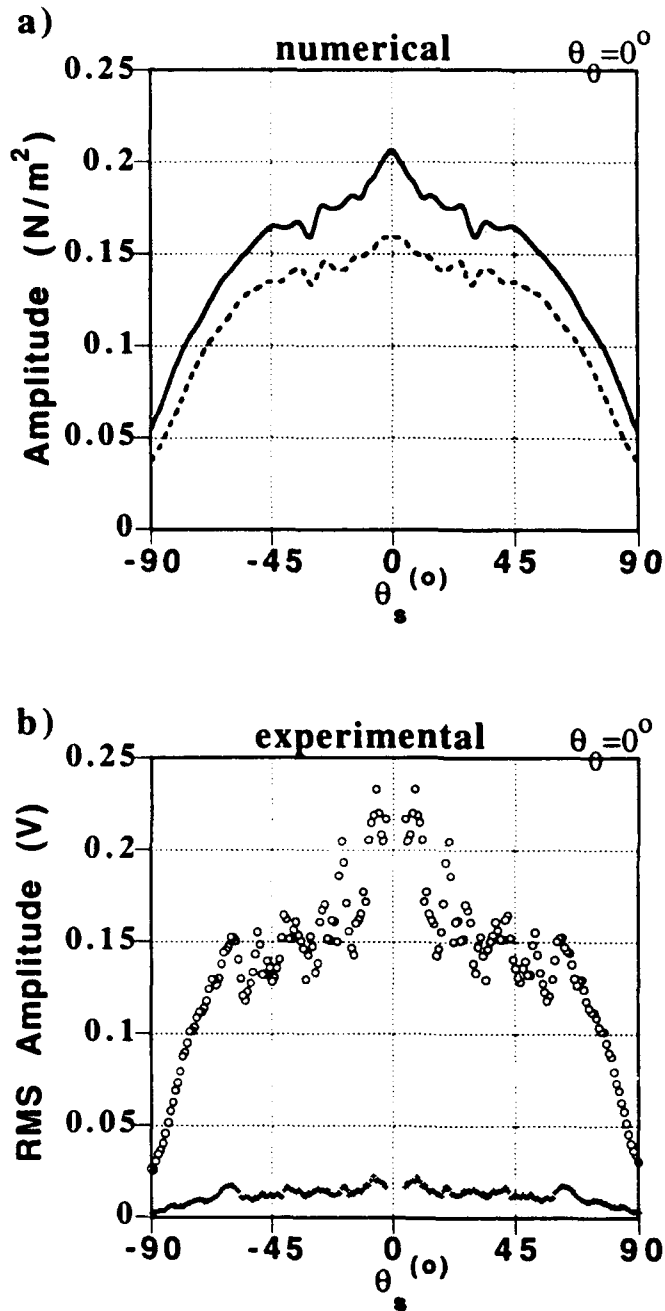


Figure 20: The 2-D reflection coefficient (a) calculated numerically over the Gaussian (solid line) and exponential (dashed line) surfaces given a normally incident source beam with  $\lambda = 2.14a$ .  $\theta_s$  is the angle of forward (positive) and back (negative) scattering. The 3-D reflection coefficient (b) recorded over the experimental interface (circles) and the standard deviation of the finite average (plus) are also shown. The experimental results correspond to 30 surface realizations.

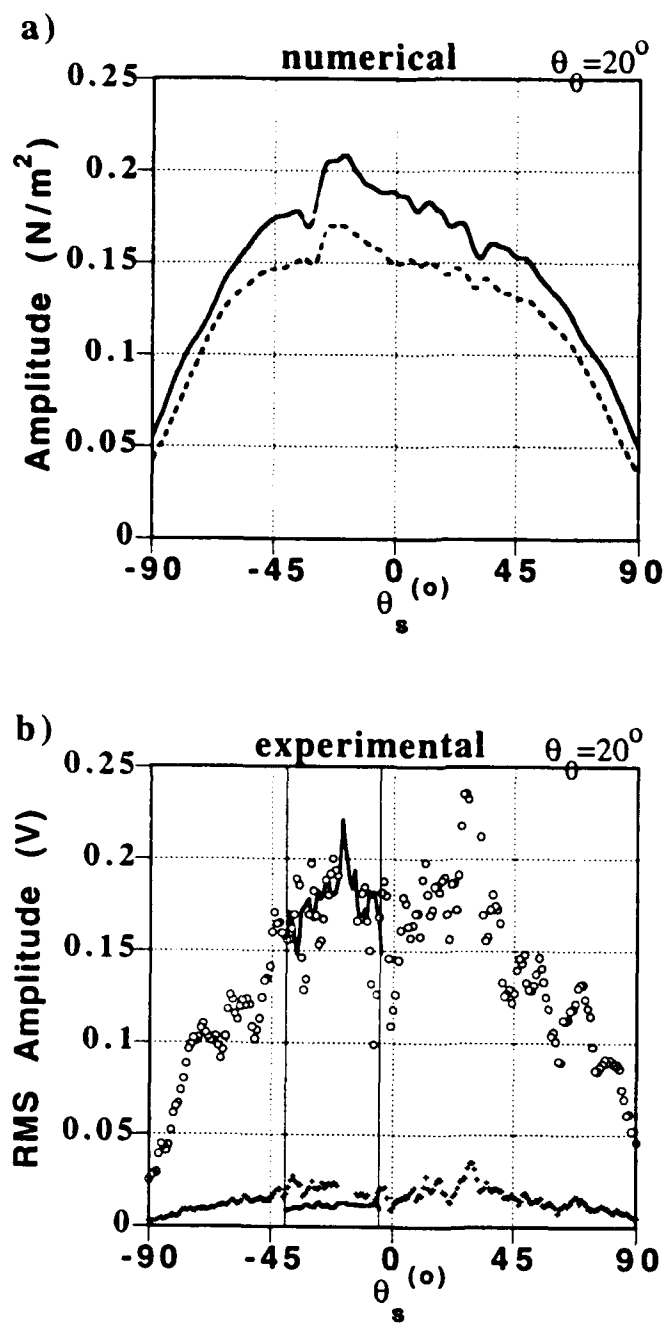


Figure 21: Similar to Figure 20 except the incident angle is now  $20^\circ$  and results correspond to 20 realizations.

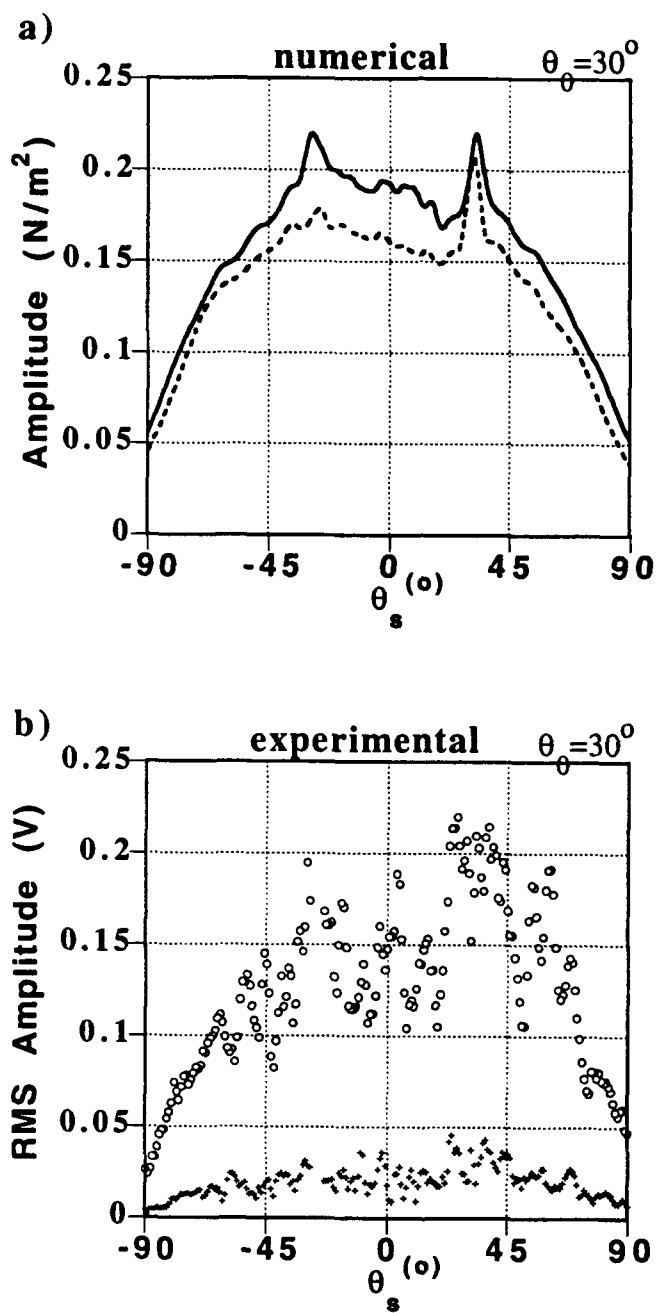


Figure 22: Similar to Figure 20 except the incident angle is now  $30^\circ$  and results correspond to 10 realizations.

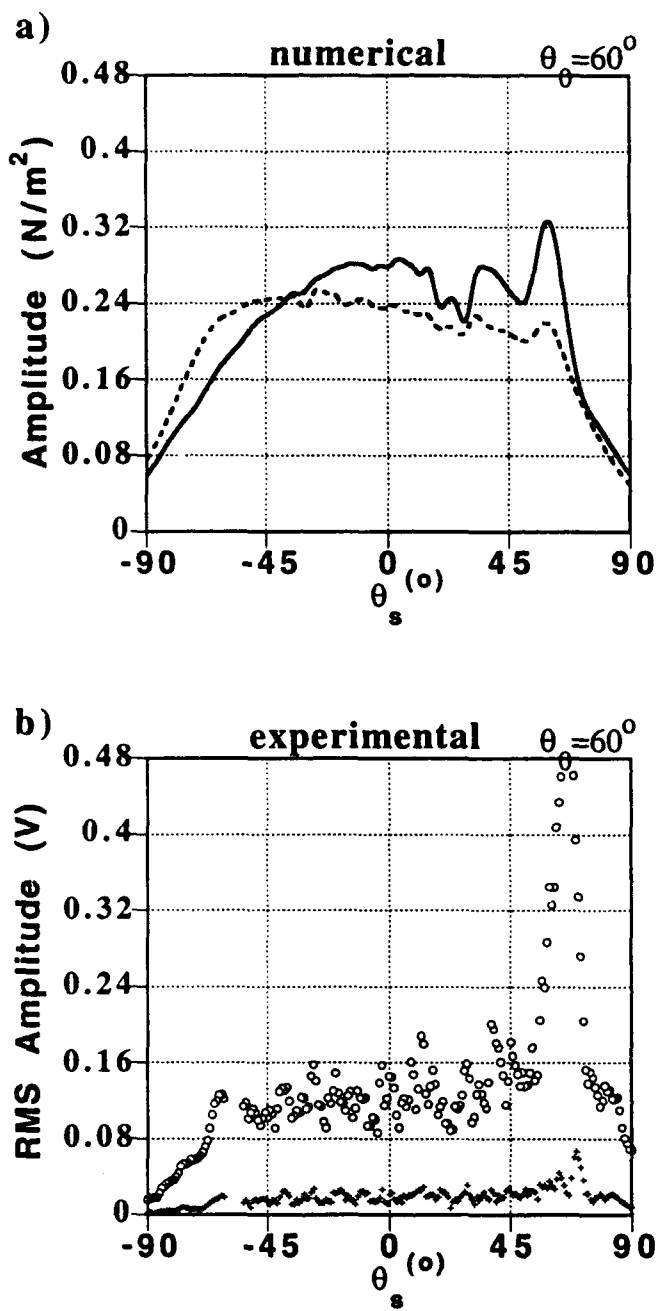


Figure 23: Similar to Figure 20 except the incident angle is now  $60^\circ$  and results correspond to 10 realizations.

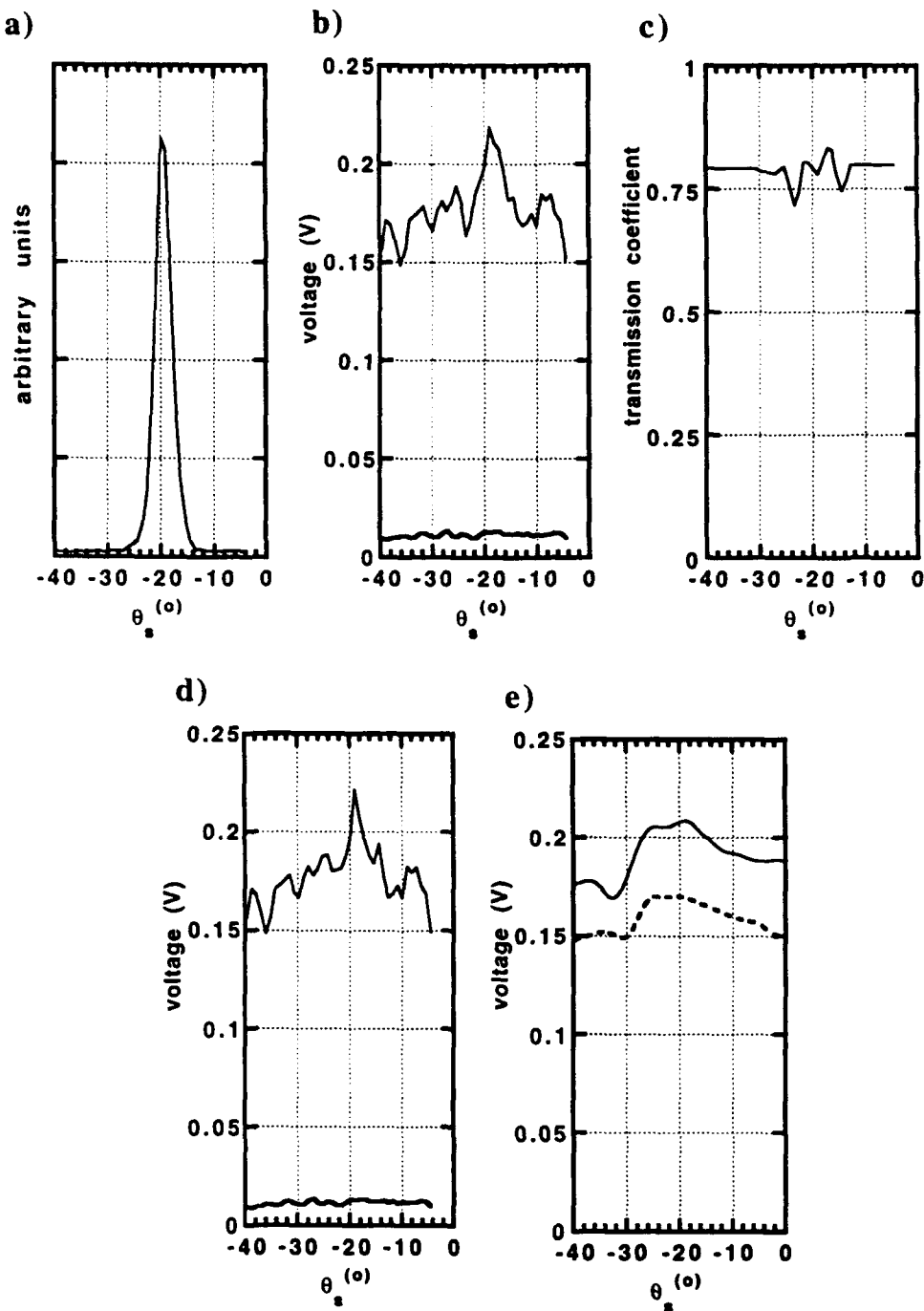


Figure 24: The data recorded about the retroreflection direction over the glass interface using a piezo-film receiver. Shown are (a) the incident source amplitude recorded with the piezo-film, (d) the average reflection coefficient for 65 surface realizations where (b) the raw data recorded has been corrected using (c) the transmission coefficient of the piezo-film receiver. The final reflection coefficient can be compared to (e) the numerically derived reflection coefficient for a 2-D interface.

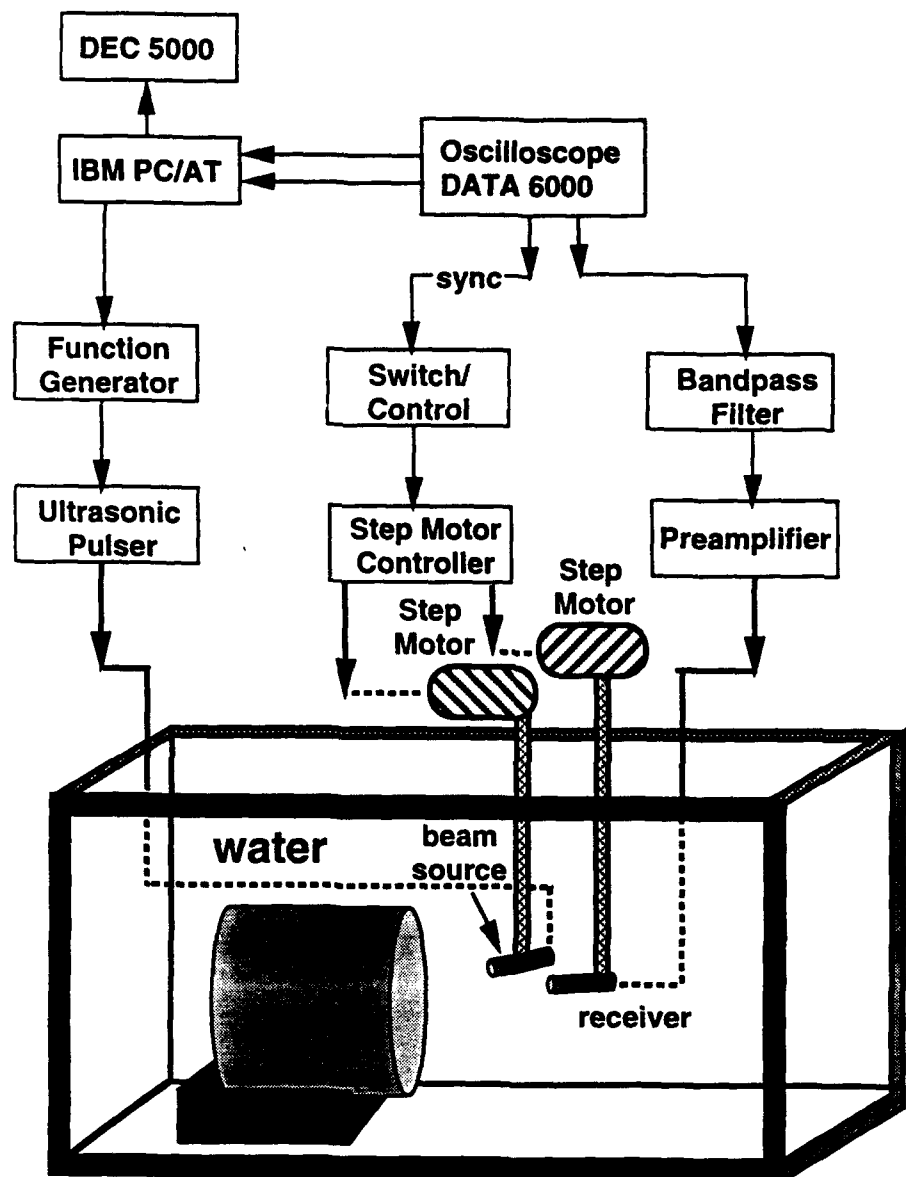


Figure B.1: The ultrasonic water tank configuration. The finite pulse measurements utilized the band-pass filter while the continuous wave measurements bypassed the filter, but used a power amplifier to increase the signal to noise ratio.

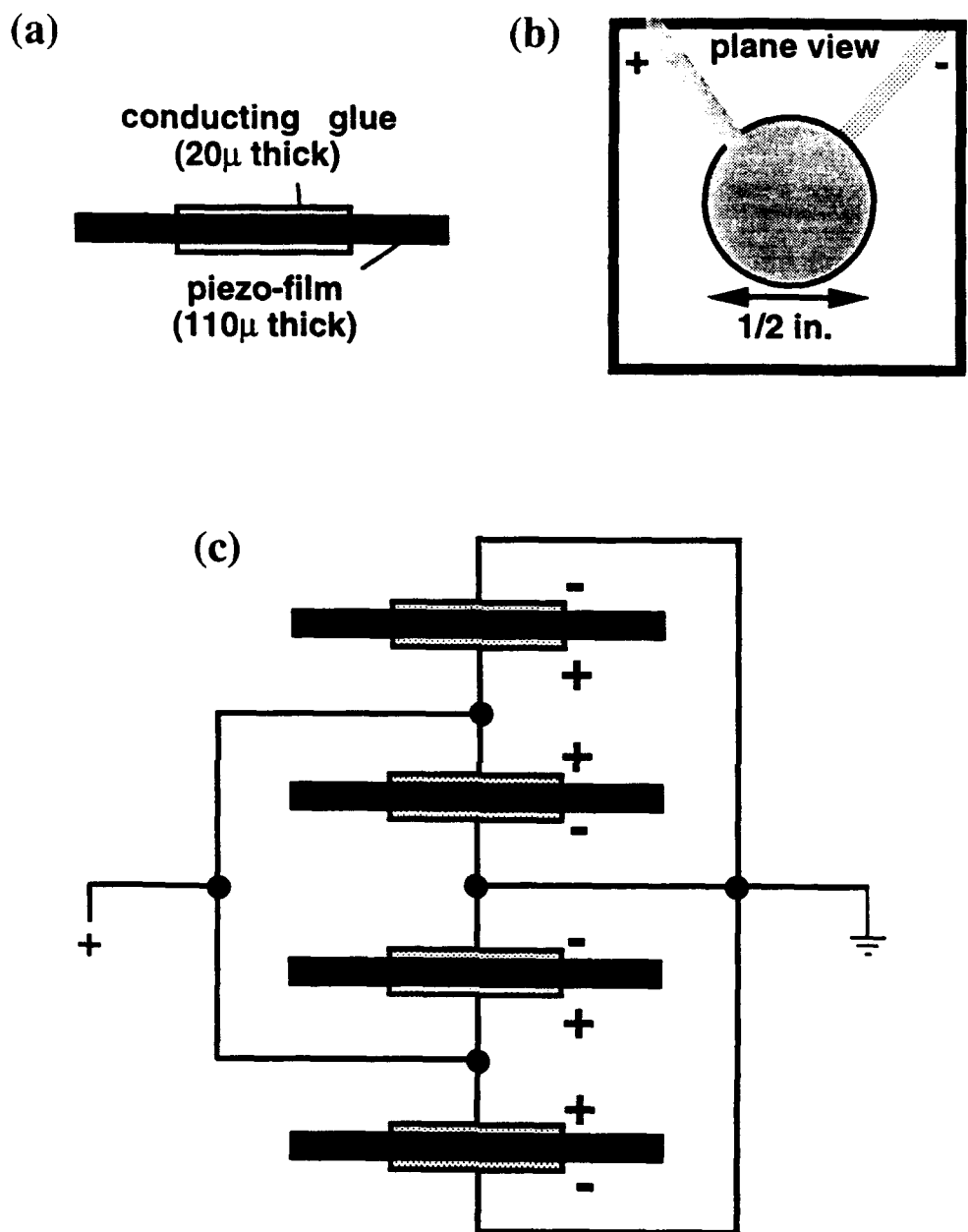


Figure B.2: The piezo-film receiver with 4 layers of piezo-film stacked together with thin epoxy layers. (a) The piezo-film sandwiched between two thinner layers of conducting glue which carry current from the film. (b) The plane-view geometry of the receiver which has a circular geometry with a 1.25 cm diameter. (c) The parallel connection of these piezo-elements which results in a four time increase in current output.

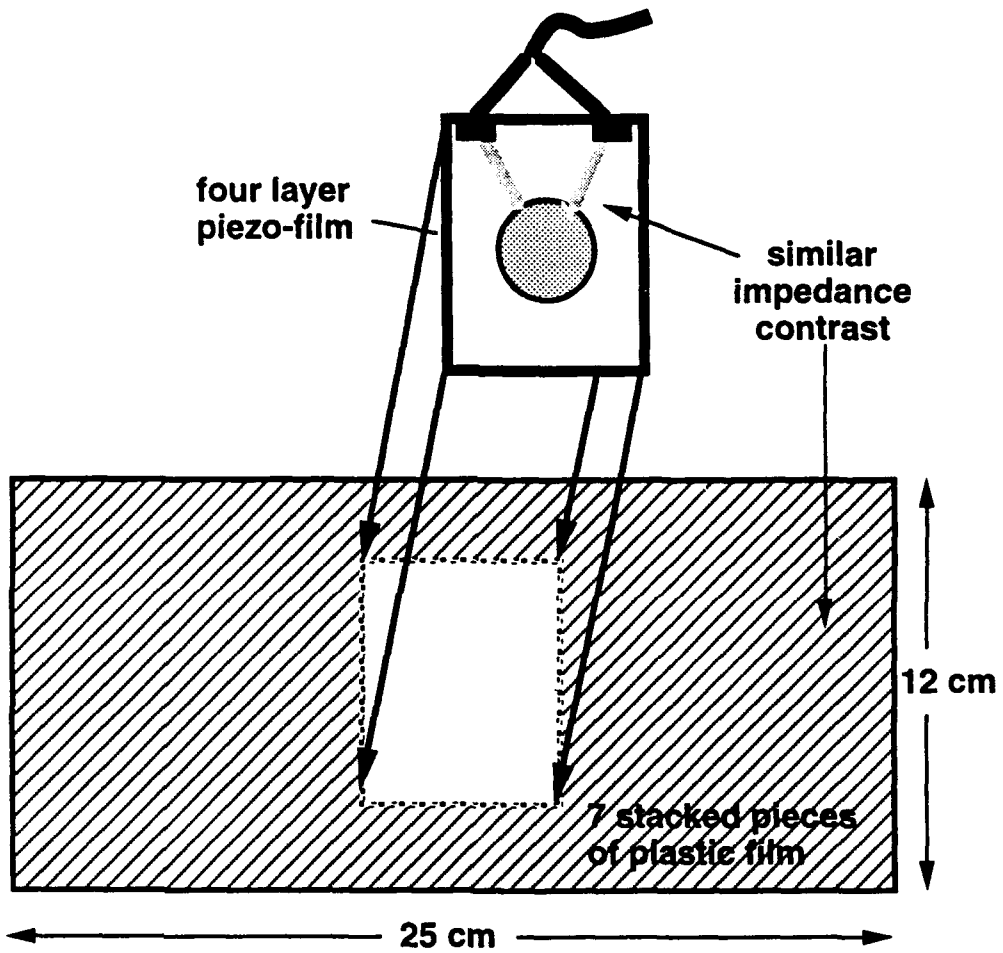


Figure B.3: Geometry of the piezo-film sheet. The piezo-film element is inserted into of a larger sheet of stacked plastic layers to reduce diffractions from the edge of the receiver element. The sheet of plastic layers was created by stacking  $110\mu$  thick layers until the impedance contrast matched that of the piezo-film.

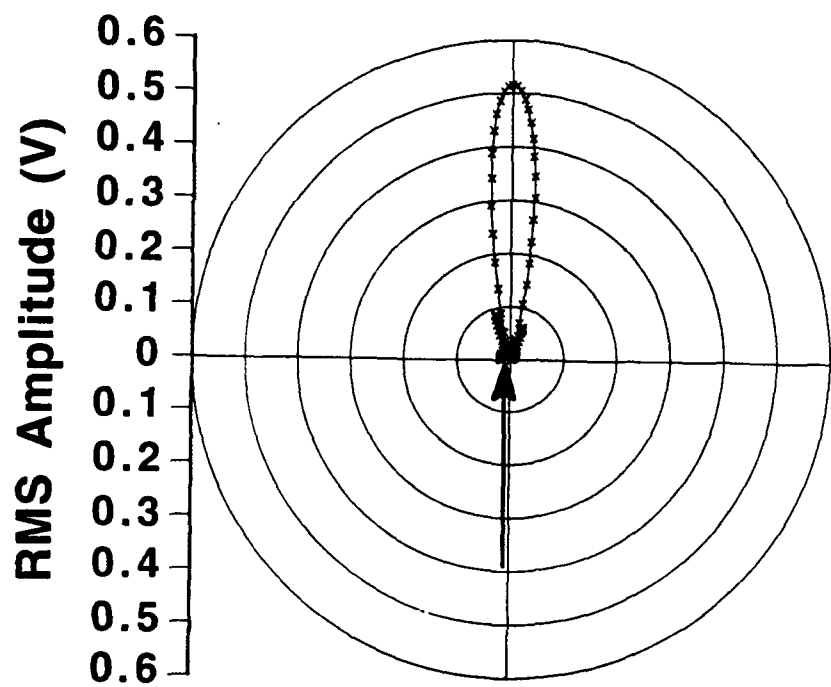


Figure B.4: The sensitivity pattern of the four layer piezo-film receiver at 500 kHz.